Stony Brook University

Multidimensional Simulations of Type Ia Supernovae and Classical Novae

A Dissertation Presented

by

Brendan Kurt Krueger

to

The Graduate School

in Partial Fulfillment of the

Requirements

for the Degree of

Doctor of Philosophy

in

Physics

Stony Brook University

August 2012

Stony Brook University

The Graduate School

Brendan Kurt Krueger

We, the dissertation committee for the above candidate for the Doctor of Philosophy degree, hereby recommend acceptance of this dissertation.

Dr. Alan C. Calder – Dissertation Advisor
Assistant Professor, Department of Physics and Astronomy

Dr. Frederick M. Walter – Chairperson of Defense
Professor, Department of Physics and Astronomy

Dr. Michael Zingale
Associate Professor, Department of Physics and Astronomy

Dr. Peter Stephens
Professor, Department of Physics and Astronomy

Dr. Marc-André Pleier
Associate Physicist, Physics Department
Brookhaven National Laboratory

This dissertation is accepted by the Graduate School.

Charles Taber
Interim Dean of the Graduate School

Abstract of the Dissertation

Multidimensional Simulations of Type Ia Supernovae and Classical Novae

by

Brendan Kurt Krueger

Doctor of Philosophy

in

Physics

Stony Brook University

2012

Explosive astrophysical phenomena have historically played a significant role in understanding the universe and our place within it. Stellar explosions are important distance indicators, allowing exploration of the structure and evolution of the universe. They also form and disperse heavy elements that are recycled into new astrophysical objects. Stellar explosions are not a uniform group; the progenitors and mechanisms of stellar explosions vary tremendously. I used multidimensional simulations to study two distinct types of explosions that are believed to result from similar progenitor systems: compact white dwarf stars that accrete matter from stellar companions. The two types of explosions I studied are type Ia supernovae and classical novae.

Type Ia supernovae are thought to arise from a thermonuclear explosion originating in the core of an accreting white dwarf and leave no remnant. These events are the premier distance indicators in cosmological studies, but questions remain about systematic biases and intrinsic scatter. My investigation centered on the systematic impact of the central density of the progenitor on the brightness of the supernova. Relating the progenitor's central density to its age provided a theoretical explanation of the observed trend that type Ia supernovae from older stars are dimmer. I also demonstrated the importance of a statistical study of such problems, due to the strongly nonlinear evolution during the explosion.

Classical novae are important for the study of circumstellar dust formation and are significant contributors of specific isotopes found in our galaxy. They result

from a thermonuclear runaway occurring in the accreted envelope on a white dwarf. Only the envelope is consumed, so the white dwarf remains and the event may recur on time scales of 10^4 to 10^5 years. My study made use of a new simulation code specialized for low-Mach number flows, such as convection just prior to the explosion. I developed hydrostatic initial models and physics modules necessary for simulations of classical novae. This problem provided unexpected challenges, but preliminary simulations of convection-driven mixing between the accreted envelope and the underlying white dwarf are underway. Future results will explore the effects of convection, particularly the quantity and mechanisms of mixing.

My research into stellar explosions provided important insight into their mechanisms and required considerable development work, which improved our models and will allow more realistic simulations in the future.

For Erin.

Contents

List of Figures

List of Tables

Abbreviations

This list is ordered alphabetically by abbreviation for ease of reference, not by order of appearance in the text.

ADR	advection-diffusion-reaction
AGB	asymptotic giant branch
AMR	adaptive mesh refinement
CFL	Courant-Friedrichs-Lewy (Courant et al., 1928)
CN	classical nova (plural: CNe, classical novae)
CNO	carbon-nitrogen-oxygen
CV	cataclysmic variable
DDT	deflagration-to-detonation transition
DTD	delay time distribution
EoS	equation of state
GCD	gravitationally-confined detonation
HSE	hydrostatic equilibrium
IGE	iron-group element
NSE	nuclear statistical equilibrium
NSQE	nuclear statistical quasi-equilibrium (also known in the literature as QSE, or quasi-statistical equilibrium)
pp	proton-proton
rp	rapid proton
SDC	spectral deferred correction
SNIa	type Ia supernova (plural: SNeIa, type Ia supernovae)
TFI	turbulence-flame interaction

V&V verification and validation

WD white dwarf

WLR width-luminosity relation

Acknowledgements

Near the end of *The Lord of the Rings*[1], when the One Ring finally exhausts Frodo, Samwise declares, "I can't carry it for you, but I can carry you!" This dissertation may have my name on the cover, but there were many who helped to carry me this far.

Firstly I would like to thank my Lord and Savior, who has been my constant companion and who gifted us with this beautiful universe to discover.

Without the encouragement and sacrifice of my wife, Erin, this dissertation would not exist. I could not hope to list all the ways she has been a blessing to me.

I never would have begun grad school without the support and encouragement of my parents, who taught me to work hard in pursuit of what I love.

Despite his protests to the contrary, Alan Calder has been an outstanding advisor. He has managed to balance when to step in and offer direction and when to allow me to find my own way.

The faculty of the Department of Physics and Astronomy have been wonderful. In particular, I would like to thank Mike Zingale and Doug Swesty, whose encouragement and guidance have been greatly appreciated.

Surviving grad school is a team sport. My thanks also go to my fellow grad students: Aaron, Chris, Josh, Rahul, Melissa, Adam, Yeunhwan, Kendra, Bryan, and Stephanie.

My collaborators, Dean Townsley, Ed Brown, and Frank Timmes, have endured an endless string of revisions of my papers and have patiently helped me develop my research and refine my writing into work worth publishing.

The text of this dissertation in part is a reprint of the materials as it appears in the Astrophysical Journal Letters and the Astrophysical Journal. The co-authors listed in the publications directed and supervised the research that forms the basis for this dissertation. Several images included in this dissertation have been reprinted by permission of Frank X. Timmes.

The work described in this dissertation was supported by several sources, including NASA through grant NNX09AD19G, the US Department of Energy through grant DE-FG02-87ER40317, and Lawrence Livermore National Laboratory through contracts B589924 and B593287. Computational resources were provided by the New York Center for Computational Sciences and the National Science Foundation through the TeraGrid and XSEDE projects.

[1] If you didn't expect me to put a *Lord of the Rings* quote in my dissertation, then you must not know me very well.

Chapter 1

Introduction

In this dissertation I explore two distinct, but related, topics: type Ia supernovae (SNeIa, discussed in Part I), and classical novae (CNe, discussed in Part II). Both are explosive astrophysical phenomena involving thermonuclear reactions in or on the surface of a compact stellar object that is accreting matter from a companion star. Stellar explosions are scientifically interesting for many reasons; for example, they synthesize and distribute heavy elements, which strongly impacts galactic chemical evolution, and they can be used as distance indicators, which has led to ground-breaking discoveries in cosmology. My research involves the use of numerical simulations of these explosions, with the goal of understanding the mechanisms which drive them and the processes involved.

1.1 Progenitor Systems

Despite significant differences in their mechanisms, SNeIa and CNe result from similar progenitor systems: a binary star system with one compact star and one non-compact star[1]. The non-compact star, referred to as the companion star, is typically assumed to be either a red giant or a star on the main sequence. In both cases, the compact star is a white dwarf (WD). White dwarfs are the endpoint of stellar evolution of stars with zero-age main-sequence masses ($M_{\rm ZAMS}$) less than approximately $8\,M_\odot$ (Nomoto, 1984). Once such a star has consumed its fuel, it contracts due to the loss of pressure support in the core. This contraction continues until the pressure from electron degeneracy becomes sufficient to halt the collapse[2]. The composition of the resulting WD will primarily be helium for the lowest $M_{\rm ZAMS}$, a carbon-oxygen mixture for intermediate $M_{\rm ZAMS}$, or an oxygen-neon mixture for the highest $M_{\rm ZAMS}$; both CNe and SNeIa are believed to result from carbon-oxygen WDs. Due to the properties of electron-degenerate material, WDs have an upper mass limit that depends on properties of the particular WD (e.g., the electron-to-baryon ratio and the spin period); this upper limit is known as the Chandrasekhar mass ($M_{\rm Ch}$) and is typically around

[1] Other models exist for SNeIa; see Section 2.2.

[2] Electron degeneracy pressure is a quantum mechanical phenomenon that arises when fermions are compressed to the point where the Pauli exclusion principle forces a fermion to move to a higher energy state in order to compress further, which manifests as a pressure (Fowler, 1926).

$1.4\,M_\odot$ (Chandrasekhar, 1931a,b, 1935). To give a sense of scale, a WD with a mass near $1\,M_\odot$ will have a radius comparable to that of the Earth.

In binary systems, it is possible to transfer mass between stars. For the systems that I am considering, several mechanisms exist to transfer mass from the non-compact companion onto the surface of the WD: primarily Roche-lobe overflow, in which the companion's outer layers are no longer gravitationally bound to the core of the companion due to the proximity of the WD, and stellar wind. A variety of phenomena may result from such mass transfer, including an assortment of cataclysmic variables (of which CNe are a subset) and SNeIa.

1.2 Numerical Simulations

My research is based on numerical simulations of these two phenomena. I do not simulate any stellar evolution or mass transfer, only the explosion itself. I use progenitor models informed by stellar evolution research to capture the state of the star immediately prior to the explosion. Therefore my simulations do not include the entire binary system, but only the WD (all or part of the WD, depending on the simulation).

I use two different simulation tools for my simulations: `FLASH` and `MAESTRO`. Both codes solve modified versions of the Euler equations for inviscid flow (Euler, 1757a,b,c, 1761) on a discretized grid of control volumes; that is, they are finite-volume Eulerian hydrodynamics codes. Modifications to the underlying hydrodynamics equations include the ability to handle multi-scale flows (e.g., through adaptive mesh refinement), gravity, nuclear reactions, and non-ideal equations of state. Further discussion of these two codes will be deferred until later; for a discussion of `FLASH` see Section 2.5, and for a discussion of `MAESTRO` see Section 6.4.

These computational tools are modern research tools designed to run on the largest computing platforms available. The challenge of including all the significant physical processes, spanning the diverse scales that are important to the phenomena being studied, and scaling well to get maximum use of the computational resources available makes these problems interesting from the perspective of computational science as well.

Part I

Type Ia Supernovae

Chapter 2

Overview

Type Ia supernovae have long provided a source of surprising discoveries about the structure of our universe and our place within it. Tycho Brahe's publication of *De Nova Stella* in 1573 signalled the end of Aristotelian cosmology: the unchanging heavens had changed, and with them our view of the universe we inhabit (Chaisson & McMillan, 2001). More recently, the Supernova Cosmology Project (Perlmutter et al., 1999) and the High-z Supernova Search Team (Riess et al., 1998) found evidence that the expansion of the universe is accelerating in violation of prior expectations of the structure of the universe, suggesting the existence of dark energy and revolutionizing our understanding of cosmology (Nobelprize.org, 2011). SNeIa continue to be the premier distance indicators for probing the structure and expansion history of the universe, but their intrinsic scatter in brightness and the inherent uncertainty in measuring and calibrating them are becoming dominant sources of uncertainty in measurements of cosmological parameters. A better understanding of the mechanism of SNeIa could potentially lower these uncertainties and allow a deeper test of cosmology.

2.1 Historical Overview

The oldest known stellar explosion is recorded in the 5th century Chinese book *The Book of the Later Han*, which discusses the appearance of a "guest star" in the year 185 (Fan Ye, 5th century; see also Stothers, 1977). The modern study of stellar explosions began with Tycho Brahe's *De Nova Stella* ("On the New Star"; Brahe, 1573), describing the appearance of a new star. From Tycho's work we derive the modern name "novae" for these phenomena. In the early twentieth century, studies of novae began to distinguish a category that were significantly more luminous than other novae, which were termed "supernovae" by Baade and Zwicky (1934; see also Osterbrock, 2001). In 1941 Minkowski began the spectral system to distinguish between classes of supernovae, proposing two types: type I, which lacks evidence of hydrogen in their spectrum, and type II, which have hydrogen present (Minkowski, 1941). Type I supernovae were further divided into types Ia, Ib, and eventually Ic (Bertola, 1964; Porter & Filippenko, 1987).

Hoyle & Fowler (1960) first proposed the idea of a thermonuclear runaway in the core of a star supported by electron degeneracy as the mechanism for SNeIa. Whelan & Iben (1973) further refined this model by proposing what is now known as the single-degenerate paradigm: a carbon-oxygen WD, supported by electron degeneracy, approaches $M_{\rm Ch}$ through

accretion from a binary companion and undergoes an explosion as an SNeIa. Truran et al. (1967) and Colgate & McKee (1969) developed the idea that the source of energy for the light curve of SNeIa is the radioactive decay of ^{56}Ni produced in the explosion.

Over the next few decades, theoretical models of SNeIa were refined. It was shown that prompt detonations (in which the burning front propagates supersonically) do not reproduce the observational signatures of SNeIa (Nomoto et al., 1976; Woosley & Weaver, 1986), while the W7 model of Nomoto et al. (1984) showed that, in one dimension, a deflagration (in which the burning front propagates subsonically) is able to reproduce many observations. However, even the deflagration model suffers from some shortcomings, and Khokhlov (1991a) introduced the delayed-detonation model, in which the explosion begins as a deflagration and transitions to a detonation later in the supernovae outburst. This delayed-detonation model is still the favored model in modern simulations of the single-degenerate paradigm of SNeIa.

2.2 Current Theory

The single-degenerate paradigm is not the only commonly-studied model for SNeIa. The double-degenerate paradigm, introduced by Webbink (1984) and Iben & Tutukov (1984), is the primary competing model to explain SNeIa. As with the single-degenerate paradigm, the double-degenerate paradigm assumes that a progenitor system is a binary star system. However, instead of one WD approaching $M_{\rm Ch}$ by accretion from a non-degenerate companion, the double-degenerate paradigm assumes that both stars are WDs and the explosion is initiated by a merger as the two WDs spiral together. My research focuses on the single-degenerate paradigm, so the double-degenerate paradigm will not be discussed further.

Even within the single-degenerate paradigm, there are a variety of mechanisms. Since Khokhlov (1991a), most simulations of SNeIa have used the delayed detonation model, but the details of how the detonation is initiated are as yet unknown. Various mechanisms exist, including the gravitationally-confined detonation first proposed by Plewa et al. (2004). My research focuses on the mechanism known as the deflagration-to-detonation transition (DDT), introduced in Khokhlov (1991a), in which the explosion begins as a deflagration within the core of the WD, and eventually some critical set of conditions is reached that causes a transition to a detonation mode. The details of this transition are actively being studied in both terrestrial and astrophysical contexts. The method used in my research is a simple model that assumes the transition occurs when the flame front reaches some characteristic density, the details of which will be explained below.

2.3 Width-Luminosity Relation

Phillips (1993) showed that the width and luminosity of the peak of SNIa light curves (brightness as a function of time) are correlated. In other words, knowing how fast the brightness declines from maximum specifies the intrinsic maximum brightness of the SNIa. This relation, known as the Phillips relation or the width-luminosity relation (WLR), can be calibrated against other methods in the astronomical distance ladder and used as a "standardizable candle": knowing how bright a supernova actually is and how bright it

appears to be determines how far away it is. Using SNeIa as standardizable candles enables studies of cosmological structure and expansion history, and was instrumental in determining that the expansion of the universe is accelerating (Riess et al., 1998; Perlmutter et al., 1999).

The use of SNeIa to determine cosmological parameters has benefited from the rapidly-growing quantity of data available. The number of SNIa observations has decreased the statistical uncertainty to the point where the systematics, such as variations of SNIa light curves with galaxy properties, will soon be the dominant source of uncertainty (Sullivan et al., 2011). In order to reduce the systematic uncertainty, it is necessary to gain a better understanding of the mechanism that underlies SNeIa. Recent work has begun to account for correlations of the brightness and light curve of an SNIa with properties of the host galaxy (Conley et al., 2011). Improvements in our understanding of the mechanism of SNeIa may shed light on these host galaxy correlations, and lower the systematic uncertainty in cosmological parameters.

2.4 Goals of Research in SNeIa

The vast majority of SNeIa obey this WLR, but an important question remains: What is the intrinsic scatter of these events? Or, to put it differently, how well does the WLR hold? Observations of SNeIa make use of a parameter known as the Hubble residual, which is the difference between the distance inferred from a SNIa based on its light curve properties and the WLR and the distance inferred from its redshift and the expansion of the universe. This expansion was originally described by the Hubble Law (Lemaître, 1927; Hubble, 1929), hence the term Hubble residual. To quote from Kelly et al. (2010): "Correlations between Hubble residuals and progenitor properties have the potential to introduce bias into SN Ia cosmological measurements [...]. If correlations are identified, host measurements such as size, mass, or metallicity could be combined with light curve parameters [...] to improve luminosity distance estimates to SNe Ia and control systematics in cosmological measurements."

As a prelude to addressing the Hubble residual, Townsley et al. (2009) presented a method to investigate how certain properties of a progenitor WD impact the outcome of the associated SNIa explosion, particularly the brightness of the SNIa. This collaborative study is an ongoing research program, with several aspects presented in Townsley et al. (2009), Jackson et al. (2010), Krueger et al. (2010), and Krueger et al. (2012). My research has focused on the influence of the central density of the progenitor WD immediately prior to the formation of the deflagration front. Lesaffre et al. (2006) showed that two progenitors that differ only in the time elapsed between the formation of the WD and the onset of accretion from the companion (known as the cooling time) will have different central densities at the point where the conditions for the formation of a deflagration front are met, with longer cooling times resulting in higher central densities. Thus the central density at the formation of the deflagration front is a proxy for the age of the progenitor star[1]. I investigated how the brightness of an SNIa depends on this density, seeking a theoretical explanation of the observed trend that older stars are systematically dimmer (Gallagher et al., 2008; Howell

[1]See Section 4.5.2 for clarification on the measurements of "age" for SNeIa

et al., 2009; Neill et al., 2009; Brandt et al., 2010).

2.5 The FLASH Code

This research was done by performing a suite of multidimensional full-star simulations of SNeIa. My simulations were performed using a customized version of the FLASH code. FLASH is a hydrodynamics code designed to simulate nuclear-powered astrophysical flashes (Fryxell et al., 2000; Calder et al., 2002b). It solves a modified version of the Euler equations for inviscid flow that accounts for reactions. We may write these compressible reactive hydrodynamics equations as:

$$\frac{\partial \rho X_k}{\partial t} = -\nabla \cdot (\rho X_k \mathbf{u}) + \rho \dot{\omega}_k \tag{2.1a}$$

$$\frac{\partial \rho \mathbf{u}}{\partial t} = -\nabla \cdot (\mathbf{u} \otimes \rho \mathbf{u}) - \nabla P - \rho \mathbf{g} \tag{2.1b}$$

$$\frac{\partial \rho e}{\partial t} = -\nabla \cdot (\mathbf{u} (\rho e + P)) + \rho \dot{e}_{\mathrm{nuc}} + \rho \mathbf{u} \cdot \mathbf{g}, \tag{2.1c}$$

where ρ is the mass density, X_k is the mass fraction for species k, $\mathbf{u}$ is the fluid velocity, $\dot{\omega}_k$ is the rate of change of species k, P is the pressure, $\mathbf{g}$ is the acceleration of gravity, e is the total energy density, and $\otimes$ is a dyadic product[2]. The mass fraction of a species is the ratio of the partial mass density to the total mass density ($X_k \equiv \rho_k / \rho$); for a given control volume, it is also the ratio of the mass of all nuclei of species k to the total mass in the control volume. It follows from this definition that

$$\sum_k \rho_k = \rho \qquad \text{and} \qquad \sum_k X_k = 1. \tag{2.2}$$

Due to conservation of mass[3],

$$\sum_k \dot{\omega}_k = 0. \tag{2.3}$$

[2]The dyadic product is also known as an outer product or tensor product. The dyadic product of two vectors creates a tensor of order two; the statements $P = \mathbf{v} \otimes \mathbf{w}$ and $P_{ij} = v_i w_j$ are equivalent. Equation (2.1b) may be clearer in component form:

$$\frac{\partial \rho u_i}{\partial t} = -\nabla \cdot (u_i \rho \mathbf{u}) - \frac{\partial P}{\partial x_i} - \rho g_i,$$

where this is a set of equations: one for each spatial dimension.

[3]In actual fact, mass is not conserved due to nuclear reactions converting mass to energy. The quantities $\dot{X}_k$ and $\dot{\omega}_k$ are not equivalent because X_k are fractions and by definition must sum to unity so that $\dot{X}_k$ must sum to zero, while $\dot{\omega}_k$ may account for this mass non-conservation and will therefore not generally sum to zero. However, even in an extreme case such as pure hydrogen converting to pure nickel, the change in mass is less than 1%, so most hydrodynamic codes neglect this mass non-conservation and $\dot{\omega}_k$ will sum to zero.

Given Equations (2.2) and (2.3), a summation over k of Equation (2.1a) yields

$$\frac{\partial \rho}{\partial t} = -\nabla \cdot (\rho \, \mathbf{u}) \, . \tag{2.4}$$

This summed form, along with Equations (2.1b) and (2.1c), can be seen as expressions of the conservation of mass, momentum, and energy respectively. The relationship between the specific total energy, e, and the specific internal energy, ε, is

$$e = \varepsilon + \frac{1}{2} (\mathbf{u} \cdot \mathbf{u}) \, . \tag{2.5}$$

The term $\dot{e}_{\text{nuc}}$ represents a source term from the energy released by nuclear reactions. This system of equations is not closed; it requires a relation between the pressure and the density. This is given by the equation of state (EoS), which relates the thermodynamic quantities of the system (e.g., density, pressure, energy, temperature, entropy); typically an EoS for astrophysical simulations will require two thermodynamic quantities and the composition.

`FLASH` makes use of adaptive mesh refinement (AMR), which allows grid cells to be subdivided or merged together in order to increase or decrease the resolution as needed. This is a powerful feature, which allows high resolution to capture important details in the "interesting" region of a simulation without wasting time computing unnecessary details in the "uninteresting" regions. What regions of a simulation are considered "interesting" depends on the goals of a particular simulation, and may include considerations such as energy generation or steep gradients in fluid quantities.

The core of `FLASH` was developed at the Flash Center for Computational Science at the University of Chicago, and is available directly from the Flash Center[4]. The details of the variant used to perform my simulations are described in Townsley et al. (2007), Townsley et al. (2009), and Jackson et al. (2010), with important support information on certain components and/or implementations presented in Calder et al. (2007) and Seitenzahl et al. (2009b). The modifications made to this custom version of the `FLASH` code are also summarized in Krueger et al. (2010) and Krueger et al. (2012); see Chapters 3 and 4.

[4] `http://flash.uchicago.edu/`

Chapter 3

Effect of the Central Density - Paper I

This chapter is a reproduction of the first paper I published on the problem of the central density dependence of SNeIa. It was originally published in the Astrophysical Journal Letters (Krueger et al., 2010). In this paper I present the main findings of my research. Due to the length restrictions of the Letters format, some details had to be omitted; those details, along with a more in-depth analysis, were presented in Krueger et al. (2012); see Chapter 4. This paper is reproduced by permission of the American Astronomical Society. The co-authors directed and supervised the research that forms the basis for this paper.

ON VARIATIONS OF THE BRIGHTNESS OF TYPE Ia SUPERNOVAE WITH THE AGE OF THE HOST STELLAR POPULATION

Brendan K. Krueger[1], Aaron P. Jackson[1], Dean M. Townsley[2], Alan C. Calder[1,3], Edward F. Brown[4], and F. X. Timmes[5]

[1] Department of Physics & Astronomy, The State University of New York–Stony Brook, Stony Brook, NY, USA
[2] Department of Physics and Astronomy, The University of Alabama, Tuscaloosa, AL, USA
[3] New York Center for Computational Sciences, The State University of New York–Stony Brook, Stony Brook, NY, USA
[4] Department of Physics and Astronomy, Michigan State University, East Lansing, MI, USA
[5] School of Earth and Space Exploration, Arizona State University, Tempe, AZ, USA

Received 2010 March 16; accepted 2010 July 2; published 2010 July 16

ABSTRACT

Recent observational studies of type Ia supernovae (SNeIa) suggest correlations between the peak brightness of an event and the age of the progenitor stellar population. This trend likely follows from properties of the progenitor white dwarf (WD), such as central density, that follow from properties of the host stellar population. We present a statistically well-controlled, systematic study utilizing a suite of multi-dimensional SNeIa simulations investigating the influence of central density of the progenitor WD on the production of Fe-group material, particularly radioactive ^{56}Ni, which powers the light curve. We find that on average, as the progenitor's central density increases, production of Fe-group material does not change but production of ^{56}Ni decreases. We attribute this result to a higher rate of neutronization at higher density. The central density of the progenitor is determined by the mass of the WD and the cooling time prior to the onset of mass transfer from the companion, as well as the subsequent accretion heating and neutrino losses. The dependence of this density on cooling time, combined with the result of our central density study, offers an explanation for the observed age–luminosity correlation: a longer cooling time raises the central density at ignition thereby producing less ^{56}Ni and thus a dimmer event. While our ensemble of results demonstrates a significant trend, we find considerable variation between realizations, indicating the necessity for averaging over an ensemble of simulations to demonstrate a statistically significant result.

Key words: hydrodynamics – nuclear reactions, nucleosynthesis, abundances – supernovae: general – white dwarfs

1. INTRODUCTION

Observations targeting the environment of type Ia supernovae (SNeIa) have exposed open questions concerning the dependence of both their rates and average brightness on environment. Mannucci et al. (2006) show that the dependence of the SNIa rate on delay time (elapsed time between star formation and the supernova event) is best fit by a bimodal delay time distribution (DTD) with a prompt component less than 1 Gyr after star formation and a tardy component several Gyr later. Although the clarity of this effect is clouded by galaxy sampling (Filippenko 2009), the basic result is borne out even within galaxies (Raskin et al. 2009). Gallagher et al. (2008) measure a correlation between the brightness of an SNIa and its delay time, which they state is consistent with either a bimodal or a continuous DTD. Other recent studies by Howell et al. (2009), Neill et al. (2009), and Brandt et al. (2010) also find a correlation between the delay time and brightness of an SNIa.

Phillips (1993) identified a linear relationship between the maximum *B*-band magnitude of a light curve and its rate of decline. This "brighter equals broader" relationship has been extended to additional bands with templates from nearby events, allowing SNeIa to be calibrated as an extension of the astronomical distance ladder (see Jha et al. 2007 for a description of one method). The brightness of an SNIa is determined principally by the radioactive decay of ^{56}Ni synthesized during the explosion (Truran et al. 1967; Colgate & McKee 1969; Arnett 1982; Pinto & Eastman 2000).

A widely accepted proposal to explain many, if not most, events is the thermonuclear disruption of a white dwarf (WD) in a mass-transferring binary system (for reviews from various perspectives see Branch et al. 1995; Filippenko 1997; Hillebrandt & Niemeyer 2000; Livio 2000; Röpke 2006). In this paradigm, a longer delay time suggests the possibility of a longer elapsed time between the formation of the WD and the onset of accretion. During this period, denoted here as the WD cooling time ($t_{\rm cool}$), the WD is isolated from any significant heat input and decreases in temperature. A longer $t_{\rm cool}$ results in a higher central density when the core reaches the ignition temperature (Lesaffre et al. 2006), due to the lower entropy at the onset of accretion. Thus, a correlation between central density and the peak brightness of an event suggests a correlation between delay time and the brightness of an event. While previous work indicated a correlation between central density and peak brightness, none has averaged over a statistically significant ensemble of realizations (Brachwitz et al. 2000; Röpke et al. 2006; Höflich et al. 2010). Therefore, we investigate, for the first time, a statistically significant correlation between progenitor central density and average peak brightness of SNeIa.

The surrounding stellar population, the metallicity and mass of the progenitor, the thermodynamic state of the progenitor, the cooling and accretion history of the progenitor, and other parameters are known to affect the light curves of SNeIa; the role, and even primacy, of these various parameters is the subject of ongoing study (e.g., Röpke et al. 2006; Höflich et al. 2010; Jackson et al. 2010). Additionally, many of these effects may be interconnected in complex ways (Lesaffre et al. 2006). In this study, we isolate the direct effect of varying the progenitor central density on the production of ^{56}Ni. To first order, this yield controls the brightness of an event;

second-order effects on the light curve are left for future study.

2. METHOD

Once a WD forms in a binary, it is initially isolated and slowly cools in a single-degenerate scenario. Eventually, mass transfer begins to carry light elements from the envelope of the companion to the surface of the WD. If the accretion rate exceeds a threshold, the infalling material experiences steady burning (Nomoto et al. 2007), and eventually the WD gains enough mass to compress and heat the core. Once the temperature rises enough to initiate carbon reactions, the core begins to convect (or "simmer"). Our progenitor models parameterize the WD at the end of this simmering phase, just prior to the birth of the flame that eventually will disrupt the entire WD in an SNIa.

We constructed a series of five parameterized, hydrostatic progenitor models that account for simmering in which we vary the central density (ρ_c). The outer regions are isothermal, although some temperature structure is expected (Kuhlen et al. 2006), and the cores are isentropic due to convection and have a lower C/O ratio (Straniero et al. 2003; Piro & Bildsten 2008; Chamulak et al. 2008; Piro & Chang 2008). Jackson et al. (2010) explored these effects and we chose the core composition as 40% ^{12}C, 57% ^{16}O, and 3% ^{22}Ne and the outer layer as 50% ^{12}C, 48% ^{16}O, and 2% ^{22}Ne. For our ρ_c, we chose (1–5) $\times$ 10^9 g cm^{-3} in steps of 10^9 g cm^{-3}. The central temperature must be in the range of carbon ignition, which is approximately (7–8) $\times$ 10^8 K (e.g., Kuhlen et al. 2006); we selected 7×10^8 K. Based on prior research, we chose other model parameters to produce expected amounts of Fe-group elements in the explosion (Townsley et al. 2009; Jackson et al. 2010). The values were kept constant in all simulations in order to isolate the central density effects.

With these five progenitor models, we utilize the statistical framework presented in Townsley et al. (2009) for a controlled study of the effect of varying the central density. For each progenitor, we created 30 realizations seeded by a random number used to generate a unique set of spherical harmonics with power in modes $12 \leqslant \ell \leqslant 16$. The spectra are used as initial perturbations to the spherical flame surface around the center of the progenitor star. Each progenitor uses the same seed values, resulting in the same 30 perturbations. This choice allows us to check for systematic biases in the realizations across different progenitors.

We performed a suite of 150 two-dimensional, axisymmetric simulations of the deflagration-to-detonation transition (DDT) model of SNeIa with a customized version of FLASH, a compressible, Eulerian, adaptive-mesh, hydrodynamics code. The modifications to this code are (1) the burning model, (2) the flame speed computations, (3) the mesh refinement criteria, and (4) the DDT criterion. Our simulation methods are described in detail in previous publications (Calder et al. 2007; Townsley et al. 2007, 2009) and continue to be improved (Jackson et al. 2010; D. M. Townsley et al. 2010, in preparation). We should note that the DDT criterion is based on a characteristic density at which we ignite detonations, which we select to be $10^{7.1}$ g cm^{-3}. Following the procedures described in Calder et al. (2007) and Seitenzahl et al. (2009) for calculating the neutronization rate in material in nuclear statistical equilibrium (NSE), we utilize weak rates from Fuller et al. (1985), Oda et al. (1994), and Langanke & Martínez-Pinedo (2001), with newer rates superseding earlier ones. The reaction networks for calculating the energetics and timescales of the deflagration and detonation phases included the same 200 nuclides, and the NSE calculation

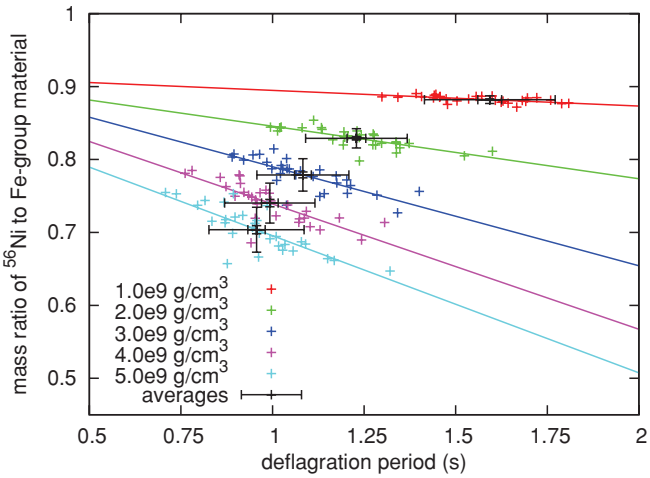

Figure 1. Plot of the ^{56}Ni-to-NSE mass ratio vs. duration of deflagration. Small crosses are single simulations and are colored to indicate ρ_c. Large black crosses show the average values for a given ρ_c with error bars showing the standard deviation and the standard error of the mean.

of tables included 443 nuclides. The supernova simulations use a three-stage burning model in which the timescale to burn to NSE is calibrated to reproduce the correct yield of Fe-group elements. The weak reaction rate is negligible at a density where Si burning to ^{56}Ni is incomplete; therefore, we estimate the ^{56}Ni yield from the total NSE yield and its associated electron fraction. We performed nuclear post-processing of Lagrangian tracer particles using a network of 200 nuclides on a subset of simulations. Comparison demonstrates that our burning model matches the energetics and final composition of important nuclei such as ^{56}Ni (D. M. Townsley et al. 2010, in preparation; see also studies by Travaglio et al. 2004; Seitenzahl et al. 2010). We utilize the adaptive-mesh capability, with a highest resolution of 4 km, which demonstrates a converged result (Townsley et al. 2009).

3. RESULTS AND DISCUSSION

The ^{56}Ni yield is determined partly by neutronization occurring during the thermonuclear burning. Neutronization pushes the nucleosynthetic yield away from balanced nuclei such as ^{56}Ni to more neutron-rich, stable isotopes like ^{58}Ni. Thus, the amount of neutronization influences the brightness of an event and, all else being constant, more neutronization results in a dimmer event. The degree of neutronization depends on the density and temperature evolution of burned material. Generally, thermonuclear burning occurring at higher densities will neutronize faster. In an explosive event like a supernova, the longer material remains in NSE at high densities, the more neutronization occurs (Nomoto et al. 1984; Khokhlov 1991; Calder et al. 2007). Accordingly, for SNeIa, both the central density and the duration of the deflagration phase influence the brightness of an event.

Figure 1 presents the mass fraction of NSE material that is ^{56}Ni as a function of deflagration duration, with points colored to indicate ρ_c. The duration of the deflagration phase is the time elapsed between the formation of a flame front and the ignition of the first detonation point. We consider this elapsed time because there is little contribution to neutronization after the first DDT. The mass of NSE material produced increases during the course of the SNIa and eventually plateaus; we find the point where the NSE yield changes by less than

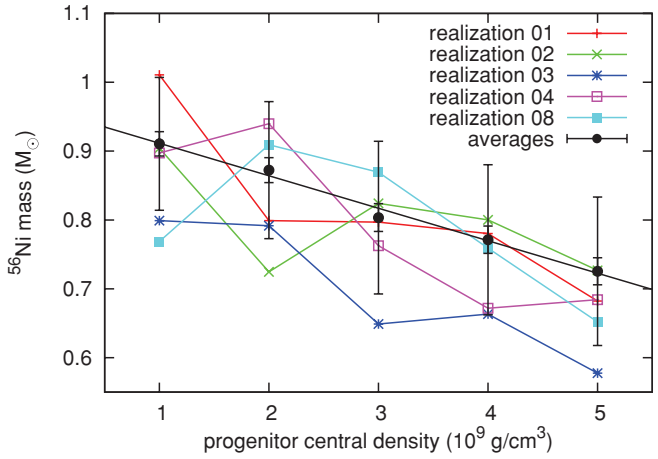

Figure 2. Plot of mass of ^{56}Ni produced vs. ρ_c for five different realizations (colored curves), demonstrating the variety of trends seen for a single realization. These include non-monotonic trends, which could suggest an increase of ^{56}Ni with increasing ρ_c instead of the decrease seen in the ensemble. In black are the average values for each density, along with the standard deviation, the standard error of the mean, and a regression fit to the average values.

0.01% over 0.01 s and use that mass as the final yield of the SNIa. The results have considerable scatter but show two trends. First, at a given ρ_c, simulations with longer deflagration periods tend to have a greater degree of neutronization. Next, simulations from progenitors with higher central densities tend to have a greater degree of neutronization despite having shorter deflagration periods. This result shows that the increased rate of neutronization at higher densities, which can be seen by the steeper slopes of the higher density trend lines, more than compensates for the decrease in time for neutronization to occur. Accordingly, our results qualitatively agree with previous work (e.g., Iwamoto et al. 1999; Brachwitz et al. 2000; Höflich et al. 2010). We also note that the yield of NSE material is, within the error of the slope, independent of ρ_c. As seen in Woosley et al. (2007), if the NSE yield remains constant but the amount of ^{56}Ni varies, then the results should lie along the Phillips relation.

The greater degree of neutronization seen in Figure 1 leads directly to lower ^{56}Ni yields with increasing ρ_c. This result can be seen in Figure 2, which presents the ^{56}Ni yield of each simulation plotted against ρ_c with color used to classify the simulations by realization. The scatter among different realizations at the same ρ_c is greater than the variation across the ρ_c range, indicating the need for analysis of an ensemble of realizations. This scatter can result in a single realization showing a trend unlike the statistical trend; for example, by considering only realization 2 and ρ_c of 2×10^9 and 3×10^9 g cm^{-3} (Figure 2, green curve), we would conclude that increasing ρ_c causes an increase in ^{56}Ni production, instead of a decrease as seen in the overall ensemble. The scatter follows from a strong dependence on the morphology of the flame surface during the early deflagration, which varies the duration of the deflagration and the production of ^{56}Ni. Changing ρ_c can cause a local change in the plume dynamics that overrides the general trend. By fitting the averages, we find the relation

$$M_{^{56}\mathrm{Ni}} = A\rho_c + B, \tag{1}$$

where

$$A = -0.047 \pm 0.003 \ \frac{M_\odot}{10^9\,\mathrm{g\,cm^{-3}}}$$
$$B = 0.959 \pm 0.009 \ M_\odot.$$

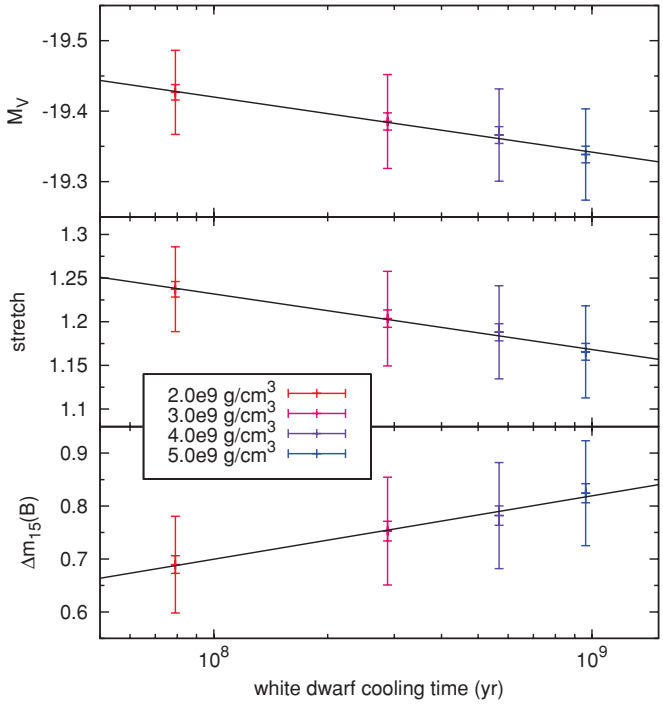

Figure 3. Plot of brightness vs. t_{cool} in terms of M_V (upper panel), s (central panel), and $\Delta m_{15}(B)$ (lower panel). Plotted are the average values for each ρ_c along with the standard deviation, the standard error of the mean, and a regression fit to the average values.

We use data from Lesaffre et al. (2006) to correlate ρ_c to t_{cool}, one component of the delay time, specifically the results for a WD with a pre-accretion mass of $1\,M_\odot$. Thus, if we imagine a collection of stars forming with the same zero-age main-sequence mass but with different companions and binary separations, the delay time would be dominated by t_{cool}. There are large uncertainties in the relationship between ρ_c and t_{cool}; accordingly, we neglect error derived from this large uncertainty in our analysis. We note that the work of Lesaffre et al. (2006) suggests that a WD with a central density of 10^9 g cm^{-3} will not ignite; further accretion is necessary to reach ignition conditions. Therefore, we cannot use Lesaffre et al. (2006) to compute a t_{cool} for our lowest-ρ_c simulations, and so we omit such simulations.

We convert our ^{56}Ni mass to stretch (s) (Howell et al. 2009), the magnitude difference in the B band between maximum light and 15 days after maximum light ($\Delta m_{15}(B)$; Goldhaber et al. 2001), and absolute magnitude in the V band at maximum light (M_V; Phillips et al. 1999) in order to compare with observational findings, shown in Figure 3. A detailed comparison of our models to these observables requires radiative transport calculations of synthetic spectra and light curves, but our results drawn from the ^{56}Ni mass are sufficient for the basic properties we consider here. Woosley et al. (2007) showed that the brightness of an event depends on the mass of ^{56}Ni when it is distributed through a large fraction of the star as in our simulations. Additionally, Stritzinger et al. (2006) showed that late-time nebular spectroscopy finds ^{56}Ni yields consistent with those found from peak luminosity using the inverse of the relations we use.

We find that the best-fit relations follow the form

$$q = \alpha_q \ \log_{10}\left(\frac{t_{\mathrm{cool}}}{\mathrm{yr}}\right) + \beta_q, \tag{2}$$

where q is one of $\Delta m_{15}(B)$, s, or M_V. The values for α_q and β_q are shown in Table 1.

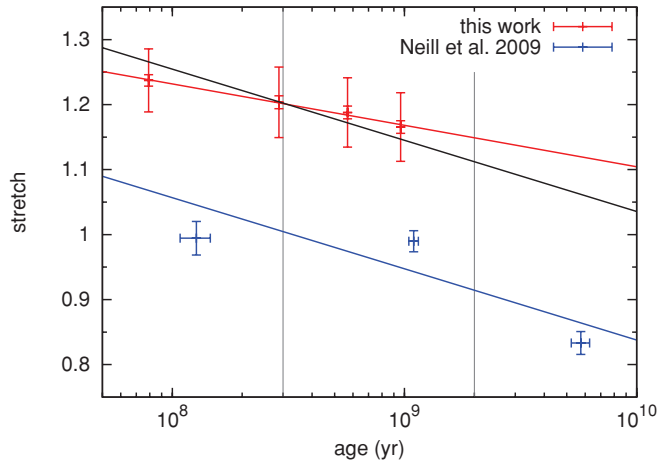

Figure 4. Plot of stretch vs. age. In red are the points from this study, based on variations in ρ_c, along with the standard deviation, the standard error of the mean, and a best-fit trend line following the form of Equation (2). In blue are the binned and averaged points from Figure 5 of Neill et al. (2009), along with a best-fit trend line following the form of Equation (2). The vertical gray lines mark the cuts between bins in the Neill et al. (2009) analysis. The trend line for the Neill et al. (2009) data is shifted upward for comparison to our results (black line). The overall offset to larger stretch in the simulations is due to the choice of DDT density. The approximate agreement of the overall trend indicates that the variation of ρ_c is an important contributor to the observed trend, but that other factors are also important.

Table 1
Best-fit Parameters for Brightness–Age Relations

q	α_q	β_q
M_V	0.078 ± 0.006	-20.05 ± 0.05
s	-0.064 ± 0.005	1.74 ± 0.04
$\Delta m_{15}(B)$	0.120 ± 0.009	-0.26 ± 0.08

To highlight the comparison with observations, in Figure 4 we plot an expansion of the center panel from Figure 3 with the binned results from Figure 5 of Neill et al. (2009). While an absolute comparison is not possible, the similarity of the overall trend indicates that variation of ρ_c is an important contribution to the observed dependence. Our choice of initial conditions and DDT density results in an effective calibration that yields higher than expected ^{56}Ni masses. Accordingly, our results are systematically too bright, giving abnormally high values of stretch. Future studies will correct for this effect. A more subtle point comes in the usage of "age": Neill et al. (2009) measures the luminosity-weighted stellar age, while for the theory we have simply used $t_{\rm cool}$ directly, which for late times is the dominant portion of the time elapsed since star formation. Such offsets, either vertical or horizontal, are less important than the overall trend and the range that can be attributed to variation of ρ_c. For comparison, the black line in Figure 4 shifts the best-fit line from the data of Neill et al. (2009) up to align it with our results. The trend due to ρ_c is weaker than in observations, suggesting that ρ_c contributes to the observed trend but that other effects also play a part.

4. CONCLUSIONS AND FUTURE WORK

We simulated a suite of 150 SNIa models with a range of ρ_c to study the trends for a population of SNeIa. We find that on average progenitors with higher ρ_c produce less ^{56}Ni. Höflich et al. (2010) argue that ^{56}Ni in the central regions of the exploding WD does not contribute to the light curve at maximum, and therefore they do not see a significant trend with central density in the maximum V-band magnitude, but rather in late-time brightness. The pure-deflagration models of Röpke et al. (2006) exhibit a shallow increase of produced ^{56}Ni as central density increases, in contradiction of our findings. Iwamoto et al. (1999) find that the trend with central density depends on the DDT transition density; extrapolating from their results, our value of $\rho_{\rm DDT}$ should yield an increasing ^{56}Ni yield as central density increases. We find that small perturbations of the initial flame surface not only influence the final ^{56}Ni yield, but also its dependence on central density through variations in the duration of the deflagration phase caused by differences in plume development. The variation that follows from perturbations on the initial conditions is a critical aspect of multi-dimensional modeling. Only after many realizations with different perturbations of the initial flame surface are simulated does a statistically significant trend with central density emerge. This result, illustrated by Figure 2, demonstrates the need for an ensemble of simulations to explore systematic effects in SNeIa.

By relating ρ_c to $t_{\rm cool}$ and ^{56}Ni to $\Delta m_{15}(B)$, our results support the observational finding that SNeIa from older stellar populations are systematically dimmer. While a degeneracy between age and metallicity in the integrated light of stellar populations exists, the observed dependence of mean brightness of SNeIa on mean stellar age is apparently the stronger effect (Gallagher et al. 2008; Howell et al. 2009). Accordingly, our choice to neglect metallicity effects and to consider only the effect of central density on ^{56}Ni yield allows us to offer a theoretical explanation for this observed trend. If we additionally consider the effect of metallicity, we may see a slightly stronger trend of decreasing brightness with increasing age as has been previously suggested (Timmes et al. 2003). Other effects besides progenitor central density and metallicity, such as progenitor main sequence mass, may also contribute to this trend.

The insensitivity of the overall Fe-group yield to central density, and therefore delay time, along with the dependence of the ^{56}Ni yield on central density, implies that SNeIa of similar brightnesses (and therefore similar ^{56}Ni yield) from progenitors of different ages will not have the same total Fe-group yield. Those from older populations will, on average, have larger masses of stable species. This may argue for a slight non-uniformity in the Phillips relation based on environment (Woosley et al. 2007; Höflich et al. 2010). The resulting closely related family of brightness–decline time relations also provides a physical motivation for intrinsic scatter in the Phillips relation as a result of combining populations with different mean stellar ages. In this picture, the primary parameter is the degree of expansion at DDT, determined by the morphology of the early flame (and the DDT density, which we hold constant), and the age acts a weaker secondary parameter. In any case, the possibility of such an effect motivates further exploration of the impact of central density on the light curve itself.

This work was supported by the Department of Energy through grants DE-FG02-07ER41516, DE-FG02-08ER41570, and DE-FG02-08ER41565, and by NASA through grant NNX09AD19G. A.C.C. also acknowledges support from the Department of Energy under grant DE-FG02-87ER40317. D.M.T. received support from the Bart J. Bok fellowship at the University of Arizona for part of this work. The authors gratefully acknowledge the generous assistance of Pierre Lesaffre, as well as fruitful discussions with Mike Zingale, and the

use of NSE and weak reaction tables developed by Ivo Seitenzahl. The authors also acknowledge the hospitality of the KITP, which is supported by NSF grant PHY05-51164, during the programs "Accretion and Explosion: the Astrophysics of Degenerate Stars" and "Stellar Death and Supernovae." The software used in this work was in part developed by the DOE-supported ASC/Alliances Center for Astrophysical Thermonuclear Flashes at the University of Chicago. This research utilized resources at the New York Center for Computational Sciences at Stony Brook University/Brookhaven National Laboratory which is supported by the U.S. Department of Energy under contract no. DE-AC02-98CH10886 and by the State of New York.

REFERENCES

Arnett, W. D. 1982, ApJ, 253, 785
Brachwitz, F., et al. 2000, ApJ, 536, 934
Branch, D., Livio, M., Yungelson, L. R., Boffi, F. R., & Baron, E. 1995, PASP, 107, 1019
Brandt, T. D., Tojeiro, R., Aubourg, É., Heavens, A., Jimenez, R., & Strauss, M. A. 2010, arXiv:1002.0848
Calder, A. C., et al. 2007, ApJ, 656, 313
Chamulak, D. A., Brown, E. F., Timmes, F. X., & Dupczak, K. 2008, ApJ, 677, 160
Colgate, S. A., & McKee, C. 1969, ApJ, 157, 623
Filippenko, A. V. 1997, ARA&A, 35, 309
Filippenko, A. V. 2009, in Stellar Death and Supernovae Conf. (Santa Barbara, CA: UCSB), http://online.itp.ucsb.edu/online/sdeath_c09/filippenko/
Fuller, G. M., Fowler, W. A., & Newman, M. J. 1985, ApJ, 293, 1
Gallagher, J. S., Garnavich, P. M., Caldwell, N., Kirshner, R. P., Jha, S. W., Li, W., Ganeshalingam, M., & Filippenko, A. V. 2008, ApJ, 685, 752
Goldhaber, G., et al. 2001, ApJ, 558, 359
Hillebrandt, W., & Niemeyer, J. C. 2000, ARA&A, 38, 191
Höflich, P., et al. 2010, ApJ, 710, 444
Howell, D. A., et al. 2009, ApJ, 691, 661
Iwamoto, K., Brachwitz, F., Nomoto, K., Kishimoto, N., Umeda, H., Hix, W. R., & Thielemann, F. 1999, ApJS, 125, 439
Jackson, A. P., Calder, A. C., Townsley, D. M., Chamulak, D. A., Brown, E. F., & Timmes, F. X. 2010, ApJ, in press (arXiv:1007.1138)
Jha, S., Riess, A. G., & Kirshner, R. P. 2007, ApJ, 659, 122
Khokhlov, A. M. 1991, A&A, 245, L25
Kuhlen, M., Woosley, S. E., & Glatzmaier, G. A. 2006, ApJ, 640, 407
Langanke, K., & Martínez-Pinedo, G. 2001, At. Data Nucl. Data Tables, 79, 1
Lesaffre, P., Han, Z., Tout, C. A., Podsiadlowski, P., & Martin, R. G. 2006, MNRAS, 368, 187
Livio, M. 2000, in Type Ia Supernovae, Theory and Cosmology, ed. J. C. Niemeyer & J. W. Truran (Cambridge: Cambridge Univ. Press), 33
Mannucci, F., Della Valle, M., & Panagia, N. 2006, MNRAS, 370, 773
Neill, J. D., et al. 2009, ApJ, 707, 1449
Nomoto, K., Saio, H., Kato, M., & Hachisu, I. 2007, ApJ, 663, 1269
Nomoto, K., Thielemann, F.-K., & Yokoi, K. 1984, ApJ, 286, 644
Oda, T., Hino, M., Muto, K., Takahara, M., & Sato, K. 1994, At. Data Nucl. Data Tables, 56, 231
Phillips, M. M. 1993, ApJ, 413, L105
Phillips, M. M., Lira, P., Suntzeff, N. B., Schommer, R. A., Hamuy, M., & Maza, J. 1999, AJ, 118, 1766
Pinto, P. A., & Eastman, R. G. 2000, ApJ, 530, 744
Piro, A. L., & Bildsten, L. 2008, ApJ, 673, 1009
Piro, A. L., & Chang, P. 2008, ApJ, 678, 1158
Raskin, C., Scannapieco, E., Rhoads, J., & Della Valle, M. 2009, ApJ, 707, 74
Röpke, F. K. 2006, in Reviews in Modern Astronomy, Vol. 19, ed. S. Roeser (Wenheim: Wiley-VCH), 127
Röpke, F. K., Gieseler, M., Reinecke, M., Travaglio, C., & Hillebrandt, W. 2006, A&A, 453, 203
Seitenzahl, I. R., Röpke, F., Fink, M., & Pakmor, R. 2010, MNRAS, in press (arXiv:1005.5071)
Seitenzahl, I. R., Townsley, D. M., Peng, F., & Truran, J. W. 2009, At. Data Nucl. Data Tables, 95, 96
Straniero, O., Domínguez, I., Imbriani, G., & Piersanti, L. 2003, ApJ, 583, 878
Stritzinger, M., Mazzali, P. A., Sollerman, J., & Benetti, S. 2006, A&A, 460, 793
Timmes, F. X., Brown, E. F., & Truran, J. W. 2003, ApJ, 590, L83
Townsley, D. M., Calder, A. C., Asida, S. M., Seitenzahl, I. R., Peng, F., Vladimirova, N., Lamb, D. Q., & Truran, J. W. 2007, ApJ, 668, 1118
Townsley, D. M., Jackson, A. P., Calder, A. C., Chamulak, D. A., Brown, E. F., & Timmes, F. X. 2009, ApJ, 701, 1582
Travaglio, C., Hillebrandt, W., Reinecke, M., & Thielemann, F. 2004, A&A, 425, 1029
Truran, J. W., Arnett, W. D., & Cameron, A. G. W. 1967, Can. J. Phys., 45, 2315
Woosley, S. E., Kasen, D., Blinnikov, S., & Sorokina, E. 2007, ApJ, 662, 487

Chapter 4

Effect of the Central Density - Paper II

This chapter is a reproduction of the second paper I wrote on the problem of the central density dependence of SNeIa, and is a follow-up to Krueger et al. (2010); see Chapter 3. This paper has been accepted by the Astrophysical Journal (Krueger et al., 2012). In this paper I present additional details of the models and analysis that had to be omitted from Krueger et al. (2010) due to length restrictions of the Letters format. Additionally, I present new analysis of those results and extend the conclusions based on the new analysis. This paper is reproduced by permission of the American Astronomical Society. The co-authors directed and supervised the research that forms the basis for this paper.

Preprint typeset using LaTeX style emulateapj v. 12/14/05

EVALUATING SYSTEMATIC DEPENDENCIES OF TYPE IA SUPERNOVAE: THE INFLUENCE OF CENTRAL DENSITY

Brendan K. Krueger[1,2], Aaron P. Jackson[2,3], Alan C. Calder[2,4], Dean M. Townsley[5] Edward F. Brown[6,7], Francis X. Timmes[7,8]

Submitted to the Astrophysical Journal 2012 February 13

ABSTRACT

We present a study exploring a systematic effect on the brightness of type Ia supernovae using numerical models that assume the single-degenerate paradigm. Our investigation varied the central density of the progenitor white dwarf at flame ignition, and considered its impact on the explosion yield, particularly the production and distribution of radioactive ^{56}Ni, which powers the light curve. We performed a suite of two-dimensional simulations with randomized initial conditions, allowing us to characterize the statistical trends that we present. The simulations indicate that production of Fe-group material is statistically independent of progenitor central density, but the mass of stable Fe-group isotopes is tightly correlated with central density, with a decrease in the production of ^{56}Ni at higher central densities. These results imply progenitors with higher central densities produce dimmer events. We provide details of the post-explosion distribution of ^{56}Ni in the models, including the lack of a consistent centrally-located deficit of ^{56}Ni, which may be compared to observed remnants. By performing a self-consistent extrapolation of our model yields and considering the main-sequence lifetime of the progenitor star and the elapsed time between the formation of the white dwarf and the onset of accretion, we develop a brightness-age relation that improves our prediction of the expected trend for single degenerates and we compare this relation with observations.

Subject headings: hydrodynamics — nuclear reactions, nucleosynthesis, abundances — supernovae: general — white dwarfs

1. INTRODUCTION

Type Ia supernovae (SNeIa; singular SNIa) are bright, transient astronomical events identified by a peak-light spectrum showing no evidence of hydrogen but absorption lines of singly-ionized silicon (Minkowski 1941; Filippenko 1997). These events follow from explosive thermonuclear burning of degenerate stellar material composed principally of C and O, which synthesizes $\sim$0.6M$_\odot$ of radioactive ^{56}Ni. The decay of this ^{56}Ni powers the light curve (Truran et al. 1967; Colgate & McKee 1969; Arnett 1982; Pinto & Eastman 2000).

The progenitor systems of these explosions remain the subject of considerable debate and active research. Observations, however, indicate these events largely form a homogeneous class. Phillips (1993) identified a relationship between the maximum B-band magnitude of an event and its rate of decline. This "brighter equals broader" relationship has been extended to additional bands with templates from nearby events, allowing these events to be calibrated as an extension of the astronomical distance ladder (see Jha et al. 2007 for a description). This property, along with the brightness of SNeIa, which makes them visible over great distances, enables the use of SNeIa to probe the structure and expansion history of the universe, allowing studies of various cosmological models' parameters (Riess et al. 1998; Perlmutter et al. 1999; Albrecht et al. 2006; Kirshner 2010), with recent work constraining cosmological parameters to within a few percent (Riess et al. 2011; Sullivan et al. 2011). Recent observational studies of SNeIa have begun to correct for correlations of the brightness of a SNIa with properties of the host galaxy (Conley et al. 2011). Many SNIa observations are restricted to broadband photometry, so knowledge of host galaxy properties is correlated. The inability to deconvolve these properties from each other is among the larger sources of uncertainty in cosmological constraints from SNeIa, so advancing the understanding of how brightness correlates with host galaxy properties may contribute significantly to reducing the uncertainties of cosmological parameters.

The brightness, and therefore "broadness", of a SNIa is determined principally by the amount of ^{56}Ni synthesized during the explosion. Observations report that SNeIa appear to have an intrinsic scatter of a few tenths of a magnitude after calibration, forcing a minimum uncertainty in any distances measured by using SNeIa as standardizable candles (Jacoby et al. 1992; Kirshner 2010). An important goal of theoretical research into SNeIa, from the standpoint of cosmology, is to understand the sources of scatter and to identify potential systematic biases by studying the effects of various properties on the mechanism and nucleosynthetic yield of the SNIa. The surrounding stellar population, the metallicity and mass of the progenitor, the thermodynamic state of the progenitor, the cooling and accretion history of the progenitor, and other parameters are known to affect the lightcurves of SNeIa; the role of these "secondary" parameters is the subject of considerable study (e.g., Röpke et al. 2006; Höflich et al. 2010). Additionally, many of these effects may be interconnected in complex ways (Domínguez et al. 2001; Lesaffre et al. 2006; Townsley et al. 2009).

[1] email: brendan.krueger@stonybrook.edu
[2] Department of Physics & Astronomy, The State University of New York - Stony Brook, Stony Brook, NY, USA
[3] present address: Laboratory for Computational Physics and Fluid Dynamics, Naval Research Laboratory, Washington, DC, USA
[4] New York Center for Computational Sciences, The State University of New York - Stony Brook, Stony Brook, NY, USA
[5] Department of Physics and Astronomy The University of Alabama, Tuscaloosa, AL, USA
[6] Department of Physics and Astronomy, Michigan State University, East Lansing, MI, USA
[7] The Joint Institute for Nuclear Astrophysics, Notre Dame, IN, USA
[8] School of Earth and Space Exploration, Arizona State University, Tempe, AZ, USA

Observational campaigns are gathering information about SNeIa at an unprecedented rate. Scannapieco & Bildsten (2005) and Mannucci et al. (2006) showed that the delay time (elapsed time between star formation and the supernova event) data are best fit by a bimodal delay time distribution (DTD) with a prompt component that tracks less than 1 Gyr after star formation and a tardy component that occurs several Gyr later. Gallagher et al. (2008) demonstrate a correlation between brighter SNeIa and shorter delay times, which they state is consistent with the bimodality described by Mannucci et al., but also with a continuous relation. Howell et al. (2009), Neill et al. (2009) and Brandt et al. (2010) also find such a correlation between the delay time and brightness of a SNIa. While the degeneracy of age and metallicity in observations could obscure these correlations, Howell et al. (2009) note that the scatter in brightness of this observed relation is unlikely to be explained by the effect of metallicity.

For this theoretical study, we adopt the model known as the single-degenerate paradigm. This model assumes that a SNIa is the result of a thermonuclear disruption of a white dwarf (WD) in a mass-transferring binary system with either a main-sequence or red-giant companion star (see Branch et al. 1995; Filippenko 1997; Hillebrandt & Niemeyer 2000; Livio 2000; Röpke 2006; Li et al. 2011; Nugent et al. 2011; Bloom et al. 2012, and references therein). Recent observational evidence, however, suggests other progenitors such as the merging of two white dwarfs may explain many events (Scalzo et al. 2010; Yuan et al. 2010). In the single-degenerate scenario, the WD is formed when the primary star goes through a giant phase and expels a planetary nebula. Once the primary becomes a WD, it is initially not in contact with the companion star, and it slowly cools as thermal energy is radiated away. Once the companion star evolves and fills its Roche lobe, mass-transfer begins to carry low-mass elements from the envelope of the companion to the surface of the WD. If the accretion rate exceeds $\sim 10^{-7}$ $M_\odot$ yr^{-1}, the H-rich material can steadily burn (Nomoto et al. 2007) and the WD gains mass, which heats and compresses the WD, driving up both the temperature and density in the core. Once the temperature rises enough for carbon burning to begin, the core of the WD begins to convect; this is known as the "simmering" phase. This simmering phase lasts on order of 10^3 yr, and ends when a flame is ignited, which occurs approximately when the eddy turnover time becomes shorter than the local nuclear runaway time. Our initial models attempt to parameterize the WD at the end of the simmering phase, just at the beginning of the thermonuclear deflagration, which will in turn cause an explosion that will disrupt the entire WD in a SNIa.

The explosion mechanism we use (within the single-degenerate paradigm) is that of a deflagration to detonation transition (DDT). After ignition, the flame propagates as a subsonic deflagration for a while and then transitions to a supersonic detonation that rapidly consumes the star (Blinnikov & Khokhlov 1986; Woosley 1990; Khokhlov 1991; Hoflich et al. 1995; Höflich & Khokhlov 1996; Khokhlov et al. 1997; Niemeyer & Woosley 1997; Hoeflich et al. 1998; Niemeyer 1999). We describe the details of our implementation of this explosion mechanism below.

In the single-degenerate paradigm, a longer delay time can be explained by a longer elapsed time between the formation of the WD and the onset of accretion. During this period, the WD is in isolation and cools, hence the moniker the "WD cooling time" ($\tau_{\rm cool}$). Following the cooling time is a period of accretion, during which the WD is compressed and heats, approaching the conditions for ignition of the thermonuclear runaway. The decrease in temperature during the cooling time, which is determined by $\tau_{\rm cool}$, influences the density structure of the WD just prior to ignition, with a longer $\tau_{\rm cool}$ resulting in a higher central density when the core reaches the ignition temperature (Lesaffre et al. 2006). Thus, a correlation between central density and the brightness of an event would suggest a correlation between delay time and the brightness of an event.

In this manuscript, we expand on our earlier investigation on the effect of $\tau_{\rm cool}$ on the brightness of the explosion. In Krueger et al. (2010) we reported that as the central density of the progenitor WD increases, the production of radioactive ^{56}Ni decreases due to increased neutronization rates, producing a dimmer event. Using the results of Lesaffre et al. (2006), we related the WD central density to $\tau_{\rm cool}$ and were able to compare our results to the observations of Neill et al. (2009). Here we present additional details of our models; a statistical analysis of the results including the assessment of intrinsic scatter; the distribution of Fe-group elements within the remnant; and a potentially-observable effect to demonstrate the connection between age, progenitor central density, and brightness. We also revised our previously-reported trend in brightness with age to account for the main sequence evolution of the WD progenitor.

In Section 2 we discuss the methodology of our suite of simulations, followed by details of the code we used to perform our simulations in Section 3. We present the results of our simulations in Section 4, and discuss how these results compare with previous studies in Section 5. Section 6 contains a brief summary and final conclusions.

2. METHODOLOGY

As described above, our explosion models assume the DDT mechanism in which a flame ignited in the core propagates as a subsonic deflagration and then transitions to a detonation. We simulate an explosion from ignition through the detonation phase until burning effectively ceases. Our models are by necessity incomplete, however, in that we do not produce light curves and spectra with which we could compare to actual observations. Instead, we rely on the mass of ^{56}Ni synthesized in our models and compare this result from our simulations to ^{56}Ni masses inferred from observations (Howell et al. 2009).

For the study, we adopted the theoretical framework first applied in Townsley et al. (2009) for a statistical study of a suite of simulations performed with randomized initial conditions. We constructed a set of five progenitor models with different central densities ($\rho_{c,0}$), and therefore slightly different masses, and from these performed suites of two-dimensional simulations. For each progenitor model we applied thirty sets of initial conditions consisting of randomized perturbations on an initially-burned region. We refer to each of these thirty as a realization, each of which is seeded by a random number used to generate a unique power spectrum of spherical harmonics (see Appendix A for details of the realizations). The spectra are used as initial perturbations to a spherical "match head" in the center of the progenitor star. Each progenitor WD had the same seed values applied, resulting in the same thirty perturbations. This procedure allows us to characterize the intrinsic scatter in the models and check for systematic biases in the realizations across different progenitors, such as how the morphology of the initial conditions may influence the final result.

Complete details of our models and simulations follow, but

we preface the description by mentioning that one limitation of our study is the use of two-dimensional models and the parameterization of inherently three-dimensional phenomena. In particular, two-dimensional models lack any meaningful consideration of turbulence and its effect on the flame because the turbulence found in the interior of a simmering white dwarf and its interaction with the flame are inherently three-dimensional. The problem is compounded by the fact that this interaction occurs partially on unresolvable scales, necessitating use of sub-grid-scale models (see Schmidt et al. 2006a, for an example).

There are two critical ways that omitting consideration of turbulence influences this work. The first is in the calculation of flame speeds during the deflagration phase. The burning model (described below) relies on an input flame speed to propagate a model flame during the deflagration. Turbulence will interact with this flame, stretching it and thereby boosting the burning rate (see Schmidt et al. 2006a,b, and referenced therein). Our present models boost the input flame speed from tabulated laminar values to compensate for buoyancy effects (Townsley et al. 2009) but do not include the effect of turbulence-flame interactions for reasons discussed above. Effectively, we assume the increase in flame surface (and hence the burning rate) is dominated by stretching due to buoyancy rather than turbulence.

The second critical way that omitting consideration of turbulence influences this work is in the criteria for the DDT (see Seitenzahl et al. 2011, and references therein). For this study, we parameterized the DDT criterion as a threshold density, $\rho_{\rm DDT}$, with a detonation initiated when the top of a rising plume of burned material reaches this density. As we describe below, this threshold density determines the duration of the deflagration and thus strongly influences the outcome of an explosion. Our *a priori* choice for this parameter led to higher than expected yields of radioactive ^{56}Ni, necessitating a rescaling of our results for comparison to observations. Confirmation of the trends we present from extrapolated results awaits a future study with a more consistent treatment of these issues.

2.1. *Initial White Dwarf Models*

As demonstrated by Lesaffre et al. (2006), for a given zero-age main-sequence mass, the properties of a progenitor WD such as central temperature and density at ignition of the deflagration can be constructed as functions of $\tau_{\rm cool}$. We take the leading-order effect from varying $\tau_{\rm cool}$; that is, vary $\rho_{c,0}$ while holding all other parameters constant. This choice allows us to disentangle the effects of $\rho_{c,0}$ from the effects of other parameters. For our $\rho_{c,0}$, we chose $1-5\times10^9$ g cm^{-3} in steps of 1×10^9 g cm^{-3}. We then constructed a series of five parameterized WD progenitor models in hydrostatic equilibrium.

Figure 1 presents the profiles of the progenitor WDs in the ρ-T plane. The core of each WD is isentropic due to convection, the intermediate ("envelope") region is isothermal due to the high conductivity of degenerate matter, and the outer ("atmosphere") region has a power-law temperature dependence that was chosen to mimic a radiative atmosphere. For a model to explode, the central temperature must be in the range where the carbon burning begins a runaway, which is approximately $7-8\times10^8$ K. Varying the isothermal envelope temperature would have a relatively insignificant effect on the mass, as the envelope contains only a small fraction of the mass; primarily the mass is set by $\rho_{c,0}$. Thus we have chosen a central temperature at the low end of the carbon ignition range and allow the total mass to vary as a function of $\rho_{c,0}$. Table 1 shows the total mass ($M_{\rm tot}$) and mass of the isentropic core ($M_{\rm core}$) for each progenitor.

TABLE 1: Central densities, masses, and radii of progenitor WDs.

$\rho_{c,0}$ (g cm^{-3})	$M_{\rm tot}$ (M$_\odot$)	$M_{\rm core}$ (M$_\odot$)	R (km)
1×10^9	1.345	1.180	2500
2×10^9	1.368	1.162	2076
3×10^9	1.379	1.144	1852
4×10^9	1.385	1.131	1716
5×10^9	1.389	1.121	1604

TABLE 2: Composition of the progenitor WDs.

isotope	mass fraction	
	core	envelope
^{12}C	40%	50%
^{16}O	57%	48%
^{22}Ne	3%	2%

The core of each WD has a lower C/O ratio than the envelope; this is primarily due to the composition of different regions of the star at the end of the asymptotic giant branch (AGB) phase and the subsequent mixing of these regions, with additional contributions from the consumption of C during the simmering phase (Straniero et al. 2003; Piro & Bildsten 2008; Chamulak et al. 2008; Piro & Chang 2008). Our parameterized models for this study assume a fixed carbon abundance. As we plan to also study the dependence on central carbon abundance, we have maintained a clear separation between the central-density and the carbon-abundance studies by varying only central density and not the core carbon fraction. The composition discontinuity between the core and the envelope causes a temperature discontinuity (Piro & Chang 2008), shown by the short vertical line segments between the core and the envelope in Figure 1. The composition is listed in Table 2. We use ^{22}Ne as a placeholder to represent the neutron-rich isotopes present in a SNIa. The abundance of ^{22}Ne is calibrated to achieve the electron-to-baryon ratio of the material present in a SNIa, but sedimentation effects are not included. See Jackson et al. (2010), specifically Section 2, for a more detailed discussion.

2.2. *Ensemble of Simulations*

The thirty unique realizations for each of our five progenitor models, consisting of a set of perturbations on the initially-burned region, allowed us to perform a suite of 150 two-dimensional, axisymmetric simulations of SNeIa. A simulation begins with a region of burned material at the center of the star with the perturbation from sphericity given as spherical harmonics with a prescribed range of $12\leq\ell\leq16$ and random amplitudes; the amplitudes for each realization are shown in Appendix A. Each realization has a unique seed (for the random number generator), allowing each realization to be applied to the five progenitor models. Figure 2a shows two example perturbations that span the space of the random perturbations. Realization 21, on the left, is representative of the "spikiest" initial conditions; i.e., the greatest deviation from the mean radius. Realization 10, on the right, is representative of the "smoothest" initial conditions; i.e., the smallest deviation from the mean radius.

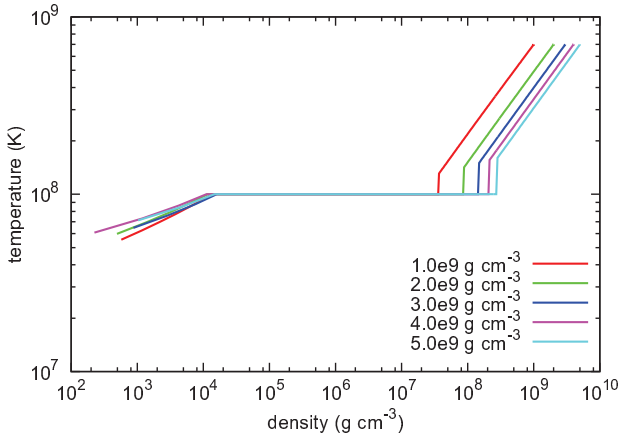

FIG. 1.—: The structure of our progenitor WDs in ρ-T space. Below $\sim 10^4$ g cm^{-3} is the power-law atmosphere. In the center of the figure is the isothermal envelope, with the same temperature for all progenitors. In the upper right region of the figure is the adiabatic core; all 5 progenitors are isentropic in this region, but the value of the entropy varies between progenitors.

3. THE SIMULATION CODE

The simulations were performed using a customized version of the FLASH code[9], an Eulerian adaptive-mesh compressible hydrodynamics code developed by the ASC/Alliances Center for Astrophysical Thermonuclear Flashes at the University of Chicago (Fryxell et al. 2000; Calder et al. 2002). The equation of state (EoS) that we use is the fully-ionized electron-ion plasma EoS (Timmes & Swesty 2000; Fryxell et al. 2000). The version of FLASH used here is the same as that used in Jackson et al. (2010). Customizations perform two main functions: First to implement the energy release due to explosive carbon-oxygen fusion, in both deflagration and detonation propagation modes, as well as a provision for a transition from deflagration to detonation. Second, criteria for mesh refinement that capture the important physics with a suitable degree of efficiency. Details of various components are given by Townsley et al. (2007), Townsley et al. (2009), and Jackson et al. (2010), with important additional and supporting information on implementation of some pieces of physics in Calder et al. (2007) and Seitenzahl et al. (2009b).

As mentioned in the introductory material, the simulations implement a multi-dimensional version of the deflagration-to-detonation transition model, in which the flame is born as a subsonic deflagration and later transitions to a supersonic detonation (Blinnikov & Khokhlov 1986; Woosley 1990; Khokhlov 1991; Hoflich et al. 1995; Höflich & Khokhlov 1996; Khokhlov et al. 1997; Niemeyer & Woosley 1997; Hoeflich et al. 1998; Niemeyer 1999). The initial conditions prescribe the deflagration at the start of a simulation. As the deflagration proceeds, the flame is subject to fluid instabilities (Figure 2b), and when the top of a rising bubble reaches the threshold density, it is assumed to transition into a supersonic detonation (Figures 2c and 2d; see Section 3.1.2 for details of the transition). See Townsley et al. (2009), Maeda et al. (2010), Jackson et al. (2010), Röpke et al. (2011), Seitenzahl et al. (2011), and references therein for examples of recent work assuming this explosion mechanism.

[9] available from http://flash.uchicago.edu

3.1. *Burning Model*

Since the carbon-oxygen fusion occurring in SNeIa proceeds to nuclear statistical equilibrium (NSE), in which all reactions among all nuclides are, to good approximation, fast relative to the hydrodynamic timescales, the nuclear processing necessarily involves a large number of reactions and nuclides. This is especially true when calculating e^- capture on Fe-group elements (IGEs), as the overall effective e^- capture rate is a combination of contributions from captures on a wide variety of nuclides with comparable individual rates. As explored in our earlier work (Calder et al. 2007; Townsley et al. 2007; see also Khokhlov 2000), it is possible to abstract the burning process from hundreds of nuclides to just a few fluid state variables with appropriately chosen reaction dynamics and energetics computed using a large set of nuclides. This enables tremendous gains in computational efficiency, making 3-d simulations and extensive 2-d studies such as this feasible.

Our burning model consists of three reaction progress variables that describe conversion between four states. The first state is the initial, unburned mixture of ^{12}C, ^{16}O, and ^{22}Ne (representing general neutron excess, as described in section 2.1), which we call fuel. The second state is the result of the ^{12}C fusing to roughly Si-group elements, which we call ash. The third state is the result of the remaining ^{16}O burning to Si-group elements, which we call nuclear statistical quasi-equilibrium (NSQE) material. The fourth and final state is the result of NSQE material relaxing to nuclear statistical equilibrium (NSE), containing mostly IGEs. The three reaction progress variables are

ϕ_{fa}	Carbon consumption, fuel to ash
ϕ_{aq}	Oxygen consumption, ash to NSQE
ϕ_{qn}	Conversion of Si-group to Fe-group, NSQE to NSE.

Each variable evolves from 0 (unburned) to 1 (fully burned). We also require that $\phi_{fa} \geq \phi_{aq} \geq \phi_{qn}$ to enforce the time-ordering of the four states. A given cell will have mass fractions $1-\phi_{fa}$ of fuel, $\phi_{fa}-\phi_{aq}$ of ash, $\phi_{aq}-\phi_{qn}$ of NSQE material, and ϕ_{qn} of NSE material.

While a large portion of the energy release occurs in the consumption of ^{12}C, the final NSE state is not, during the explosion, energetically inert. The NSE state is one in which the distribution of nuclides in the fluid, and therefore the average nuclear binding energy, is determined by the fluid state. That is, it participates in the EoS of the fluid, releasing or absorbing energy as the pressure and density of the fluid change. As a result, a significant portion of the energy release for some fluid elements occurs well after the "fully burned" NSE state has been reached. The reaction kinetics used are given in Jackson et al. (2010). We track several material properties in the fully burned material, including the electron-to-baryon ratio (Y_e), ion-to-baryon ratio ($Y_{\rm ion}$), and average nuclear binding energy per baryon ($\overline{q}$).

Our treatment of matter in NSE allows for the effects of weak reactions, specifically electron captures, which serve to deleptonize the material. Weak processes (e.g. electron capture) are included in the calculation of the energy input rate, as are neutrino losses, which are calculated by convolving the NSE distribution with the weak interaction cross sections. Both the NSE state and the electron capture rates were calculated with a set of 443 nuclides (Seitenzahl et al. 2009b). Weak cross sections were taken from Fuller et al. (1985), Oda et al. (1994), and Langanke & Martínez-Pinedo (2001), with

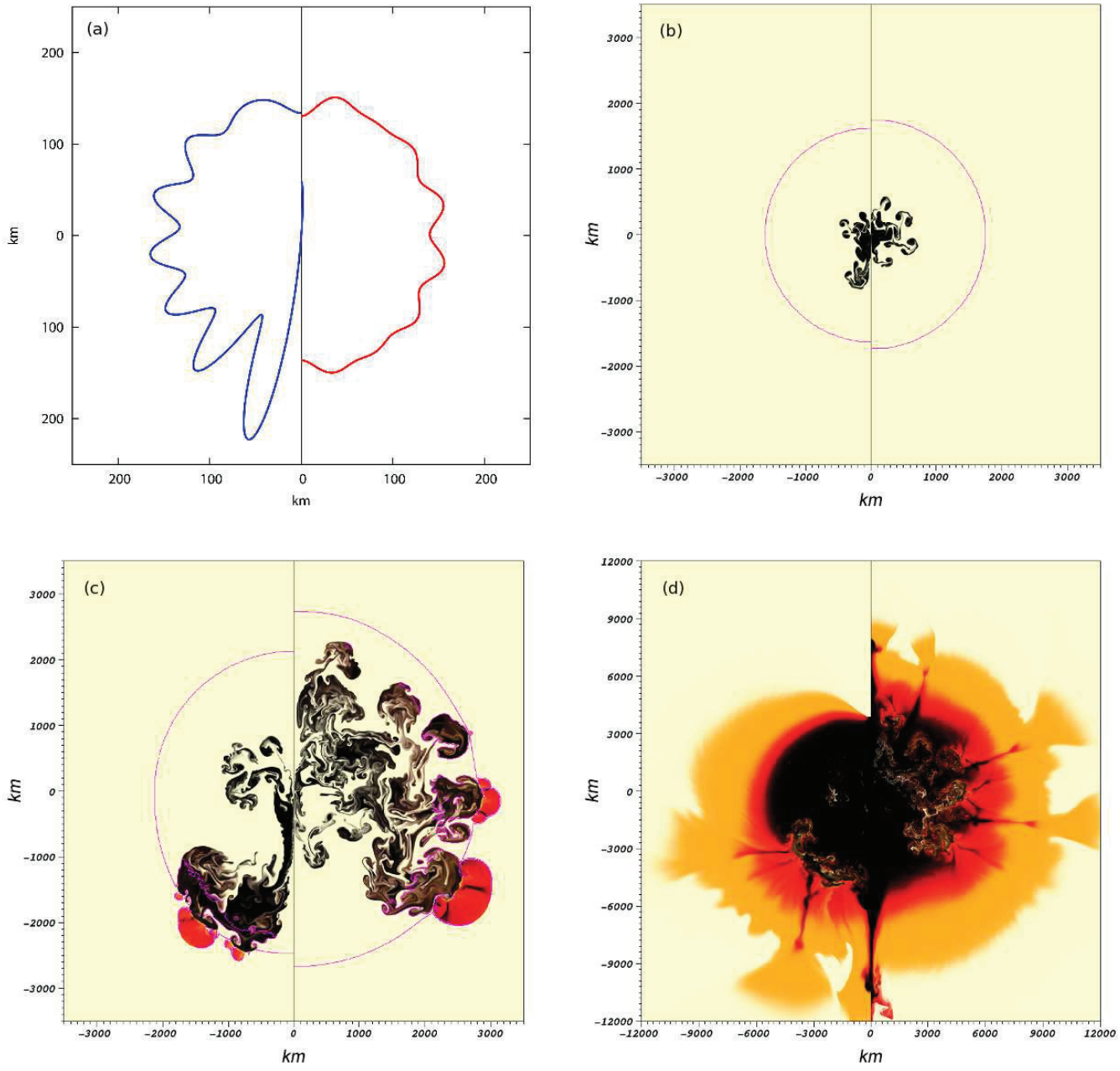

FIG. 2.—: Illustrations of the phases of the DDT model of a SNIa; each panel displays two of our realizations: 21 (left) and 10 (right). Panel 2a shows the initial flame surfaces; realization 21 has the greatest deviation from the mean radius, and realization 10 has the least deviation from the mean radius. Panels 2b – 2d are snapshots from our simulations, with $\rho_{c,0} = 3 \times 10^9$ g cm^{-3}; Panel 2b shows the early deflagration phase, Panel 2c shows the first DDT events, and Panel 2d shows the later detonation phase. The colors represent the four stages of the burning model discussed in Section 3.1: cream represents unburned fuel, gold represents ash from carbon burning, red represents material in NSQE, and black represents material in NSE. Only in the detonation stage do the three burning processes separate out spatially; they are co-located during the deflagration. Our simulations extend to $\sim 6.5 \times 10^8$ km, but these images show only the inner regions; the spatial scale varies between panels, with only panels 2b and 2c having the same spatial extent in order to illustrate the expansion that occurs during the deflagration phase.

newer rates superseding earlier ones.

The treatment of electron capture is critical to the dynamics for three reasons. First, NSE is a dynamic equilibrium and the composition of material in NSE evolves as the thermodynamic state evolves and/or Y_e changes. Binding energy can be released if the equilibrium evolves toward more tightly bound nuclei, which changes the local temperature. Second, the reduction in Y_e lowers the Fermi energy, reducing the primary pressure support of this highly degenerate material and having an impact on the buoyancy of the neutronized material. Finally, neutrinos are emitted (since the star is transparent to them) so that some energy is lost from the system.

By using the progress variables defined above and the local Y_e, we can derive a local estimate for the abundance of ^{56}Ni. As was done in Townsley et al. (2009), we estimate the ^{56}Ni abundance by assuming that the first IGE material made as neutronization occurs is equal parts by mass ^{54}Fe and ^{58}Ni. The local mass fraction of ^{56}Ni is estimated by

$$Y_{e,n} = \frac{Y_e - (1-\phi_{qn})Y_{e,f}}{\phi_{qn}}$$
$$X_{^{56}\mathrm{Ni}} = \max\left[\phi_{qn}\frac{Y_{e,n}-0.48212}{0.5-0.48212}, 0\right], \quad (1)$$

where $Y_{e,f}$ is the electron fraction in the unburned fuel and 0.48212 is the electron fraction of material that is equal parts by mass ^{54}Fe and ^{58}Ni. This should be a modestly accurate estimate of the ^{56}Ni production because the dynamics of the progress variable ϕ_{qn} have been calibrated to reproduce, in hydrodynamics, the production of IGEs during incomplete silicon burning seen in direct calculations (Zeldovich, Von Neumann, Döring; ZND; e.g. Khokhlov 1989) of steady-state detonations. When realization 2 from Jackson et al. (2010) with $\rho_{\mathrm{DDT}} = 10^{7.1}$ g cm^{-3} is post-processed with a nuclear network, the ^{56}Ni yield from Equation (1) is within 2% of that determined by the post-processing. More detailed study of the accuracy of computed yields under various conditions is the subject of separate, ongoing work.

3.1.1. *Deflagration*

Even at our highest resolution (4 km), the flame front is unresolved. To handle this we use an artificial, resolved reaction front that is governed by the advection-diffusion-reaction (ADR) equation (Khokhlov 1995; Vladimirova et al. 2006), with special features to ensure that the front is stable and acoustically quiet (Townsley et al. 2007). Our ADR front is chosen to be resolved over about 4 computational cells in order to obtain acceptably low acoustic noise as it propagates across the grid and releases energy. This creates an extended "partially burned" region that requires some specialized treatment. In such regions, particularly at high density, we say that the material is well-separated into unburned and fully-burned material divided by a thin flame. However the spatial resolution cannot capture this and the average over a mixture of fully burned and unburned results a "partially-burned" state. Thus we have to make estimates of the correct thermodynamic state of the two cases (unburned and fully burned) mixed together within the region.

Additionally, we enforce a minimum flame speed in order to prevent the flame from being torn apart by Rayleigh-Taylor-induced turbulence. The minimum flame speed is

$$S_{\mathrm{min}} = 0.5\sqrt{Agm\Delta}, \quad (2)$$

where A is the Atwood number, g is the local acceleration of gravity, Δ is the width of the grid cell, and m is an adjustable parameter, set to 0.04 for these simulations. The flame speed is set by

$$S = \max(S_{\mathrm{min}}, S_{\mathrm{lam}}). \quad (3)$$

The Atwood number and the laminar flame speed, S_{lam}, are both functions of the local, unburned density estimate and the composition. The Atwood number varies by less than 0.01% due to the amount of ^{22}Ne present so it is tabulated for a representative, constant ^{22}Ne fraction.

3.1.2. *DDT*

At present, the physical mechanism by which a DDT in degenerate supernova material occurs is an area of current research (see Röpke 2007; Seitenzahl et al. 2009a; Woosley et al. 2009; Schmidt et al. 2010; Poludnenko et al. 2011, and references therein). Simulations of supernovae involving a DDT assume it occurs via the Zeldovich-gradient mechanism (Khokhlov et al. 1997, but see also Niemeyer 1999), in which a gradient in reactivity leads to a series of explosions that are in phase with the velocity of a steadily propagating detonation wave. Many authors suggest that when the flame reaches a state of distributed burning, which is when turbulence on scales at or below the laminar flame width are fast enough to dominate transport processes (see, e.g., Pope 1987), fuel and ash are mixed and the temperature of the fuel is raised and "prepared" in such a way to produce the required reactivity gradient. A requirement for distributed burning is that the ratio of turbulent intensity to the laminar flame speed must exceed some unknown threshold, which is still actively researched (Niemeyer & Woosley 1997; Khokhlov et al. 1997; Golombek & Niemeyer 2005; Röpke & Hillebrandt 2005; Aspden et al. 2008, 2010; Poludnenko & Oran 2011a,b). Entrance into the distributed burning regime does not guarantee such a reactivity gradient to form. Woosley (2007) and Woosley et al. (2009) studied incorporating more stringent requirements for these conditions to be met.

In the context of supernova models, the ratio of turbulent intensity to laminar flame speed changes most rapidly due to the change in laminar flame properties, which are strongly dependent on fuel density. Therefore, DDT is assumed to occur at a range of densities that vary somewhat but generally lie in the range of $10^{6.7}$ to $10^{7.7}$ g cm^{-3} (Khokhlov et al. 1997; Lisewski et al. 2000; Woosley 2007; Röpke & Niemeyer 2007; Bravo & García-Senz 2008; Maeda et al. 2010; Jackson et al. 2010). We choose to ignite detonations where the flame reaches a specific density, $\rho_{\mathrm{DDT}} = 10^{7.1}$ g cm^{-3}, which puts us somewhere in the middle of that range, consistent with a number of studies on this subject. We note that while parameterizing the DDT criteria by only density omits effects such as background turbulent intensity and density gradients, our choice of one threshold is intended to keep such variables constant so that we can isolate and investigate the effect of varying the central density.

The choice of ρ_{DDT} increases or decreases the duration of the deflagration phase, which increases or decreases the amount of expansion prior to the detonation and hence the yield of IGEs. A companion study of the effects of varying ρ_{DDT} as a proxy for metallicity under the same statistical ensemble we use here indicated a slight over-production of ^{56}Ni at this choice of ρ_{DDT} (Jackson et al. 2010), a result borne out by this study. The DDT transition is implemented by burning small regions ahead of rising plumes. When a plume reaches ρ_{DDT}, a circular region with a radius of 12 km is selected 32 km radially outward from the point where the rising

plume reaches the transition density. The reaction progress variables in this region are then instantly increased to a fully-burned state. This method conserves energy, as the detonation is initiated by the sudden release of energy from the conversion of fuel to NSE, not by an unphysical addition of extra energy. Each plume is limited to ignite no more than 2 – 3 detonations, with a minimum separation distance of 200 km imposed between detonation points. The full details of this algorithm are given in Section 3.2 of Jackson et al. (2010).

Previous studies using this DDT mechanism found that DDT points with a 12 km radius successfully generated detonations in all simulations performed. However, our simulations showed that this size DDT point is not as robust for this study. One of our simulations ($\rho_{c,0} = 1.0 \times 10^9$ g cm^{-3}, realization 8) deviated from the behavior of the other 149 simulations and inspection showed that the first plume to reach $\rho_{\rm DDT}$ ignited several DDT points that did not propagate as detonations; the first detonation to actually propagate ignited when the second plume reached $\rho_{\rm DDT}$ significantly after (and beneath) the first plume to reach $\rho_{\rm DDT}$. The failure of the detonation of the first plume to reach $\rho_{\rm DDT}$ led to significantly more expansion of the WD prior to the subsequent detonation, which led to some or all of the material burning at a lower density than it should have, and the corresponding suspect yields. Thus we removed this simulation from our suite and performed the analysis on the remaining 149 points. Even if this "failed DDT" simulation is included, the results presented in this paper change by no more than a few percent.

3.2. *Mesh Refinement*

Refinement is based on gradients in ρ and ϕ_{fa}, subject to the limits imposed below. We define three types of regions, subject to different refinement limits:

1. fluff (f): regions with $\rho < \rho_{\rm fluff}$
2. star (*): non-energy-generating stellar material, $\rho > \rho_{\rm fluff}$
3. energy generation (eg): regions with $\epsilon_{\rm nuc} > \epsilon_{\rm eg}$ or $\dot{\phi}_{\rm fa} > \dot{\phi}_{\rm fa,eg}$

where $\phi_{\rm fa}$ is the reaction progress variable from the ADR equation, and $\epsilon_{\rm eg}$ and $\dot{\phi}_{\rm fa,eg}$ are parameters equal to 10^{18} erg g^{-1} s^{-1} and 0.2 s^{-1} respectively. These limits are chosen so that all actively propagating flames or detonation fronts are at the highest resolution. We establish a minimum cell size for refinement of each type of region such that $\Delta_f > \Delta_* > \Delta_{\rm eg}$. We use $\Delta_{\rm eg} = 4$ km, $\Delta_* = 16$ km and Δ_f to be as large as allowable. FLASH only allows adjacent subdomains of the mesh to be of fixed size (we use 16×16 cells) and to differ by a single refinement level (a factor of 2 in resolution). These were found to be the lowest resolutions which gave converged results in 1-d simulations (Townsley et al. 2009).

Fluff is the low-density area outside of the star; we choose $\rho_{\rm fluff} = 10^3$ g cm^{-3}. The FLASH code cannot properly handle empty (zero-density) regions, so these regions are set to some low, but non-zero, density so that they will not affect the dynamics of the star. To avoid rapidly cycling the refinement-derefinement of a region, a small amount of hysteresis is introduced near the limits for refinement changes, so that, for example, a refinement of grid resolution is not immediately derefined as a result of slight changes due to the necessary interpolation.

4. RESULTS

The results presented here build on the initial results presented in Krueger et al. (2010) and extend the analysis beyond what was shown there. The explosions occur in two main phases, the deflagration phase (from ignition until the first DDT occurs) and the subsequent detonation phase. The principal difference is that during the deflagration phase, the star has time to react to the energy release. Accordingly, the evolution is naturally divided by the time at which the first DDT event occurs, which we define as $t_{\rm DDT}$; this duration also describes the time spent in the deflagration-dominated phase of the SNIa evolution. We also define $t_{\rm IGE}$ as the time when the production of IGEs ceases. This is the time at which burning ceases, and by this time the NSE state is no longer evolving due to freezeout; thus energy release has effectively ceased by $t_{\rm IGE}$. However, our models have not yet entered into free expansion by this time. For the purpose of our simulations, $t_{\rm IGE}$ also measures the duration of the entire SNIa event. We found that the duration of the deflagration phase ($t_{\rm DDT}$) decreases with increasing density and is less sensitive to density as the density increases, while the duration of the detonation phase (equal to $t_{\rm IGE} - t_{\rm DDT}$) is very nearly constant for all simulations, with a mean of 0.476 s and a standard deviation of 0.065 s.

The table in Appendix C presents the masses of ^{56}Ni and IGEs at $t_{\rm DDT}$ and $t_{\rm IGE}$. Recall from Table 1 that the total mass and the mass of the convective core both change with density, but the variations are only of a few percent. Thus, we believe that effects from variations in the total or convective core masses are negligible. The results and trends we describe follow from variations in the central density and the variations in initial conditions from realization to realization. Also, as discussed in Section 3 of Krueger et al. (2010), the choice of the DDT transition density in our simulations led to an overproduction of ^{56}Ni. Essentially, our models are systematically too bright, but we believe that our trends are valid. Jackson et al. (2010) investigated the role of DDT density in our models and found that the production of ^{56}Ni is very sensitive to the choice of DDT density. This choice determines the duration of the deflagration phase, which determines the amount of expansion and, accordingly, the density profile of the star during the detonation and the yield. Future studies will be better calibrated based on these results.

4.1. *Evolution*

Figure 3 shows the evolution of the gravitational binding energy and the mass of IGEs for the five simulations performed using realization 5, each with a different $\rho_{c,0}$. During the deflagration-dominated phase, higher-$\rho_{c,0}$ progenitors experience faster burning, thus expanding the star faster due to the faster energy release. This effect can be seen by the rapid drop of the binding energy for the higher-density simulations around 0.5 s in the upper panel. The transition to a detonation in higher-$\rho_{c,0}$ progenitors occurs sooner. Once the first DDT event occurs, the production of IGEs proceeds much faster than in the deflagration phase, as may be seen by the sudden increase of the slope in the lower panel after the detonation occurs.

During the detonation phase the drop in binding energy is similar for all densities. During this same period the curves of the IGE mass stay ordered, with the differences between them following principally from the difference in $t_{\rm DDT}$. The nonlinear morphological dependencies come into play as the

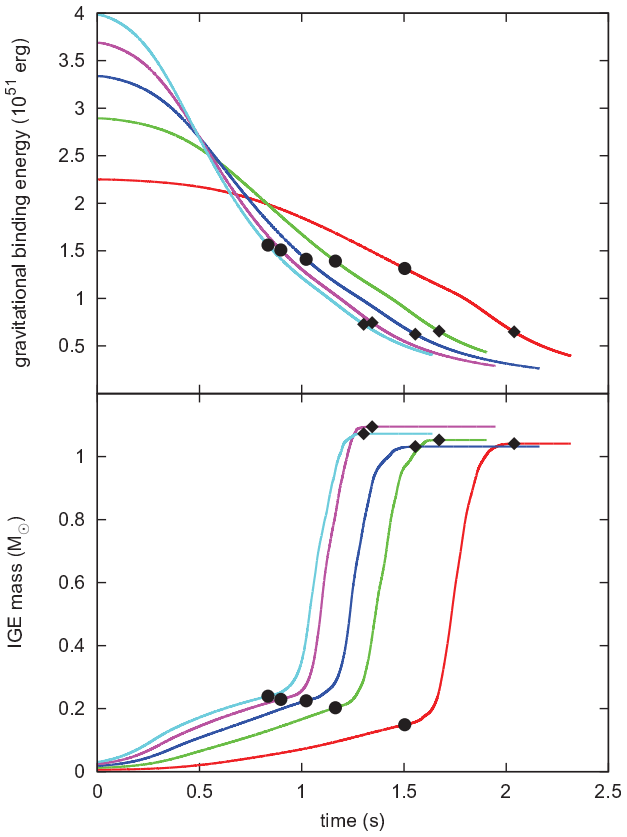

FIG. 3.—: Sample curves showing the evolution of the gravitational binding energy and the mass of IGEs over the duration of a simulation. These curves all use realization 5. Curves are colored by $\rho_{c,0}$: 1.0×10^9 g cm^{-3} (red), 2.0×10^9 g cm^{-3} (green), 3.0×10^9 g cm^{-3} (blue), 4.0×10^9 g cm^{-3} (magenta), 5.0×10^9 g cm^{-3} (cyan). The times $t_{\rm DDT}$ and $t_{\rm IGE}$ are marked by black circles and black diamonds respectively.

detonation slows and then stops; the total IGE yield plateaus to a constant value, but that value is not (for a single realization) correlated with the central density of the progenitor. The leveling off of the mass of IGEs, due to the cessation of burning, is apparent in the lower panel. The time $t_{\rm IGE}$ was calculated for each simulation by finding the point at which the IGE mass changes by less than 0.01% over the preceding 0.01 s.

4.2. *Statistics*

We showed in Krueger et al. (2010) (see especially Figure 2) that a single initial morphology is, in general, insufficient to capture trends in SNeIa due to the nonlinearities involved in the explosion process. This observation invites the question of how many initial morphologies are necessary to obtain statistically-meaningful trends from the simulations. Figure 4 presents the standard deviation of ^{56}Ni yield as a function of the number of realizations, with the realizations added in the order presented in Appendix A. Shown are the standard deviations for each of the five central densities of the study. The obvious evolution of the standard deviation until approximately 15 realizations are included in the average shows that a statistically meaningful average requires approximately 15 realizations. From this result, we conclude that our our sample of 30 realizations per central density is sufficient to fully characterize the statistical trends we present. The choice of

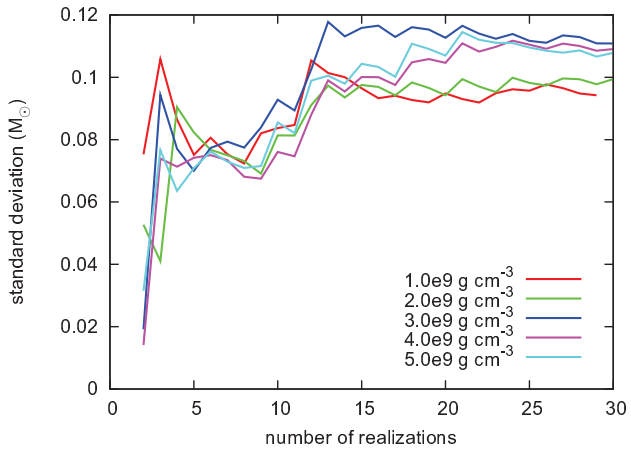

FIG. 4.—: Plot of the standard deviation of ^{56}Ni yield as a function of the number of realizations, added in the order listed in Appendix A, for each of the five central densities of the study. The standard deviation of the ^{56}Ni mass converges around 15 total realizations.

30 realizations allows us to go somewhat beyond characterizing the variation in the sample, allowing us to reduce our uncertainty on the sample mean.

This result, the need for an average over an ensemble of simulations for determining statistically-meaningful trends, is critical to the analysis of our study. Because the results discussed in this paper come from a statistical analysis of our simulations, the results presented here generally cannot be applied predictively to individual SNeIa, but only apply statistically to large sets of SNeIa. Exceptions to this rule will be noted explicitly.

4.3. *Initial Morphology Correlations*

We explored whether properties of the initial flame morphology correlate with the final result. We find that "spikier" initial flame surfaces, that is initial morphologies that appear to have a small number of large amplitude perturbations, give rise to faster plume growth and less expansion, and, therefore, a higher yield of IGEs and ^{56}Ni. Several quantities were tested as measures of the morphology of "spikiness", and each gave the same qualitative result. For example, Figure 5 plots the final yield of IGEs as a function of the maximum radius of the initial flame surface and standard deviation of the initial flame radius.

As illustrative cases, consider Figure 2. The right panels shows realization 10, $\rho_{c,0} = 3 \times 10^9$ g cm^{-3}, which is a very smooth initial flame surface; this same realization is outlined by a black square in Figure 5. The smooth configuration results in several rising plumes approaching $\rho_{\rm DDT}$, and these multiple plumes burn a larger fraction of the star and release more energy than a single plume would during its rise to $\rho_{\rm DDT}$. The net effect is an increase in both $t_{\rm DDT}$ and in the amount of expansion at $t_{\rm DDT}$, leaving less mass at densities high enough to burn to IGEs during the detonation phase. Contrast this with the left panels of Figure 2, showing realization 21, $\rho_{c,0} = 3 \times 10^9$ g cm^{-3}, which is a very spiky initial flame surface; this same realization is outlined by a black circle in Figure 5. For this case, a single plume is dominant over all other features of the initial flame surface and rapidly accelerates towards $\rho_{\rm DDT}$ with little competition. This gives a short deflagration phase, and burns a lower fraction of the star prior to the detonation (see especially Figure 2c). These two

effects result in less expansion at $t_{\rm DDT}$, leaving more mass at a density high enough to burn to IGEs during the detonation, resulting in a greater yield of IGEs and ^{56}Ni.

In the center of each panel of Figure 5, the trend is not so clear. Realization 24 (outlined by black diamonds) is a good example of the lack of a clear trend in this intermediate range. The initial flame surface for realization 24 has multiple large spikes, so that it has a larger than average maximum radius and radial standard deviation, and would be considered a spiky case. However, most of these spikes are of comparable maximum radius, and none of these features develops into a dominant plume, as is typical of the spiky cases; instead, the plumes grow together and the behavior is like that of the smooth cases. Thus realization 24 leads to high values of $t_{\rm DDT}$ and low yields of IGEs and ^{56}Ni relative to simulations of similar spikiness. Thus the intermediate range does not show a strong trend, while the extreme ranges (multiple competing plumes starting from a smooth initial surface, or a single dominant plume with no significant competition) show the trend more clearly.

4.4. *Yields*

Figure 6 shows the masses of IGEs and ^{56}Ni produced in the 149 simulations that were analyzed, along with the ^{56}Ni-to-IGE mass ratio. The figures plot yield vs. central density and also show average yields and standard deviations at each central density, with best-fit trend lines. The mass of IGEs is consistent with a flat line; i.e., it is independent of $\rho_{c,0}$. However, the mass of ^{56}Ni decreases with increasing $\rho_{c,0}$. The significant scatter in the two masses is readily apparent; the mean standard deviations for the IGEs and ^{56}Ni masses are 0.108 $M_\odot$ and 0.105 $M_\odot$, respectively. As discussed in Mazzali & Podsiadlowski (2006) and Woosley et al. (2007), assuming a constant IGE mass and varying the ^{56}Ni mass produces SNeIa that lie approximately along the observed width-luminosity relationship, while the width of the relationship allows the IGE mass to vary somewhat (c.f. Figures 15 and 20 of Woosley et al. 2007). We note that the masses of IGEs and in particular the masses of ^{56}Ni from our simulations are on average higher than accepted results for masses synthesized in actual SNIa events (see Woosley et al. 2007, and references therein).

The ^{56}Ni-to-IGE mass ratio decreases with increasing $\rho_{c,0}$, as would be expected from a constant IGE mass and a decreasing mass of ^{56}Ni. However, unlike the constant standard deviations of these two masses, the standard deviation of the ^{56}Ni-to-IGE mass ratio increases with $\rho_{c,0}$. The variation in the ^{56}Ni-to-IGE ratio is dominated by variation related to neutronization: because neutronization can exaggerate differences that arise in the hydrodynamics, we find that the standard deviation (variation) increases with the total mass of stable IGEs synthesized

Additionally, we found that the yield from burning during the deflagration phase is substantially different from the yield during the detonation phase. Figure 7 shows the yields of stable IGEs and ^{56}Ni during the deflagration and detonation phases. The trend of increasing stable IGE yield and decreasing ^{56}Ni yield with increasing central density is most obvious in the deflagration phase yield. We interpret this result as following from the fact that the detonation phase involves burning at densities that are typically lower than those of the deflagration phase due to expansion of the star during the deflagration phase. The neutronization rate increases with density, so it shows up most strongly in the deflagration phase before significant expansion occurs.

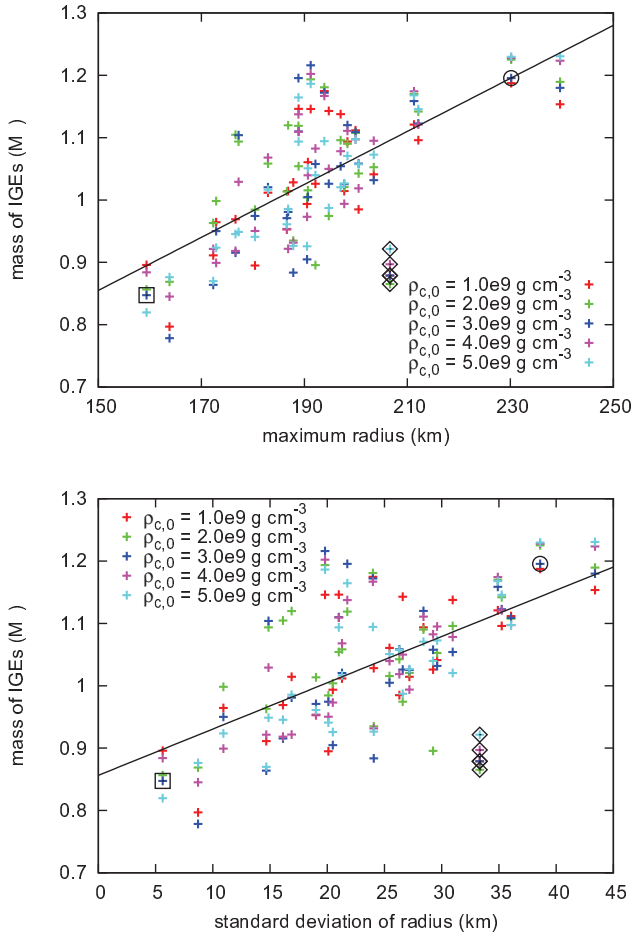

FIG. 5.—: Plots of the mass of IGEs as functions of the maximum initial flame radius and the standard deviation of the initial flame radius, both being treated as measures of how spiky the initial flame surface is, with simulations colored by $\rho_{c,0}$. The black square marks realization 10 and the black circle marks realization 21, both with $\rho_{c,0} = 3 \times 10^9$ g cm^{-3}. These two simulations are shown in Figures 2a – 2d, and are examples of extreme cases: very smooth (realization 10) and very spiky (realization 21). Black diamonds mark realization 24, an example which runs counter to the general trend, and a good illustration of the ambiguity of the intermediate regions of these plots.

4.5. *Distribution of* ^{56}Ni

The principal result from a simulation is the mass of ^{56}Ni synthesized in the explosion, which directly sets the brightness of an event. The synthesized ^{56}Ni masses are listed in Appendix C. The next question to be answered in the analysis concerns the distribution of ^{56}Ni in the remnant. Figure 8 presents radially-averaged profiles of ^{56}Ni for three of the five central densities ($\rho_{c,0} = 1 \times 10^9$, 3×10^9, and 5×10^9). Also shown are representative results from realizations 4, 12, 13, and 29 for comparison. The radial profile of ^{56}Ni mass fraction varies between simulations, but certain details are consistent across the ensemble. The inner 0.8 – 1.0 M$_\odot$ has a high ^{56}Ni mass fraction; we refer to this region as the "plateau", although there can be significant variation within this region. Outside of the plateau, there is a smooth decrease to a ^{56}Ni

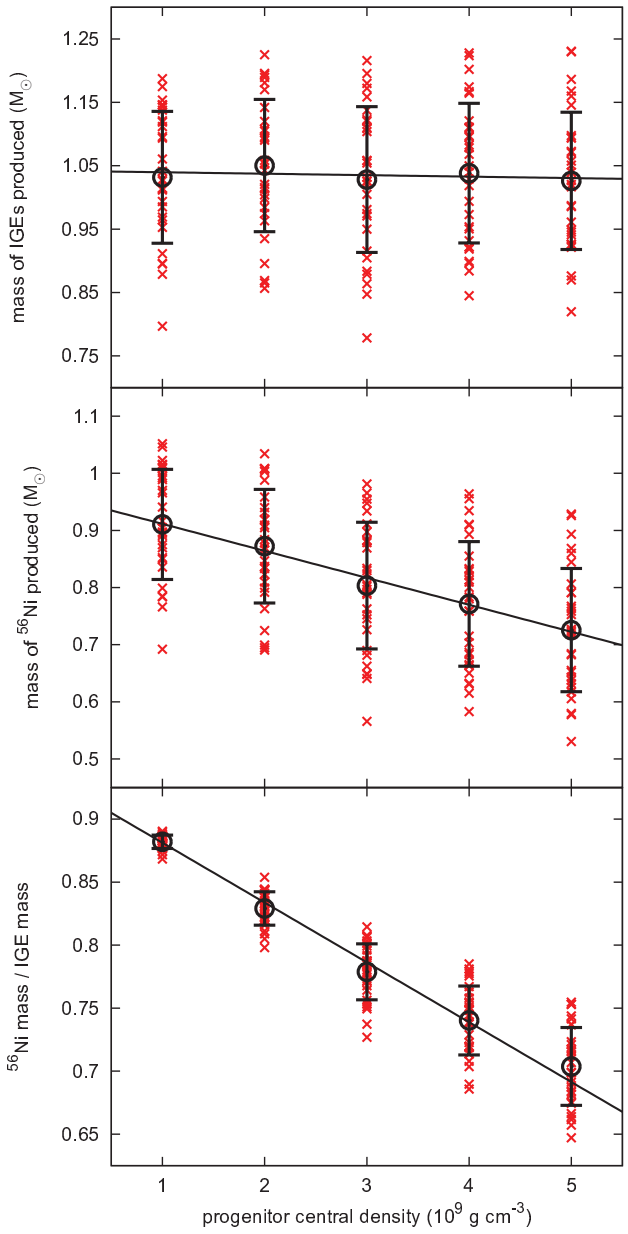

FIG. 6.—: Final yields (at $t_{\rm IGE}$) of our simulations plotted against $\rho_{c,0}$. The black lines are the best-fit trend lines, with the averages and standard deviations marked by the circles and the vertical error bars.

mass fraction at or near zero at the surface of the WD; we refer to this as the "decline" region. It appears that this decline region may not be fully relaxed to the final profile at time $t_{\rm IGE}$, but may experience some steepening prior to entering the free-expansion phase. Lower-$\rho_{c,0}$ simulations have less neutronization and therefore generate more ^{56}Ni. For these simulations the ^{56}Ni mass fraction in the plateau tends to cluster near the maximum value (~ 0.9), with some deviations down as far as ~ 0.6. The higher-$\rho_{c,0}$ simulations have more neutronization and therefore generate less ^{56}Ni, so the typical ^{56}Ni mass fraction in the plateau shows more variation and there exist larger deviations from the mean (down to ~ 0.2).

The representative realizations presented in Figure 8 demonstrate the deviation from mean behavior. In particular, the representative realizations show "typical" behavior

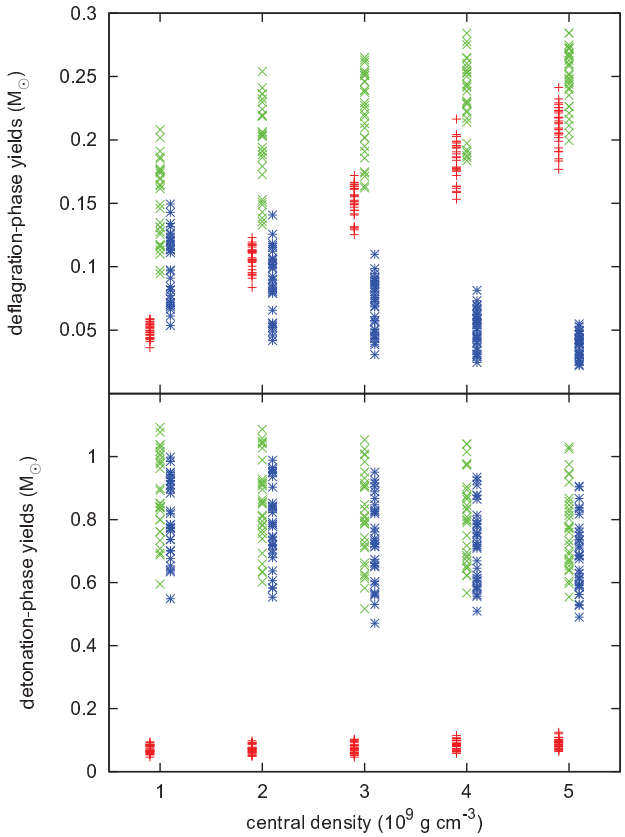

FIG. 7.—: Plots of the masses of stable IGEs (red pluses), ^{56}Ni (blue asterisks), and total IGEs (green crosses) produced during the deflagration phase (top panel) and the detonation phase (bottom panel). The symbols for each mass have been horizontally shifted slightly so the symbols do not overlap.

(the ^{56}Ni profile nearly matches the mean profile), over- and under-luminous models, and ^{56}Ni holes (patches within the plateau with significantly less ^{56}Ni than the surrounding regions). Previous studies have reported the presence of a ^{56}Ni hole in the inner region (Höflich et al. 2010). The green and red curves in the bottom panel of Figure 8 (realization 4) illustrate such a ^{56}Ni deficit, although the deficit is offset from the center of the WD in the case of the red curve. Most of our simulations do not show evidence of this ^{56}Ni hole in the inner region. Only a few simulations have such a feature, with ^{56}Ni holes being more common in simulations with a higher $\rho_{c,0}$. Turbulent mixing caused by the burning processes breaks the symmetries that give rise to a consistent central ^{56}Ni hole in 1-d simulations.

Figure 9 shows the distributions of ^{56}Ni, stable IGEs, and non-IGE material for the four sample cases shown in Figure 8c ($\rho_{c,0} = 5 \times 10^9$). For our results, the mass of stable IGEs is approximated by any IGE material that is not ^{56}Ni. The figures present the inner 6000 km of the domain, and for all cases the bulk of IGEs appears in the plotted region. The distributions indicate that ^{56}Ni holes can be caused by incompletely-burned regions (for example, on the axis of Figure 9c just below the equator) or by neutronized regions (for example, adjoining the previously-mentioned incompletely-burned region of Figure 9c, or the band at a radius of ~ 2000 km in Figure 9a). The plume rise, velocity fields, and neutronization may be asymmetric, which is seen especially in Figures 9a and 9d. The degree of asymmetry observed in our models

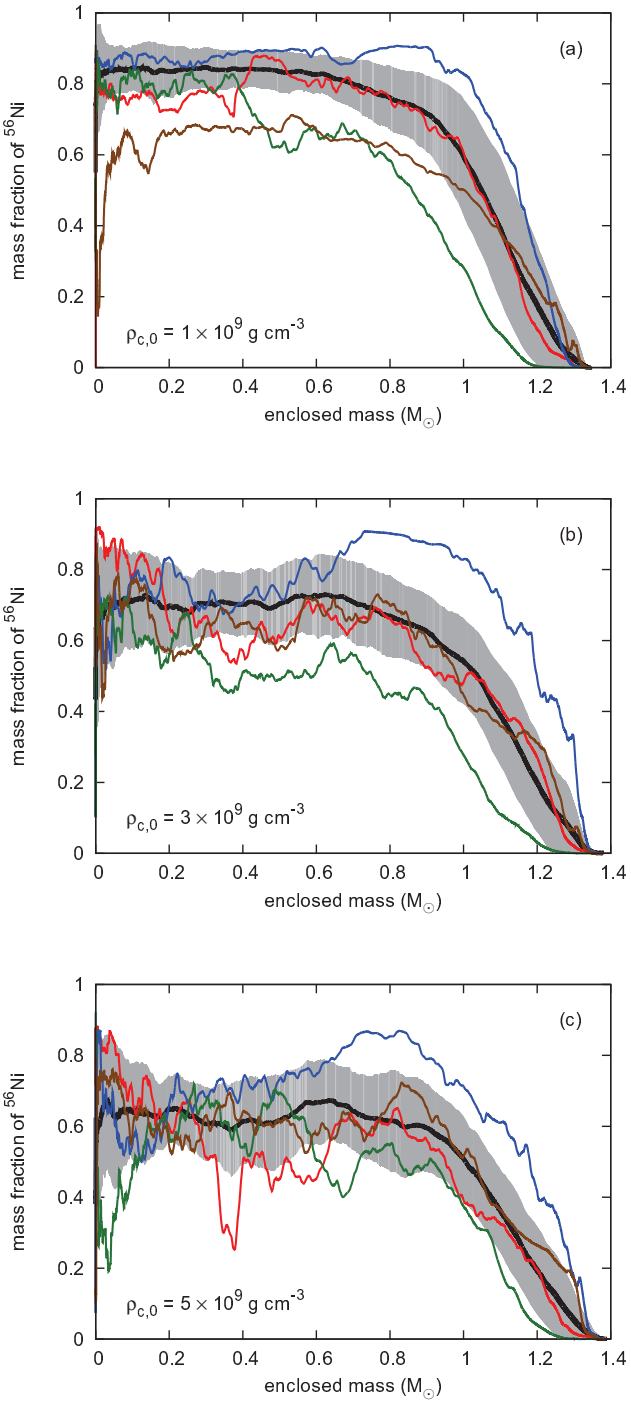

FIG. 8.—: Radially-averaged profiles of ^{56}Ni mass fraction at three central densities (1×10^9, 3×10^9, 5×10^9 g cm^{-3} in Panels 8a, 8b, and 8c respectively). The black curves show the mean profile of all simulations at a given $\rho_{c,0}$, with the grey band showing the standard deviation. The four colored curves represent four different realizations: 4 (red), 12 (blue), 13 (green), and 29 (brown).

suggests that there may be noticeable line-of-sight effects for SNeIa.

4.6. *Distinguishing Age Among SNeIa of Equal Brightness*

Can we extract from our results insight into the age of a progenitor WD given the brightness of the SNIa? From our results, one might conclude that the mass of stable IGEs ($M_{\rm stable}$) should increase with increasing $\rho_{c,0}$, and that the relation should have a large scatter (akin to the scatter in the ^{56}Ni and IGE relations). Figure 10 illustrates the relationship between $\rho_{c,0}$ and $M_{\rm stable}$, along with the best-fit trend and the scatter (the shaded region shows two standard deviations in each direction around the best fit curve through the data). The data show an increasing trend as expected, with the best fit being

$$\left(\frac{\rho_{c,0}}{10^9\ \mathrm{g\ cm^{-3}}}\right) = 35.4\left(\frac{M_{\rm stable}}{\mathrm{M}_\odot}\right)^2 + 6.92\left(\frac{M_{\rm stable}}{\mathrm{M}_\odot}\right) - 0.349\,. \quad (4)$$

Unlike the ^{56}Ni and IGE relations, however, there is a very small scatter in this relation for $M_{\rm stable}$, with a standard deviation of only 0.167×10^9 g cm^{-3}. This result is the tightest relation in our data, to the point where this relation can be meaningfully applied to a single event. This tight relationship is unlike all of our other relations, which only apply to the statistics of large ensembles.

Given observations of multiple SNeIa of the same brightness and a reliable measure of the mass of stable IGEs from the observations, our models predict that we can use Equation (4) to determine the relative ages of the progenitors. The relation provides the central density from observed masses of stable IGEs. Lesaffre et al. (2006) presents relations between the cooling time of the progenitor and the central density of the progenitor at the ignition of the thermonuclear runaway. Applying the relations of Lesaffre et al. (2006) to the central densities, our result allows determination of the cooling times the progenitor WDs experienced. Assuming the progenitors had the same main sequence mass, we thus obtain a measure of the relative ages of the progenitors. Because this result is derived from varying the central density of the progenitor, we are implicitly assuming that such a variation of $\rho_{c,0}$ is the dominant effect on the mass of stable IGEs. Future work in three dimensions will consider central density variation combined with other effects that may be related to age.

Our models, specifically the distribution of IGEs in the expanding remnant, offer insight into what would be required for observing the mass of stable IGEs. While our models exhibit a mild degree of asymmetry, we find systematic behavior of the distribution of heavy nuclei for events of a given brightness (or given mass of ^{56}Ni). Figure 11 shows profiles of ^{56}Ni and IGE mass fractions in three sets. Each set has a simulation at each of the five central densities, but the simulations within a set are chosen to have approximately the same integrated ^{56}Ni mass. Accordingly, the simulations within a set may not be from the same realization. These profiles are generated at $t_{\rm IGE}$, when the burning has essentially ceased, but not yet into the free-expansion phase.

The plateau (central region) exhibits a slight systematic behavior in Figure 11. Considering both the curves of ^{56}Ni and IGEs, we note a tendency of a less-well-defined plateau in the lowest-^{56}Ni-mass set (top panel). The start of the decline region occurs at a higher enclosed mass for simulations with a higher mass of ^{56}Ni; the plateau extends farther out. Also, there appears to be a mild trend in the plateau region of simulations within a set: the higher $\rho_{c,0}$ simulations (magenta and cyan curves) tend to show a wider plateau in the IGE mass fraction. In addition, we note that within these results, some simulations exhibit the ^{56}Ni hole while some do not. The hole may be observed in the drastic decreases of some curves at the lowest enclosed masses.

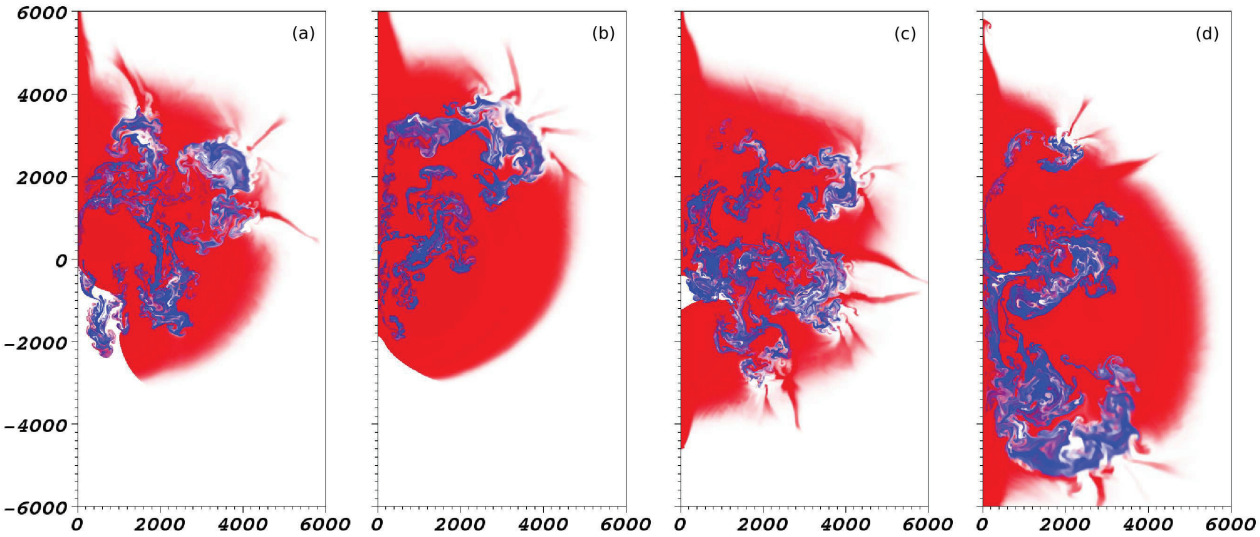

FIG. 9.—: Plots of the inner 6,000 km of four simulations at $t_{\rm IGE}$, showing mass fractions of ^{56}Ni (red), stable IGEs (blue), and non-IGE material (white). These are the same simulations plotted in Figure 8c, with $\rho_{c,0} = 5 \times 10^9$ g cm^{-3}; from left to right, the panels show a non-central ^{56}Ni hole (realization 4), an overluminous case (realization 12), an underluminous case with a central ^{56}Ni hole (realization 13), and a typical case (realization 29). The off-center ^{56}Ni deficit in realization 4 is due to a band of neutronized, stable isotopes caused by multiple plumes that have reached a common radius. The central ^{56}Ni hole in realization 13 is partially due to a neutronized region around the equator, and partially due to an incompletely-burned region near the axis, below the equator.

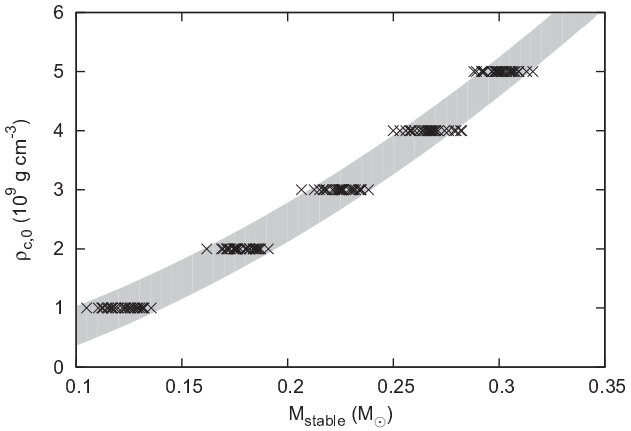

FIG. 10.—: Plot of $\rho_{c,0}$ vs. $M_{\rm stable}$. The shaded region displays two standard deviations around the model (Equation (4)).

We also may consider the distribution of the synthesized heavy elements within the models. Figure 12 shows the distribution of ^{56}Ni vs. stable IGEs for 3 of the simulations from Figure 11a. The densities of the three simulations ($\rho_{c,0}$ = 1×10^9, 3×10^9, and 5×10^9 g cm^{-3}) span the range of central density. The trend for more stable IGEs at higher $\rho_{c,0}$ can clearly be seen by the more extensive regions colored in blue, indicating higher mass fractions of stable IGEs. These 2-d plots also show that as $\rho_{c,0}$ increases, the ^{56}Ni and stable IGEs are more sharply segregated; there are more mixed regions (in shades of purple) in the lowest-$\rho_{c,0}$ simulation (Figure 12a).

5. DISCUSSION

The results presented above in Section 4 follow directly from our simulations and are as rigorous as can be within the limitations of our models (as described in Section 2). We may extend our results some in order to investigate the implications of our trends, particularly the decreasing proportion of ^{56}Ni with increasing central density. The principle result from one of our simulations is the mass of ^{56}Ni, and there are well-established relationships between the brightness of an observed thermonuclear supernova and the mass of ^{56}Ni synthesized during the explosion (see Woosley et al. 2007, and references therein). Thus our trends may have implications for the brightness of events. In this section, we explore these connections by comparing our trends in ^{56}Ni mass to ^{56}Ni masses inferred from observations.

In Krueger et al. (2010) (see especially Figure 4 of Krueger et al. (2010), an updated version of which is shown in Figure 14 of this paper), we showed that our results agree with the general trend of dimmer SNeIa from older stellar populations by comparing with observations from Neill et al. (2009). We improve upon that result with two additions: recalibration of the ^{56}Ni mass produced by our models and clarifying the definition of "age" by including a range of main sequence lifetimes. Additionally, this section discusses how our results compare to other studies considering the effect of $\rho_{c,0}$ on ^{56}Ni.

5.1. *Recalibration of* ^{56}Ni *Yield*

As discussed above, on average our suite of simulations exhibited an overproduction of IGEs and ^{56}Ni when compared to masses estimated from observations of remnants (Woosley et al. 2007). We estimate a correction to our ^{56}Ni masses, the details of which are given in Appendix B but which we summarize here, that allows us to more directly compare our results to ^{56}Ni masses inferred from observations.

The recalibration is based on relationships between model parameters and explosion yields found in previous studies. Jackson et al. (2010) found that higher values of $\rho_{\rm DDT}$ led to increased yields due to less expansion of the star during the deflagration phase. Townsley et al. (2009) found a correspondence between the mass at densities above 2×10^7 g cm^{-3} at $t_{\rm DDT}$ and the mass of IGEs synthesized in the yield (Figure 5).

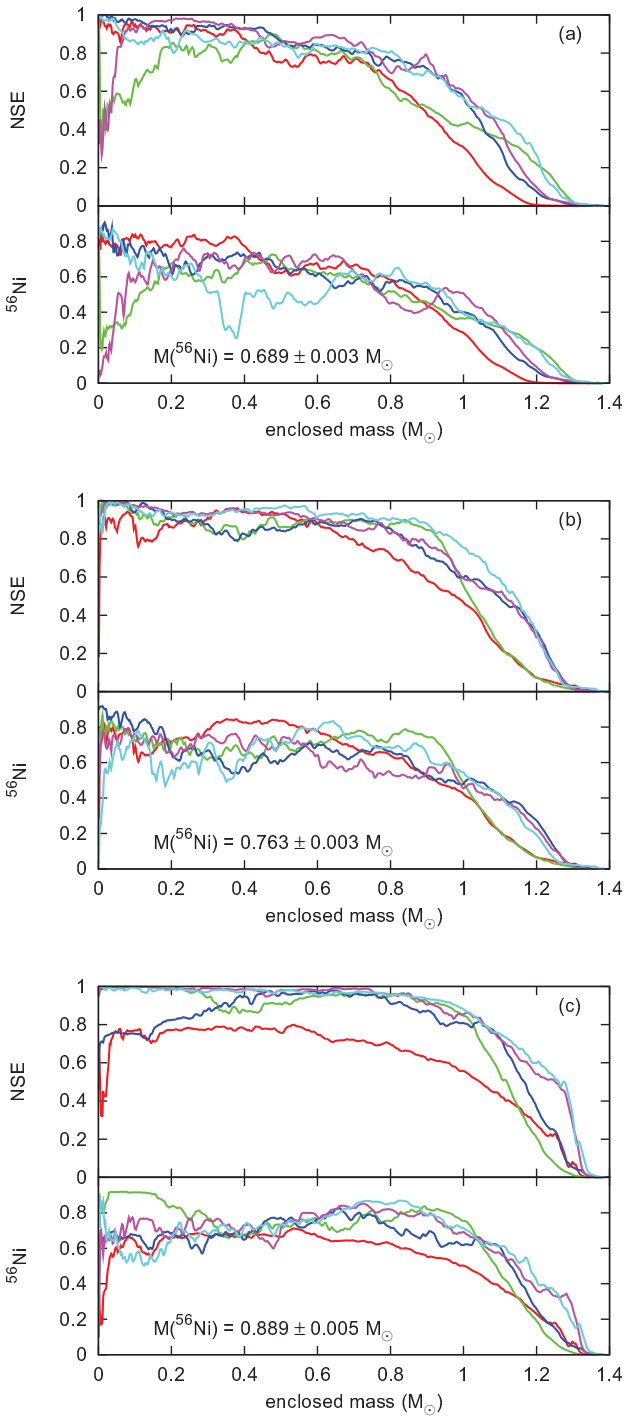

FIG. 11.—: Comparisons of radial profiles of ^{56}Ni and IGE mass fractions for models with nearly the same total mass of ^{56}Ni, but different values of $\rho_{c,0}$. The upper set of profiles has a mass of $0.689 \pm 0.003\ M_\odot$, the central set of profiles has a mass of $0.763 \pm 0.003\ M_\odot$, and the lower set of profiles has a mass of $0.889 \pm 0.005\ M_\odot$. Lines are colored by $\rho_{c,0}$: 1.0×10^9 g cm^{-3} (red), 2.0×10^9 g cm^{-3} (green), 3.0×10^9 g cm^{-3} (blue), 4.0×10^9 g cm^{-3} (magenta), 5.0×10^9 g cm^{-3} (cyan).

Although the correspondence found by Townsley et al. (2009) was not perfect, these two relationships form the basis for our re-scaling. We note that the rescaling assumes that even for lower values of $\rho_{\rm DDT}$, the mass of IGEs is independent of $\rho_{c,0}$; this assumption is discussed in greater detail in Appendix B based on the expansion characteristics present in our simulations. However, this is a critical assumption in our analysis and is based on a somewhat restricted parameter space and therefore is subject to future investigation to confirm it. Recent work by Seitenzahl et al. (2011), who performed full three-dimensional simulations covering the range of observed ^{56}Ni masses, suggests that this assumption does not hold. See section Section 5.3.

Performing this recalibration lowers the ^{56}Ni masses (see Figure 13), giving yields that are consistent with yields inferred from observations. A similar trend of decreasing ^{56}Ni mass with increasing central density is also found in these extrapolated results. Future models will extend to three dimensions and may include more physically-motivated initial conditions or more detailed burning models that capture interactions between the turbulent velocity field and the flame structure. Such changes will require that we re-evaluate our choice of model parameters, such as $\rho_{\rm DDT}$.

5.2. *Comparison to Observations*

One of the principal metrics that we extract from each simulation is the mass of ^{56}Ni produced, which is directly related to the brightness of an event. Using the method outlined in Howell et al. (2009), we converted stretch reported in observational results to ^{56}Ni masses to compare to the ^{56}Ni masses (derived in Section 5.1) obtained from our simulations. We then combined our central density values with the results of Lesaffre et al. (2006), which correlate the central density at the time of the ignition of the flame front to the cooling time of the progenitor WD, allowing us to express our results as ages. The results of Lesaffre et al. (2006) suggest that a WD with a central density of 1×10^9 g cm^{-3} will not ignite without further accretion, so for this comparison we neglect our simulations with that value of $\rho_{c,0}$. Our "age" was previously defined as the delay time ($\tau_{\rm cool}$), while the observational results used the delay time, which includes the main-sequence lifetime ($\tau_{\rm MS}$). We can improve our comparison by applying a shift to our data to account for $\tau_{\rm MS}$. We assume that our progenitors differ solely in their cooling times in order to separate out other effects; therefore we take $\tau_{\rm MS}$ to be constant across our results. Our best-fit line would now become

$$M_{^{56}\rm Ni} = \alpha \log_{10}(\tau_{\rm cool} + \tau_{\rm MS}) + \beta, \qquad (5)$$

where α and β are fitting parameters. Because the addition of $\tau_{\rm MS}$ is inside the logarithm, this corresponds not only to a shift but also an increasing slope. We have selected two estimated limiting values for $\tau_{\rm MS}$ (0.05 and 1.0 Gyr, corresponding to main-sequence masses of approximately 8.0 and 1.5 M$_\odot$respectively; see Hansen et al. 2004) and included them with the original $\tau_{\rm MS} = 0$ result in Figure 14. Adding in a $\tau_{\rm MS}$ consistent with our C/O progenitors brings our results into better agreement with the two right-most points of Neill et al. (2009).

As seen in Figure 14, our theoretical results are not in complete agreement with the observed data. Observationally, the age-brightness correlation may flatten at young ages, while our data do not, resulting in our data being overluminous relative to young SNeIa. This study isolated the effects of central density and related that to age assuming a constant main-

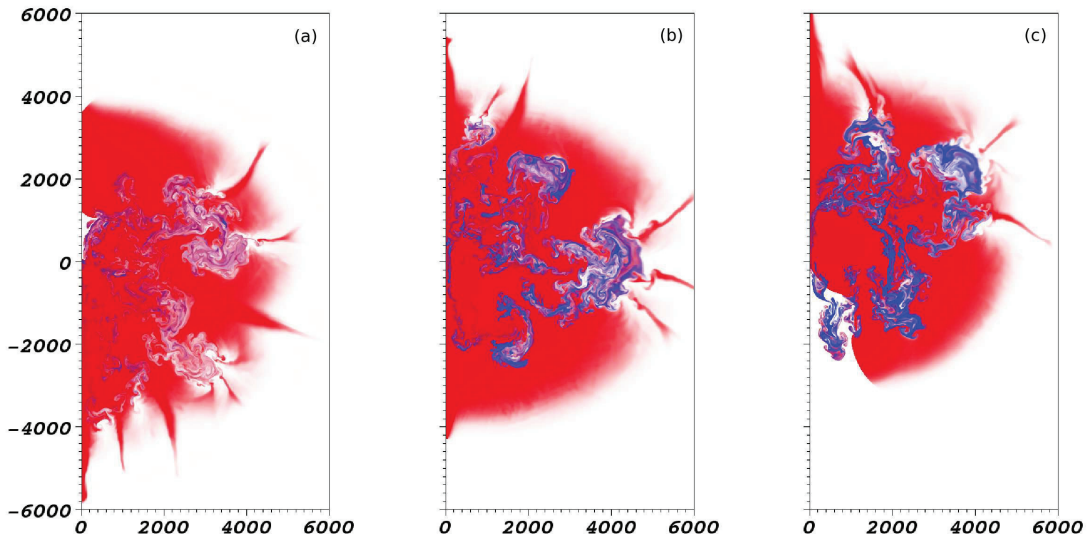

FIG. 12.—: Comparison of ^{56}Ni and stable IGE distributions at $t_{\rm IGE}$ for simulations with the same total ^{56}Ni mass. These images are generated from the same simulations used in Figure 11a. From left to right, the central densities are 1.0, 3.0, and 5.0 $\times 10^9$ g cm^{-3}. Red represents the mass fraction of ^{56}Ni, blue represents stable IGEs, and white represents non-IGEs. Axes are in kilometers. As $\rho_{c,0}$ increases (with constant ^{56}Ni), more IGEs are produced and less material is mixed (seen by the purple regions).

sequence mass, but there are other effects that may be correlated. Examples of such potentially correlated effects are: main-sequence mass and it's correlation with central density, metallicity of the progenitor, core ^{12}C fraction prior to ignition of the deflagration, sedimentation, and others. Inclusion of such effects may modify the results presented here and are the subjects of future work.

5.3. *Comparison to Other Theoretical Efforts*

Recent theoretical work by other research groups also addresses the role of central density in the single-degenerate picture of SNeIa. Fisher et al. (2010) note that in the gravitationally confined detonation model (GCD; Plewa et al. 2004), a higher central density leads to increased energy release during the deflagration phase, which leads to increased expansion of the star and an increase in the production of intermediate-mass elements and the corresponding decrease in IGEs. These results are consistent with our findings concerning the choice of $\rho_{\rm DDT}$ influencing the production of IGEs discussed above in Section 3.1.2. These results are also consistent with some of our realizations, but Fisher et al. (2010) do not consider the role of neutronization, preventing comparison to our principal result that the relative proportion of ^{56}Ni decreases with higher central density, producing a dimmer event.

Seitenzahl et al. (2011) performed a study of the DDT scenario with three-dimensional simulations and a description of the flame energetics that accounts for neutronization. Seitenzahl et al. (2011) similarly find that the ^{56}Ni fraction of IGEs decreases in WD models with higher central densities, but they also find that the mass of IGEs increases at higher densities. The net effect is a roughly constant mass of ^{56}Ni synthesized during the explosion, implying that central density influences the brightness of an event only as a secondary parameter. Seitenzahl et al. (2011) comment on differences between their results and our earlier results (Krueger et al. 2010) and, likewise, we offer discussion here.

First, we note that our results are more similar than they might at first appear. Our trend of decreasing ^{56}Ni follows from the increased rate of neutronization at high densities of a roughly constant mass of IGEs synthesized during the explosion. In a sense, our trend is consistent with that of Seitenzahl et al. (2011). For a given mass of IGEs, the fraction that is ^{56}Ni is lower in WD models with a high central density. The difference between our results and Seitenzahl et al. (2011) follows from the the increase in the mass of IGEs synthesized in their models. If our explosions produced more IGEs for higher central density progenitors, then we may well see a roughly constant mass of ^{56}Ni. This observation should be readily apparent by considering Figure 6. If the flat slope of the IGE yield were instead rising enough, the decreasing slope of the ^{56}Ni yield would be instead rising. Accordingly, the key to the differences in our results is understanding the reason for the difference in the production of IGEs.

While there are many differences between the methodology of Seitenzahl et al. (2011) and ours, including (as they mention) differences in the flame model (level set vs. ADR), differences in the energy release scheme, and structure of the computational mesh, perhaps the most substantive difference is the dimensionality of the simulations. Three-dimensional simulations meaningfully describe turbulent flow, which enables use of turbulence-flame interaction (TFI) models. Turbulence in two-dimensional simulations, however, has very different properties; particularly, it has an inverse-cascade of energy from small to large scales (see Chapter 10 of Davidson 2004, and references therein). Because of the large scope of this study, only two-dimensional simulations were possible. As described above, our models use a flame speed that compensates for buoyancy effects to prevent the flame from being torn apart by Rayleigh-Taylor-induced turbulence. Because of the issue of turbulence in two-dimensional simulations, we chose not to include models for unresolved turbulence and the turbulence-flame interaction in our models for this study.

In their three-dimensional simulations, Seitenzahl et al. (2011) similarly account for buoyancy effects, but also implement a method for accounting for turbulent energy on unresolved scales and the corresponding enhancement to the flame speed. Originally proposed by Niemeyer & Hillebrandt (1995) and developed in detail by Schmidt et al. (2006a,b),

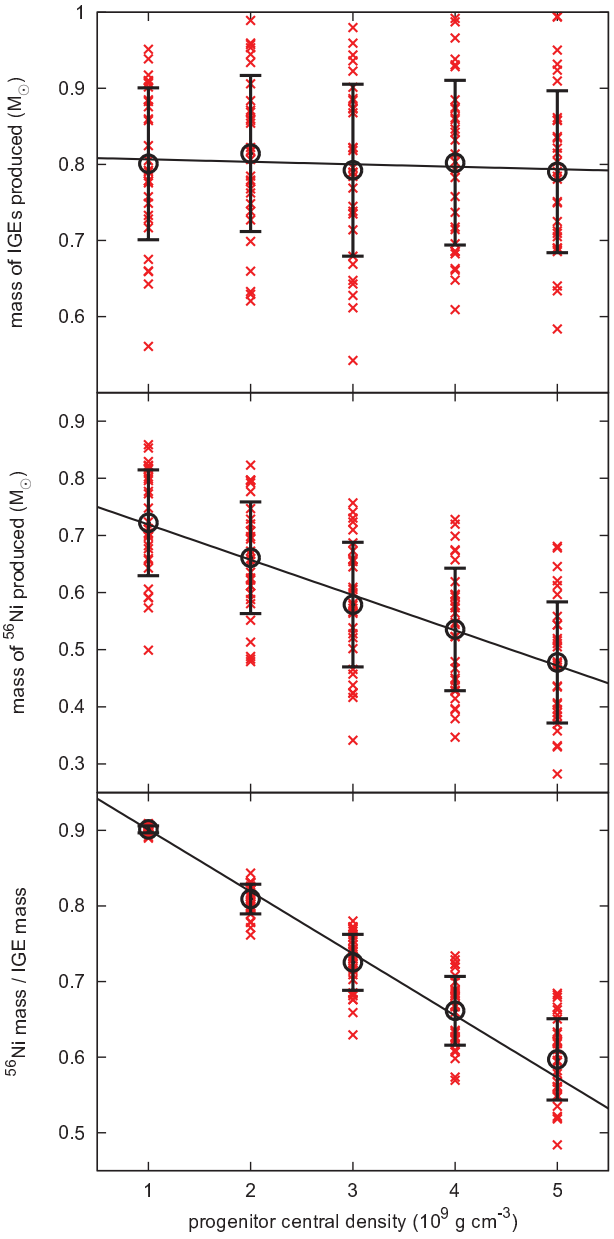

FIG. 13.—: Final yields of our simulations after recalibration using Equations (B2) and (B3), the parameter values given in Table B2, and the time shifts given in Table B3. The black lines are the best-fit trend lines, with the averages and standard deviations marked by the circles and the vertical error bars. These plots are directly analogous to those shown in Figure 6.

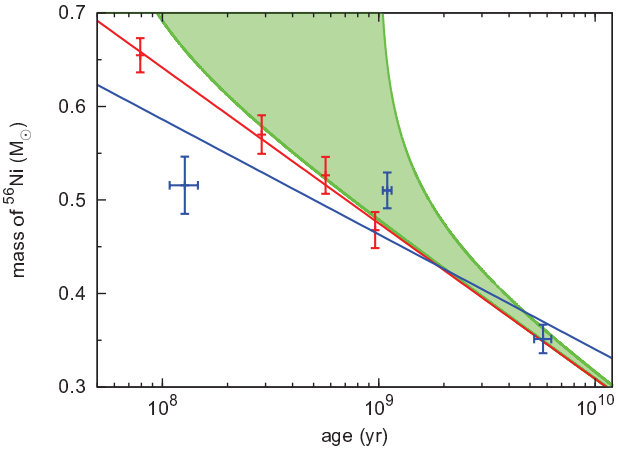

FIG. 14.—: Plot of $M_{^{56}\mathrm{Ni}}$ vs. age comparing the scaled results of this study to the ^{56}Ni masses inferred from the observations of Neill et al. (2009). In red are the points from this study with no shift (i.e., $\tau_{\mathrm{MS}} = 0$ Gyr), along with the standard error of the mean and a best-fit trend line following the form of Equation (5). The green shaded region shows our best-fit line with $\tau_{\mathrm{MS}} = 0.05 - 1.0$ Gyr. In blue are the binned and averaged points from Figure 5 of Neill et al. (2009), along with their best-fit trend line.

the method consists of a dynamic measure of the local turbulent energy on sub-grid scales and sets the flame speed to $s = \sqrt{s_\ell^2 + C_t q^2}$, where q is a velocity that characterizes the sub-grid turbulence energy content and C_t is a constant taken to be 4/3. This addition should boost the burning rate during the deflagration phase, which will change the density profile of the star when the detonation occurs and thus change the final yield. It may be our omission of turbulence and flame-turbulence interaction models that accounts for the systematic difference we see in the yield of IGEs compared to Seitenzahl et al. (2011). While the difference in treatment of the turbulent flame is a very important one, it is difficult to decouple from the dimensionality of the simulations performed. The dimensionality appears to influence the expansion rate, which may or may not be related to the turbulent flame model. Future three-dimensional simulations with different turbulent flame models will be able to address these uncertainties.

Seitenzahl et al. (2011) also mention the choice of ρ_{DDT} as a possible source of the difference between their study and our earlier results. As they describe, Seitenzahl et al. (2011) use a dynamic measure that calculates the probability of a DDT based on the turbulent intensity, density, and fraction of fuel. As they note, this prescription is significantly different from just fixing ρ_{DDT} and results in fewer DDTs. Considering Table 1 of Seitenzahl et al. (2011), we can see that the density at which the DDT occurred appears to be a function of central density due to their DDT criteria: other than their three models with only five DDT points, their effective DDT density increases with central density. A higher DDT density implies an earlier detonation, which means that the star has expanded less prior to the detonation, allowing the detonation to burn a larger fraction of the star. So it may be possible that the trend of increasing IGEs seen in Seitenzahl et al. (2011) comes from the change in their effective DDT density, instead of directly from the changing $\rho_{c,0}$. Regardless of whether this difference in methodology fully explains the difference in results, we can state that the differences in methodologies make direct comparison between the two results difficult.

Finally, the relatively small number of simulations performed by Seitenzahl et al. (2011) may not allow them to determine statistically meaningful trends. Unfortunately, the expense of three-dimensional simulations make extensive studies difficult. The twelve simulations they performed are a remarkable achievement, but our results suggest that it is necessary to have a distribution of ignition conditions that reproduces the distribution of observed yields. Our statistical ensemble does this in two dimensions, but demonstrating such a distribution in three dimensions would require significant computational resources.

As Seitenzahl et al. (2011) mention, Meakin et al. (2009)

explored the effect of varying the offset from the center of the initially burned region (what we call the "match head") in the GCD scenario. Their Figure 12 plots mass of NSE elements (which we have been referring to as IGEs), mass at $\rho > 10^7$ g cm^{-3}, and mass of ^{56}Ni as functions of central density *at the time of the detonation;* all of their models have the same central density at the ignition of the deflagration. We note that the GCD scenario is significantly different from the DDT scenario that we and Seitenzahl et al. (2011) investigated, with the principal difference arising in the expansion of the star during the deflagration phase of the evolution. In the GCD scenario, the star expands during the deflagration as the bubbles rise because the displaced mass softens the gravitational potential. The effect is that GCD models typically experience considerably less expansion than DDT models. Also, unlike central ignitions, there is very little material burned until the detonation occurs. A direct comparison, therefore, between the results of Meakin et al. (2009), with yields presented as functions of the central density at the ignition of the detonation, and our work, considering yields as a function of central density at the initial ignition of the deflagration, is at best uncertain, especially given that our results show that the effect of neutronization is greatest during the deflagration phase as illustrated in Figure 7.

Röpke et al. (2006) performed a set of simulations of SNeIa assuming the pure deflagration model. They found that as the central density of the progenitor is increased, the mass of ^{56}Ni produced also increases. Their discussion of why they produce more iron-group material also applies to our results. The yields during the deflagration and detonation phases were presented in Figure 7. We find the yield of IGEs increases with central density during the deflagration phase. We do not, however, find the same increase in ^{56}Ni mass due to increased neutronization. On this point our results disagree with the pure deflagration model as studied by Röpke et al. (2006). Bravo et al. (1990), however, studied the effects of neutronization and found that at higher central densities the yield of ^{56}Ni decreases, in agreement with our results.

Similarly to the Seitenzahl et al. (2011) work, Röpke et al. (2006) and Bravo et al. (1990) only performed a modest number of simulations. In light of our findings in Section 4.2, we note that it may be difficult to draw statistically significant results from a single realization. Röpke et al. (2006) and Bravo et al. (1990) both appear to use only a single morphology for each parameter set, which our results suggest could result in deriving an incorrect trend.

6. SUMMARY AND CONCLUSIONS

This paper builds on the results presented in Krueger et al. (2010), giving more detail of the study and extending the analysis. In that paper we showed that, in our 2-d simulations, a higher central density of the progenitor star does not impact the production of IGEs, but leads to greater neutronization, resulting in the production of less ^{56}Ni. We also discussed the relation between the age of the progenitor and the central density (see, e.g., Lesaffre et al. 2006), and the relation between the brightness and the mass of ^{56}Ni produced. Thus the statement that a higher density leads to less ^{56}Ni is equivalent to the statement that an older progenitor will produce a dimmer SNIa. In this work we expand on the discussion of Krueger et al. (2010) to give more detail of our models and to improve upon the age-brightness relation predicted by our simulations. In particular, we show that by adding a main-sequence lifetime to the cooling time our brightness-age relation is steeper, more closely matching the observed behavior of older SNeIa.

In comparing with other theoretical work, we see that the variation of ^{56}Ni mass with progenitor central density is not a settled question. In this paper we further developed the idea that, due to the strong nonlinearities of the processes in SNeIa, a statistical study of an ensemble of SNIa simulations may be necessary to determine the true trends. For our simulations, we find that 15 realizations (morphologies of the initial flame surface) are sufficient to characterize the mean trends from our models.

We find that the inner region (out to an enclosed mass of $0.8 - 1.0\ M_\odot$) of the remnant is dominated by ^{56}Ni. However, the stable (non-^{56}Ni) IGEs tend to be in "clumps", instead of well-mixed throughout this region. This may give rise to ^{56}Ni holes with little or no ^{56}Ni, depending on the line of sight through a SNIa remnant. The outer region of the remnant will have more intermediate- and low-mass elements, as the burning becomes less efficient for lower densities. As the central density increases, the mean ^{56}Ni mass fraction in the inner region drops (roughly 0.8 for $\rho_{c,0} = 1 \times 10^9$ g cm^{-3} to roughly 0.6 for $\rho_{c,0} = 5 \times 10^9$ g cm^{-3}). However, the extent of this region (in enclosed-mass space) does not significantly change. Variations in the central density affect the sharpness of the edges of the stable IGE clumps: a higher central density leads to clumps of stable elements that are more sharply defined, as well as less mixing between the ^{56}Ni and the stable IGEs.

To better connect to observations, we discussed how to distinguish the relative ages of SNeIa with the same brightness (in other words, the relative initial central densities of SNeIa that produce the same mass of ^{56}Ni). We found that, in our models, the best measure of the central density is the mass of stable IGEs, where higher central density progenitors produce more stable IGEs due to their greater rate of neutronization during the subsonic deflagration phase.

We found that a higher central density leads to a shorter deflagration phase. Since the rate of neutronization is significantly boosted, the total neutronization is greater at a higher central density despite there being less time to neutronize. The time between the ignition of the first detonation and the cessation of burning is independent of central density.

As noted in Krueger et al. (2010) and described above, our choice for the DDT transition density led to an overproduction of ^{56}Ni. In Section 5.1 we provided a recalibration of this overall brightness normalization to extrapolate our results to an expected average brightness. Future work will be improved by a better choice of DDT density and we will report any quantitative changes to the trends reported here. Due to the fundamentally 3-d nature of some of the phenomena in a SNIa (such as the turbulent velocities), we plan to extend this work by performing 3-d simulations. Because 3-d simulations are much more computationally expensive than the corresponding 2-d simulations, a study with 3-d simulations will by necessity be constrained to a smaller number of simulations. The choices will be motivated by this work and seek to span the parameter space explored here.

This work was supported by the Department of Energy through grants DE-FG02-07ER41516, DE-FG02-08ER41570, and DE-FG02-08ER41565, and by NASA through grant NNX09AD19G. ACC also acknowledges support from the Department of Energy under grant DE-FG02-87ER40317. APJ is currently supported by a National Research Council Research Associateship. The authors grate-

fully acknowledge the generous assistance of Pierre Lesaffre, fruitful discussions with Mike Zingale, and the use of weak reaction tables developed by Ivo Seitenzahl. The authors also acknowledge the hospitality of the KITP, which is supported by NSF grant PHY05-51164, during the programs "Accretion and Explosion: the Astrophysics of Degenerate Stars" and "Stellar Death and Supernovae." The software used in this work was in part developed by the DOE-supported ASC/Alliances Center for Astrophysical Thermonuclear Flashes at the University of Chicago. We thank Nathan Hearn for making his QuickFlash analysis tools publicly available at http://quickflash.sourceforge.net. This research utilized resources at the New York Center for Computational Sciences at Stony Brook University/Brookhaven National Laboratory which is supported by the U.S. Department of Energy under Contract No. DE-AC02-98CH10886 and by the State of New York.

REFERENCES

Albrecht, A., Bernstein, G., Cahn, R., Freedman, W. L., Hewitt, J., Hu, W., Huth, J., Kamionkowski, M., Kolb, E. W., Knox, L., Mather, J. C., Staggs, S., & Suntzeff, N. B. 2006, arXiv Astrophysics e-prints
Arnett, W. D. 1982, ApJ, 253, 785
Aspden, A. J., Bell, J. B., Day, M. S., Woosley, S. E., & Zingale, M. 2008, ApJ, 689, 1173
Aspden, A. J., Bell, J. B., & Woosley, S. E. 2010, ApJ, 710, 1654
Blinnikov, S. I. & Khokhlov, A. M. 1986, Soviet Astronomy Letters, 12, 131
Bloom, J. S., Kasen, D., Shen, K. J., Nugent, P. E., Butler, N. R., Graham, M. L., Howell, D. A., Kolb, U., Holmes, S., Haswell, C. A., Burwitz, V., Rodriguez, J., & Sullivan, M. 2012, ApJ, 744, L17
Branch, D., Livio, M., Yungelson, L. R., Boffi, F. R., & Baron, E. 1995, PASP, 107, 1019
Brandt, T. D., Tojeiro, R., Aubourg, É., Heavens, A., Jimenez, R., & Strauss, M. A. 2010, AJ, 140, 804
Bravo, E. & García-Senz, D. 2008, A&A, 478, 843
Bravo, E., Isern, J., Canal, R., & Labay, J. 1990, Ap&SS, 169, 19
Calder, A. C., Fryxell, B., Plewa, T., Rosner, R., Dursi, L. J., Weirs, V. G., Dupont, T., Robey, H. F., Kane, J. O., Remington, B. A., Drake, R. P., Dimonte, G., Zingale, M., Timmes, F. X., Olson, K., Ricker, P., MacNeice, P., & Tufo, H. M. 2002, ApJS, 143, 201
Calder, A. C., Townsley, D. M., Seitenzahl, I. R., Peng, F., Messer, O. E. B., Vladimirova, N., Brown, E. F., Truran, J. W., & Lamb, D. Q. 2007, ApJ, 656, 313
Chamulak, D. A., Brown, E. F., Timmes, F. X., & Dupczak, K. 2008, ApJ, 677, 160
Colgate, S. A. & McKee, C. 1969, ApJ, 157, 623
Conley, A., Guy, J., Sullivan, M., Regnault, N., Astier, P., Balland, C., Basa, S., Carlberg, R. G., Fouchez, D., Hardin, D., Hook, I. M., Howell, D. A., Pain, R., Palanque-Delabrouille, N., Perrett, K. M., Pritchet, C. J., Rich, J., Ruhlmann-Kleider, V., Balam, D., Baumont, S., Ellis, R. S., Fabbro, S., Fakhouri, H. K., Fourmanoit, N., González-Gaitán, S., Graham, M. L., Hudson, M. J., Hsiao, E., Kronborg, T., Lidman, C., Mourao, A. M., Neill, J. D., Perlmutter, S., Ripoche, P., Suzuki, N., & Walker, E. S. 2011, ApJS, 192, 1
Davidson, P. A. 2004, Turbulence (Oxford: Oxford University Press)
Domínguez, I., Höflich, P., & Straniero, O. 2001, ApJ, 557, 279
Filippenko, A. V. 1997, ARA&A, 35, 309
Fisher, R., Falta, D., Jordan, G., & Lamb, D. 2010, in Gravitation and Astrophysics, ed. J. Luo, Z.-B. Zhou, H.-C. Yeh, & J.-P. Hsu, 335–344
Fryxell, B., Olson, K., Ricker, P., Timmes, F. X., Zingale, M., Lamb, D. Q., MacNeice, P., Rosner, R., Truran, J. W., & Tufo, H. 2000, ApJS, 131, 273
Fuller, G. M., Fowler, W. A., & Newman, M. J. 1985, ApJ, 293, 1
Gallagher, J. S., Garnavich, P. M., Caldwell, N., Kirshner, R. P., Jha, S. W., Li, W., Ganeshalingam, M., & Filippenko, A. V. 2008, ApJ, 685, 752
Golombek, I. & Niemeyer, J. C. 2005, A&A, 438, 611
Hansen, C. J., Kawaler, S. D., & Trimble, V. 2004, Stellar interiors : physical principles, structure, and evolution, ed. Hansen, C. J., Kawaler, S. D., & Trimble, V.
Hillebrandt, W. & Niemeyer, J. C. 2000, ARA&A, 38, 191
Hoeflich, P., Wheeler, J. C., & Thielemann, F. K. 1998, ApJ, 495, 617
Höflich, P. & Khokhlov, A. 1996, ApJ, 457, 500
Hoflich, P., Khokhlov, A. M., & Wheeler, J. C. 1995, ApJ, 444, 831
Höflich, P., Krisciunas, K., Khokhlov, A. M., Baron, E., Folatelli, G., Hamuy, M., Phillips, M. M., Suntzeff, N., Wang, L., & NSF07-SNIa Collaboration. 2010, ApJ, 710, 444
Howell, D. A., Sullivan, M., Brown, E. F., Conley, A., Le Borgne, D., Hsiao, E. Y., Astier, P., Balam, D., Balland, C., Basa, S., Carlberg, R. G., Fouchez, D., Guy, J., Hardin, D., Hook, I. M., Pain, R., Perrett, K., Pritchet, C. J., Regnault, N., Baumont, S., LeDu, J., Lidman, C., Perlmutter, S., Suzuki, N., Walker, E. S., & Wheeler, J. C. 2009, ApJ, 691, 661
Jackson, A. P., Calder, A. C., Townsley, D. M., Chamulak, D. A., Brown, E. F., & Timmes, F. X. 2010, ApJ, 720, 99
Jacoby, G. H., Branch, D., Ciardullo, R., Davies, R. L., Harris, W. E., Pierce, M. J., Pritchet, C. J., Tonry, J. L., & Welch, D. L. 1992, PASP, 104, 599
Jha, S., Riess, A. G., & Kirshner, R. P. 2007, ApJ, 659, 122
Khokhlov, A. M. 1989, MNRAS, 239, 785
—. 1991, A&A, 245, 114
—. 1995, ApJ, 449, 695
—. 2000, ApJ, submitted, astro-ph/0008463
Khokhlov, A. M., Oran, E. S., & Wheeler, J. C. 1997, ApJ, 478, 678
Kirshner, R. P. 2010, Foundations of supernova cosmology, ed. Ruiz-Lapuente, P., 151
Krueger, B. K., Jackson, A. P., Townsley, D. M., Calder, A. C., Brown, E. F., & Timmes, F. X. 2010, ApJ, 719, L5
Langanke, K. & Martínez-Pinedo, G. 2001, At. Data Nucl. Data Tables, 79, 1
Lesaffre, P., Han, Z., Tout, C. A., Podsiadlowski, P., & Martin, R. G. 2006, MNRAS, 368, 187
Li, W., Bloom, J. S., Podsiadlowski, P., Miller, A. A., Cenko, S. B., Jha, S. W., Sullivan, M., Howell, D. A., Nugent, P. E., Butler, N. R., Ofek, E. O., Kasliwal, M. M., Richards, J. W., Stockton, A., Shih, H.-Y., Bildsten, L., Shara, M. M., Bibby, J., Filippenko, A. V., Ganeshalingam, M., Silverman, J. M., Kulkarni, S. R., Law, N. M., Poznanski, D., Quimby, R. M., McCully, C., Patel, B., Maguire, K., & Shen, K. J. 2011, Nature, 480, 348
Lisewski, A. M., Hillebrandt, W., & Woosley, S. E. 2000, ApJ, 538, 831
Livio, M. 2000, in Type Ia Supernovae, Theory and Cosmology, ed. J. C. Niemeyer & J. W. Truran (Cambridge: Cambridge Univ. Press), 33
Maeda, K., Röpke, F. K., Fink, M., Hillebrandt, W., Travaglio, C., & Thielemann, F.-K. 2010, ApJ, 712, 624
Mannucci, F., Della Valle, M., & Panagia, N. 2006, MNRAS, 370, 773
Mazzali, P. A. & Podsiadlowski, P. 2006, MNRAS, 369, L19
Meakin, C. A., Seitenzahl, I., Townsley, D., Jordan, G. C., Truran, J., & Lamb, D. 2009, ApJ, 693, 1188
Minkowski, R. 1941, PASP, 53, 224
Neill, J. D., Sullivan, M., Howell, D. A., Conley, A., Seibert, M., Martin, D. C., Barlow, T. A., Foster, K., Friedman, P. G., Morrissey, P., Neff, S. G., Schiminovich, D., Wyder, T. K., Bianchi, L., Donas, J., Heckman, T. M., Lee, Y., Madore, B. F., Milliard, B., Rich, R. M., & Szalay, A. S. 2009, ApJ, 707, 1449
Niemeyer, J. C. 1999, ApJ, 523, L57
Niemeyer, J. C. & Hillebrandt, W. 1995, ApJ, 452, 769
Niemeyer, J. C. & Woosley, S. E. 1997, ApJ, 475, 740
Nomoto, K., Saio, H., Kato, M., & Hachisu, I. 2007, ApJ, 663, 1269
Nomoto, K., Thielemann, F.-K., & Yokoi, K. 1984, ApJ, 286, 644
Nugent, P. E., Sullivan, M., Cenko, S. B., Thomas, R. C., Kasen, D., Howell, D. A., Bersier, D., Bloom, J. S., Kulkarni, S. R., Kandrashoff, M. T., Filippenko, A. V., Silverman, J. M., Marcy, G. W., Howard, A. W., Isaacson, H. T., Maguire, K., Suzuki, N., Tarlton, J. E., Pan, Y.-C., Bildsten, L., Fulton, B. J., Parrent, J. T., Sand, D., Podsiadlowski, P., Bianco, F. B., Dilday, B., Graham, M. L., Lyman, J., James, P., Kasliwal, M. M., Law, N. M., Quimby, R. M., Hook, I. M., Walker, E. S., Mazzali, P., Pian, E., Ofek, E. O., Gal-Yam, A., & Poznanski, D. 2011, Nature, 480, 344
Oda, T., Hino, M., Muto, K., Takahara, M., & Sato, K. 1994, A. Data Nucl. Data Tables, 56, 231
Perlmutter, S., Aldering, G., Goldhaber, G., Knop, R. A., Nugent, P., Castro, P. G., Deustua, S., Fabbro, S., Goobar, A., Groom, D. E., Hook, I. M., Kim, A. G., Kim, M. Y., Lee, J. C., Nunes, N. J., Pain, R., Pennypacker, C. R., Quimby, R., Lidman, C., Ellis, R. S., Irwin, M., McMahon, R. G., Ruiz-Lapuente, P., Walton, N., Schaefer, B., Boyle, B. J., Filippenko, A. V., Matheson, T., Fruchter, A. S., Panagia, N., Newberg, H. J. M., Couch, W. J., & The Supernova Cosmology Project. 1999, ApJ, 517, 565
Phillips, M. M. 1993, ApJ, 413, L105
Pinto, P. A. & Eastman, R. G. 2000, ApJ, 530, 744
Piro, A. L. & Bildsten, L. 2008, ApJ, 673, 1009
Piro, A. L. & Chang, P. 2008, ApJ, 678, 1158
Plewa, T., Calder, A. C., & Lamb, D. Q. 2004, ApJ, 612, L37

Poludnenko, A. Y., Gardiner, T. A., & Oran, E. S. 2011, Physical Review Letters, 107, 054501
Poludnenko, A. Y. & Oran, E. S. 2011a, Combustion and Flame, 157, 995
—. 2011b, Combustion and Flame, 158, 301
Pope, S. B. 1987, Annual Review of Fluid Mechanics, 19, 237
Riess, A. G., Filippenko, A. V., Challis, P., Clocchiatti, A., Diercks, A., Garnavich, P. M., Gilliland, R. L., Hogan, C. J., Jha, S., Kirshner, R. P., Leibundgut, B., Phillips, M. M., Reiss, D., Schmidt, B. P., Schommer, R. A., Smith, R. C., Spyromilio, J., Stubbs, C., Suntzeff, N. B., & Tonry, J. 1998, AJ, 116, 1009
Riess, A. G., Macri, L., Casertano, S., Lampeitl, H., Ferguson, H. C., Filippenko, A. V., Jha, S. W., Li, W., & Chornock, R. 2011, ApJ, 730, 119
Röpke, F. K. 2006, in Reviews in Modern Astronomy, ed. S. Roeser, Vol. 19 (Wenheim: Wiley-VCH), 127
Röpke, F. K. 2007, ApJ, 668, 1103
Röpke, F. K., Gieseler, M., Reinecke, M., Travaglio, C., & Hillebrandt, W. 2006, A&A, 453, 203
Röpke, F. K. & Hillebrandt, W. 2005, A&A, 429, L29
Röpke, F. K. & Niemeyer, J. C. 2007, A&A, 464, 683
Röpke, F. K., Seitenzahl, I. R., Benitez, S., Fink, M., Pakmor, R., Kromer, M., Sim, S. A., Ciaraldi-Schoolmann, F., & Hillebrandt, W. 2011, Progress in Particle and Nuclear Physics, 66, 309
Scalzo, R. A., Aldering, G., Antilogus, P., Aragon, C., Bailey, S., Baltay, C., Bongard, S., Buton, C., Childress, M., Chotard, N., Copin, Y., Fakhouri, H. K., Gal-Yam, A., Gangler, E., Hoyer, S., Kasliwal, M., Loken, S., Nugent, P., Pain, R., Pécontal, E., Pereira, R., Perlmutter, S., Rabinowitz, D., Rau, A., Rigaudier, G., Runge, K., Smadja, G., Tao, C., Thomas, R. C., Weaver, B., & Wu, C. 2010, ApJ, 713, 1073
Scannapieco, E. & Bildsten, L. 2005, ApJ, 629, L85
Schmidt, W., Ciaraldi-Schoolmann, F., Niemeyer, J. C., Röpke, F. K., & Hillebrandt, W. 2010, ApJ, 710, 1683
Schmidt, W., Niemeyer, J. C., & Hillebrandt, W. 2006a, A&A, 450, 265
Schmidt, W., Niemeyer, J. C., Hillebrandt, W., & Röpke, F. K. 2006b, A&A, 450, 283
Seitenzahl, I. R., Ciaraldi-Schoolmann, F., & Röpke, F. K. 2011, MNRAS, 414, 2709
Seitenzahl, I. R., Meakin, C. A., Townsley, D. M., Lamb, D. Q., & Truran, J. W. 2009a, ApJ, 696, 515
Seitenzahl, I. R., Townsley, D. M., Peng, F., & Truran, J. W. 2009b, A. Data Nucl. Data Tables, 95, 96
Straniero, O., Domínguez, I., Imbriani, G., & Piersanti, L. 2003, ApJ, 583, 878
Sullivan, M., Guy, J., Conley, A., Regnault, N., Astier, P., Balland, C., Basa, S., Carlberg, R. G., Fouchez, D., Hardin, D., Hook, I. M., Howell, D. A., Pain, R., Palanque-Delabrouille, N., Perrett, K. M., Pritchet, C. J., Rich, J., Ruhlmann-Kleider, V., Balam, D., Baumont, S., Ellis, R. S., Fabbro, S., Fakhouri, H. K., Fourmanoit, N., González-Gaitán, S., Graham, M. L., Hudson, M. J., Hsiao, E., Kronborg, T., Lidman, C., Mourao, A. M., Neill, J. D., Perlmutter, S., Ripoche, P., Suzuki, N., & Walker, E. S. 2011, ApJ, 737, 102
Timmes, F. X. & Swesty, F. D. 2000, ApJS, 126, 501
Townsley, D. M., Calder, A. C., Asida, S. M., Seitenzahl, I. R., Peng, F., Vladimirova, N., Lamb, D. Q., & Truran, J. W. 2007, ApJ, 668, 1118
Townsley, D. M., Jackson, A. P., Calder, A. C., Chamulak, D. A., Brown, E. F., & Timmes, F. X. 2009, ApJ, 701, 1582
Truran, J. W., Arnett, W. D., & Cameron, A. G. W. 1967, Can. J. Phys., 45, 2315
Vladimirova, N., Weirs, G., & Ryzhik, L. 2006, Combust. Theory Modelling, 10, 727
Woosley, S. E. 1990, in Supernovae, ed. A. G. Petschek, 182–212
Woosley, S. E. 2007, ApJ, 668, 1109
Woosley, S. E., Kasen, D., Blinnikov, S., & Sorokina, E. 2007, ApJ, 662, 487
Woosley, S. E., Kerstein, A. R., Sankaran, V., Aspden, A. J., & Röpke, F. K. 2009, ApJ, 704, 255
Yuan, F., Quimby, R. M., Wheeler, J. C., Vinkó, J., Chatzopoulos, E., Akerlof, C. W., Kulkarni, S., Miller, J. M., McKay, T. A., & Aharonian, F. 2010, ApJ, 715, 1338

APPENDIX

A. RANDOMIZED INITIAL CONDITIONS

The initial flame surfaces for each realization are determined by spherical harmonics. The formula used is:

$$r = 150\text{km} + \sum_{\ell} A_\ell Y_\ell^m, \tag{A1}$$

where Y_ℓ^m are the spherical harmonics and the coefficients A_ℓ are given in Table A1. A reference implementation is available online at http://astronomy.ua.edu/townsley/code/. This suite of simulations used an initial seed value of 1866936915.

B. RECALIBRATION OF ^{56}Ni YIELDS

As discussed above near the beginning of Section 4, on average our suite of simulations exhibited an overproduction of IGEs and ^{56}Ni. The yields of IGEs and ^{56}Ni are related to the expansion of the WD prior to the ignition of the detonation: as the star expands during the deflagration phase, the density decreases and, therefore, less fuel (C and O) remains at sufficiently high density to burn to IGEs during the detonation. Thus, the amount of expansion of the WD prior to the DDT principally determines the yield of IGEs and ^{56}Ni (Nomoto et al. 1984; Khokhlov 1991). The amount of expansion is determined by DDT conditions (Jackson et al. 2010) along with the energy deposition history, which depends on initial conditions, dimensionality, and the burning model.

Given our models and the simulations we have performed, the most straightforward way to systematically correct the overproduction of IGEs is to modify the DDT conditions and repeat the simulations. The value of $\rho_{\rm DDT}$ should be determined by the physics of the DDT, but, as the physics of DDTs is incompletely understood and most likely could not be resolved in these simulations, we treat $\rho_{\rm DDT}$ as a parameter. The DDT transition is implemented by burning small regions ahead of rising plumes, when the tip of the plume reaches $\rho_{\rm DDT}$. As demonstrated in Jackson et al. (2010), lowering the value of $\rho_{\rm DDT}$ is tantamount to increasing $t_{\rm DDT}$ because the material that undergoes a DDT is at a higher radius and the time required for a rising bubble of burning material to reach that radius is longer. This longer $t_{\rm DDT}$ results in more expansion of the WD prior to detonation and, because the amount of material at higher density decreases, the detonation produces a lower yield of IGEs. In order to address the impact of $\rho_{\rm DDT}$ on our results, the ideal solution would be to repeat our simulations with $\rho_{\rm DDT}$ set to a lower value and therefore obtain a longer $t_{\rm DDT}$, more expansion, and more realistic yields. Using the data available from this study and the study of Jackson et al. (2010), we can estimate the results of performing a new suite of simulations using a different value of $\rho_{\rm DDT}$ and use these findings to inform future studies. We consider two issues here. First we attempt to extrapolate to lower $\rho_{\rm DDT}$ based on the expansion characteristics of our models to confirm that for a *single value* of $\rho_{\rm DDT}$, the $M_{\rm IGE}$ appears to continue to be independent of $\rho_{c,0}$. Second, we use this justified assumption to extrapolate our yields based on a delay of the DDT transition.

First we consider how we expect $M_{\rm IGE}$ might change if a lower $\rho_{\rm DDT}$ were assumed. Townsley et al. (2009) demonstrates a correlation between $M_{\rm IGE}$ at $t_{\rm IGE}$ and the mass of all material with a density greater than 2×10^7 g cm^{-3} at time $t_{\rm DDT}$ (which we represent by $M^{\rm DDT}_{\rho_7>2}$). Therefore we can choose a new value of $\rho_{\rm DDT}$ and use this correlation to estimate the final mass of IGEs in

TABLE A1: Amplitudes of spherical harmonic perturbations by realization.

real. #	amplitude of perturbation (km)				
	A_{12}	A_{13}	A_{14}	A_{15}	A_{16}
1	-50.88	-51.22	22.23	9.979	-56.23
2	-31.03	51.57	-43.21	-55.76	-30.22
3	-39.89	-28.06	31.48	6.848	-29.80
4	-48.89	-44.21	1.509	52.44	29.00
5	29.67	-74.12	-53.44	13.83	-51.24
6	-26.95	5.169	-45.79	-46.34	14.93
7	12.67	-19.76	-90.22	-2.312	-20.83
8	-10.23	1.206	-43.74	-25.57	10.26
9	30.25	69.91	-29.37	-74.17	-29.50
10	-15.76	-4.818	14.53	1.979	-15.23
11	-55.91	47.08	-15.86	-34.44	-43.00
12	1.021	-0.685	-33.13	-48.32	-22.22
13	-10.41	-32.27	5.236	27.06	-12.46
14	-73.60	-38.16	-22.76	41.81	25.76
15	-74.20	-3.179	-30.20	-36.56	-21.16
16	-86.84	16.28	19.75	14.43	4.924
17	12.87	44.39	-12.17	-34.34	-67.18
18	-13.88	-62.62	-35.93	-41.57	-81.32
19	-31.09	-49.91	2.953	57.76	-5.397
20	51.43	-44.30	-41.00	26.83	-42.83
21	-28.15	11.27	-37.43	85.20	-46.84
22	53.67	4.730	-52.71	-46.66	-65.99
23	-21.66	-12.31	53.21	14.14	-34.18
24	-16.25	-68.30	-43.63	111.6	-33.86
25	-56.50	-31.25	44.51	0.098	-40.66
26	-98.62	-31.80	-19.40	45.75	-3.815
27	-39.29	2.525	-32.95	27.10	-14.95
28	29.24	79.73	-30.80	-19.18	-96.98
29	-14.08	46.98	-89.82	-11.95	28.21
30	-24.91	33.12	-46.75	-10.40	-3.940

order to verify that changing $\rho_{\rm DDT}$ does not change the fact that the mass of IGEs is independent of $\rho_{c,0}$. In order to refine the relation between $M_{\rm IGE}$ and $M^{\rm DDT}_{\rho_7>2}$, we make use of data from this study and data from the study presented in Jackson et al. (2010), which varied $\rho_{\rm DDT}$. This will enable us to calibrate the relationship between $M_{\rm IGE}$ and $M^{\rm DDT}_{\rho_7>2}$ for differences in $\rho_{c,0}$ and $\rho_{\rm DDT}$. The relationship between $M_{\rm IGE}$ and $M^{\rm DDT}_{\rho_7>2}$ appears to be approximately linear, so we assume that $M_{\rm IGE} = m\,M^{\rm DDT}_{\rho_7>2} + b$. As can be seen in Figure B1, the relationship between $M^{\rm DDT}_{\rho_7>2}$ and $M_{\rm IGE}$ depends on $\rho_{c,0}$ and $\rho_{\rm DDT}$, so the slope and intercept are allowed to be functions of $\rho_{c,0}$ and $\rho_{\rm DDT}$. We test polynomials of varying degree and find that the best functions are quadratic in $\rho_{c,0}$ and $\rho_{\rm DDT}$ for both the slope and the intercept. The equations for this fitting are

$$M_{\rm IGE} = m(\rho_{c,0},\rho_{\rm DDT})\,M^{\rm DDT}_{\rho_7>2} + b(\rho_{c,0},\rho_{\rm DDT}) \tag{B1a}$$

$$m(\rho_{c,0},\rho_{\rm DDT}) = m_0 + \gamma_1\rho_{c,0} + \gamma_2\rho^2_{c,0} + \delta_1\rho_{\rm DDT} + \delta_2\rho^2_{\rm DDT} \tag{B1b}$$

$$b(\rho_{c,0},\rho_{\rm DDT}) = b_0 + \varepsilon_1\rho_{c,0} + \varepsilon_2\rho^2_{c,0} + \zeta_1\rho_{\rm DDT} + \zeta_2\rho^2_{\rm DDT}. \tag{B1c}$$

Fitting this 10-parameter function to the data from this study and the study of Jackson et al. (2010) yields the parameters given in Table B1. As a check, we use this relation at the same $\rho_{\rm DDT}$ as was used in our simulations ($10^{7.1}$ g cm^{-3}) and compare the estimated values of $M_{\rm IGE}$ to the actual values. This is shown in Figure B2.

With this function, we can extract $M^{\rm DDT}_{\rho_7>2}$ assuming different values of $\rho_{\rm DDT}$. Based on the data available, we cannot choose a value of $\rho_{\rm DDT}$ lower than what used in this study, but we can test higher values of $\rho_{\rm DDT}$. Figure B3 shows that for three sample values of $\rho_{\rm DDT}$, $M_{\rm IGE}$ is still independent of $\rho_{c,0}$; formally, we say that $M_{\rm IGE}$ is independent of $\rho_{c,0}$ when the magnitude of the slope of the line relating these two quantities is less than the uncertainty in the slope. We therefore assume that, even for lower values of $\rho_{\rm DDT}$, $M_{\rm IGE}$ is independent of $\rho_{c,0}$. This allows us to apply a uniform shift in $M_{\rm IGE}$ (constant for all simulations) to correct for the overproduction of IGEs. Observations tell us that the mass of IGEs should lie approximately in the range of $0.7-0.9$ M$_\odot$ (see, e.g., Woosley et al. 2007), so we can choose to force our mean mass of IGEs to be in the center of this range (0.8 M$_\odot$).

Now that we have established a reasonable expectation that $M_{\rm IGE}$ will continue to be independent of $\rho_{c,0}$ even at other $\rho_{\rm DDT}$ values, we proceed to extrapolate our yields based around this premise. We can relate this change in $M_{\rm IGE}$ to a change in the mass of ^{56}Ni through adjustments to $t_{\rm DDT}$. The value of $t_{\rm DDT}$, which depends on $\rho_{\rm DDT}$, is not a free parameter that can be independently adjusted in our models; however, in order to correct the mass of ^{56}Ni we can treat $t_{\rm DDT}$ as a parameter. Figure B4 shows the masses of IGEs and ^{56}Ni plotted as functions of $t_{\rm DDT}$, where each point is a single simulation colored by $\rho_{c,0}$. Also shown is a trend line based on Equation (B2), explained below. Each of these quantities shows five separate trends, one for each value of $\rho_{c,0}$. Performing independent linear fits for each $\rho_{c,0}$ gives lines that appear to be correlated: the five lines intersect each other near $t_{\rm DDT} = 0$, and the slopes appear to be a function of $\rho_{c,0}$. Based on these correlations, we derived a new fit using the function

$$y(\rho_{c,0},t_{\rm DDT}) = y_0 + s(\rho_{c,0})\,t_{\rm DDT}, \tag{B2}$$

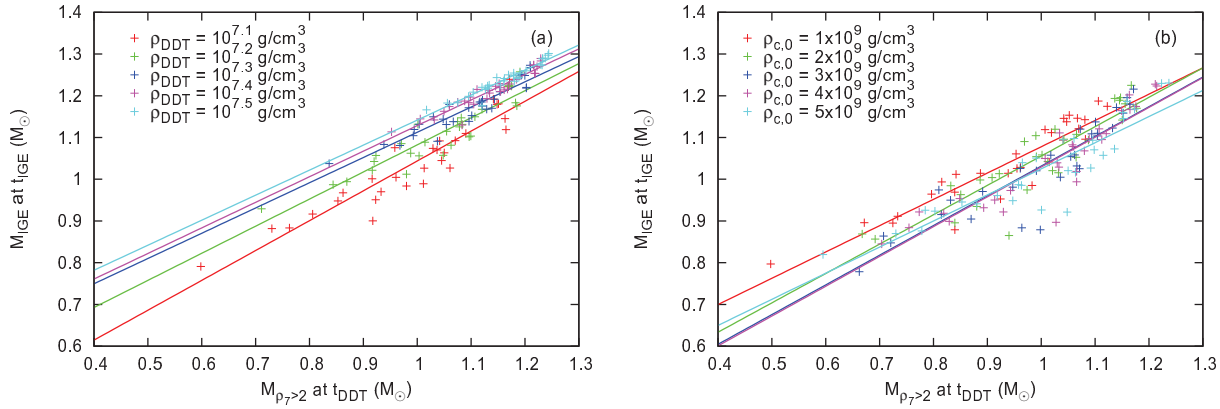

FIG. B1.—: Relationship between $M^{\rm DDT}_{\rho_7>2}$ and $M_{\rm IGE}$, demonstrating the dependence of this relationship on $\rho_{c,0}$ and $\rho_{\rm DDT}$. The data in the left panel comes from the study of Jackson et al. (2010), which varied $\rho_{\rm DDT}$ with a constant $\rho_{c,0}$; data points and trend lines are colored by $\rho_{\rm DDT}$. The data in the right panel comes from this study; data points and trend lines are colored by $\rho_{c,0}$.

TABLE B1: Fit parameters for Equation (B1). These values assume that $\rho_{c,0}$ is in 10^9 g cm^{-3}, $\rho_{\rm DDT}$ is in 10^7 g cm^{-3}, and both masses are in $M_\odot$.

parameter	value
m_0	9.099×10^{-1}
γ_1	1.453×10^{-1}
γ_2	-2.429×10^{-2}
δ_1	-4.225×10^{-1}
δ_2	8.555×10^{-2}
b_0	8.358×10^{-3}
ε_1	-1.847×10^{-1}
ε_2	2.869×10^{-2}
ζ_1	6.231×10^{-1}
ζ_2	-1.196×10^{-1}

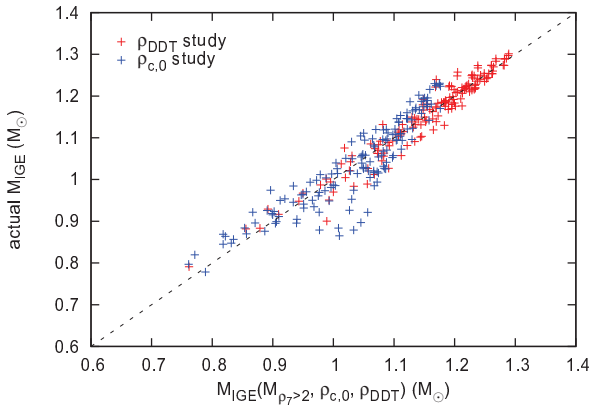

FIG. B2.—: Demonstration of the results of Equation (B1), showing the comparison of the actual $M_{\rm IGE}$ data from simulations to the values of $M_{\rm IGE}$ estimated from this relation (assuming $\rho_{\rm DDT} = 10^{7.1}$ g cm^{-3}). Data points are colored by the study they were taken from: blue from this study, red from Jackson et al. (2010). The dotted line shows a perfect correspondence between the two measures of $M_{\rm IGE}$.

where y is the mass of either IGEs or ^{56}Ni. We found that the best form for the slope $s(\rho_{c,0})$ is:

$$s(\rho_{c,0}) = a\,\rho_{c,0}^2 + b\,\rho_{c,0} + c. \tag{B3}$$

Minimizing the χ^2_ν for this 4-parameter function results in the parameter values shown in Table B2.

Given the shift in the mass of IGEs, we can then use the $M_{\rm IGE}(\rho_{c,0}, t_{\rm DDT})$ relation from Equations (B2) and (B3) to compute a corresponding change in $t_{\rm DDT}$. However, since the relation (in particular the slope) depends on $\rho_{c,0}$, the time shift will also depend

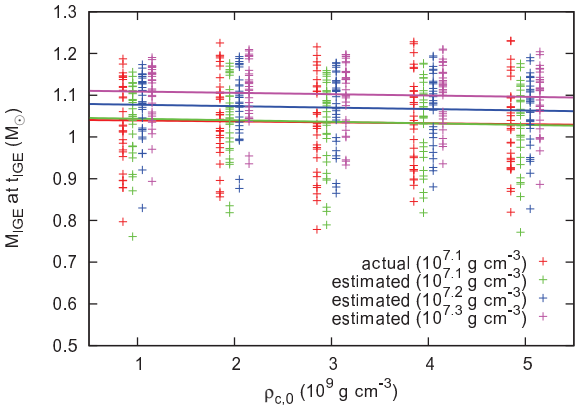

FIG. B3.—: Demonstration of the results of Equation (B1), showing the trend of $M_{\rm IGE}$ with $\rho_{c,0}$, using data from this study. The values of $M_{\rm IGE}$ from the simulations are shown in red, with green, blue, and magenta showing the estimated $M_{\rm IGE}$ assuming $\rho_{\rm DDT} = 10^{7.1}$, $10^{7.2}$, and $10^{7.3}$ g cm^{-3} respectively. The data points are slightly offset horizontally for clarity. This shows that $M_{\rm IGE}$ is independent of $\rho_{c,0}$ even if $\rho_{\rm DDT}$ varies. This figure also demonstrates that a lower value of $\rho_{\rm DDT}$ leads to a lower mean value of $M_{\rm IGE}$.

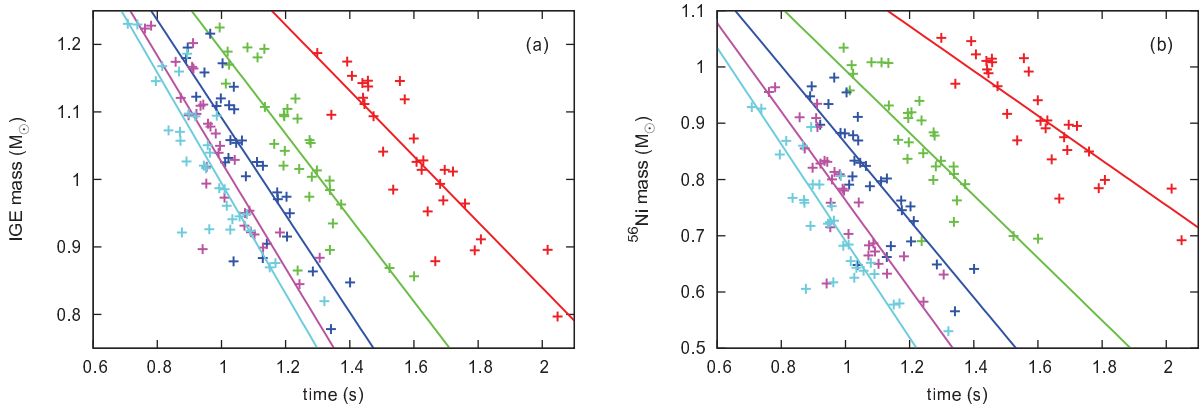

FIG. B4.—: Yield of IGEs (left panel) and ^{56}Ni (right panel) as functions of $t_{\rm DDT}$ for the 149 simulations. Also shown are the best-fit trend lines in the form given by Equations (B2) and (B3). Lines and data points are colored by $\rho_{c,0}$: 1.0×10^9 g cm^{-3} (red), 2.0×10^9 g cm^{-3} (green), 3.0×10^9 g cm^{-3} (blue), 4.0×10^9 g cm^{-3} (magenta), 5.0×10^9 g cm^{-3} (cyan).

TABLE B2: Fit parameters for Equations (B2) and (B3). These values assume that $t_{\rm DDT}$ is in seconds, $\rho_{c,0}$ is in 10^9 g cm^{-3}, and mass is in M$_\odot$.

parameter	$M_{\rm IGE}$	$M_{^{56}{\rm Ni}}$
y_0	1.813	1.550
a	1.716×10^{-2}	1.422×10^{-2}
b	-1.859×10^{-1}	-2.007×10^{-1}
c	-3.180×10^{-1}	-2.114×10^{-1}

on $\rho_{c,0}$; i.e., we will have $\Delta t_{\rm DDT}(\rho_{c,0})$. The five values of $\Delta t_{\rm DDT}$ are given in Table B3. Using this density-dependent time shift and the $M_{^{56}{\rm Ni}}(\rho_{c,0}, t_{\rm DDT})$ relation, we can then derive a consistent adjustment to the mass of ^{56}Ni. This adjusted mass of ^{56}Ni is used in Section 5.1.

C. SIMULATION RESULTS

The structure and composition of the progenitor models are discussed in detail in Section 2.1, along with the creation of a statistical ensemble. The simulations and the code are discussed in Section 2. As we have stressed, the principal result from our simulations is a mass of ^{56}Ni. Our models reproduce the qualitative description given in Woosley et al. (2007) that produces a type Ia supernova light curve. The ideal solution for comparing our results to observed light would be for us to post-process our results with a radiation transfer method to actually calculate light curves. In the absence of that technology, we may infer observed properties of supernova events suggested by our results. We report some of those here, including stretch, the scaling of

TABLE B3: Time shifts for the recalibration of the ^{56}Ni and IGE masses.

$\rho_{c,0}$ (g cm^{-3})	$\Delta t_{\rm DDT}$ (s)
1×10^9	0.4850
2×10^9	0.3800
3×10^9	0.3273
4×10^9	0.2999
5×10^9	0.2884

brightness with rapidity of decline that is reported in observational results (Howell et al. 2009; Jha et al. 2007). The tabulated data are

1. $\rho_{c,0}$: central density of pre-supernova white dwarf (g cm^{-3});
2. r: realization number[10];
3. $t_{\rm DDT}$: time of the first deflagration-to-detonation transition (s);
4. $M_{\rm IGE}(t_{\rm DDT})$: mass of Fe-group elements synthesized by time $t_{\rm DDT}$ ($M_\odot$);
5. $M_{^{56}{\rm Ni}}(t_{\rm DDT})$: mass of ^{56}Ni synthesized by time $t_{\rm DDT}$ ($M_\odot$);
6. $t_{\rm IGE}$: time that production of Fe-group elements ceases (s);
7. $M_{\rm IGE}(t_{\rm IGE})$: mass of Fe-group elements synthesized by time $t_{\rm IGE}$ ($M_\odot$);
8. $M_{^{56}{\rm Ni}}(t_{\rm IGE})$: mass of ^{56}Ni synthesized by time $t_{\rm IGE}$ ($M_\odot$);
9. $t^*_{\rm DDT}$: recalibrated[11] value of $t_{\rm DDT}$ (s);
10. $M^*_{\rm IGE}(t^*_{\rm IGE})$: recalibrated[11] value of $M_{\rm IGE}(t_{\rm IGE})$ ($M_\odot$);
11. $M^*_{^{56}{\rm Ni}}(t^*_{\rm IGE})$: recalibrated[11] value of $M_{^{56}{\rm Ni}}(t_{\rm IGE})$ ($M_\odot$);
12. s: recalibrated[11] value of stretch[12];
13. $\tau_{\rm cool}$: cooling time[12] (yr).

The initial composition for the progenitor is shown in Table 2. The total mass of the star and the total mass of the initial convective, isentropic core are both shown for each progenitor in Table 1. Both of these tables are shown in Section 2.1.

TABLE C1: Data extracted from simulations.

$\rho_{c,0}$ (g cm^{-3})	r	$t_{\rm DDT}$ (s)	$M_{\rm IGE}(t_{\rm DDT})$ ($M_\odot$)	$M_{^{56}{\rm Ni}}(t_{\rm DDT})$ ($M_\odot$)	$t_{\rm IGE}$ (s)	$M_{\rm IGE}(t_{\rm IGE})$ ($M_\odot$)	$M_{^{56}{\rm Ni}}(t_{\rm IGE})$ ($M_\odot$)	$t^*_{\rm DDT}$ (s)	$M^*_{\rm IGE}(t^*_{\rm IGE})$ ($M_\odot$)	$M^*_{^{56}{\rm Ni}}(t^*_{\rm IGE})$ ($M_\odot$)	s	$\tau_{\rm cool}$ (yr)
1e+9	1	1.439	1.256e-1	7.744e-2	2.046	1.143e+0	1.011e+0	1.924	9.067e-1	8.177e-1	1.203	...[b]
1e+9	2	1.608	1.756e-1	1.210e-1	2.040	1.026e+0	9.042e-1	2.093	7.900e-1	7.112e-1	1.138	...[b]
1e+9	3	1.809	1.773e-1	1.229e-1	2.203	9.113e-1	7.991e-1	2.294	6.752e-1	6.061e-1	1.066	...[b]
1e+9	4	1.696	1.766e-1	1.256e-1	2.083	1.014e+0	8.972e-1	2.181	7.783e-1	7.042e-1	1.134	...[b]
1e+9	5	1.504	1.490e-1	9.677e-2	2.039	1.041e+0	9.166e-1	1.989	8.052e-1	7.237e-1	1.146	...[b]
1e+9	6	1.456	1.176e-1	7.158e-2	1.959	1.146e+0	1.015e+0	1.941	9.102e-1	8.217e-1	1.205	...[b]
1e+9	7	1.474	1.313e-1	8.181e-2	2.008	1.094e+0	9.659e-1	1.959	8.575e-1	7.729e-1	1.177	...[b]
1e+9	8	1.477	1.164e-1	6.855e-2	2.400	8.780e-1	7.687e-1	...[a]	...[a]	...[a]	...[a]	...[a]
1e+9	9	1.682	1.637e-1	1.110e-1	2.095	9.935e-1	8.751e-1	2.167	7.575e-1	6.822e-1	1.119	...[b]
1e+9	10	2.017	2.081e-1	1.495e-1	2.430	8.959e-1	7.837e-1	2.502	6.599e-1	5.907e-1	1.054	...[b]
1e+9	11	1.457	1.310e-1	8.431e-2	1.878	1.138e+0	1.008e+0	1.942	9.016e-1	8.155e-1	1.202	...[b]
1e+9	12	1.556	1.099e-1	6.654e-2	2.025	1.146e+0	1.016e+0	2.041	9.098e-1	8.227e-1	1.206	...[b]

Continued on Next Page...

[10] See Appendix A and Section 2 for more details.
[11] See Appendix B and Section 5.1 for details of the recalibration.
[12] See Section 5.2 for details of the derivation of s and $\tau_{\rm cool}$.

TABLE C1 – Continued

$\rho_{c,0}$ (g cm^{-3})	r	$t_{\rm DDT}$ (s)	$M_{\rm IGE}(t_{\rm DDT})$ ($M_\odot$)	$M_{^{56}{\rm Ni}}(t_{\rm DDT})$ ($M_\odot$)	$t_{\rm IGE}$ (s)	$M_{\rm IGE}(t_{\rm IGE})$ ($M_\odot$)	$M_{^{56}{\rm Ni}}(t_{\rm IGE})$ ($M_\odot$)	$t^*_{\rm DDT}$ (s)	$M^*_{\rm IGE}(t^*_{\rm IGE})$ ($M_\odot$)	$M^*_{^{56}{\rm Ni}}(t^*_{\rm IGE})$ ($M_\odot$)	s	$\tau_{\rm cool}$ (yr)
1e+9	13	2.048	2.017e-1	1.429e-1	2.473	7.969e-1	6.920e-1	2.533	5.608e-1	4.990e-1	0.980	...[b]
1e+9	14	1.600	1.616e-1	1.135e-1	2.015	1.061e+0	9.410e-1	2.085	8.246e-1	7.480e-1	1.161	...[b]
1e+9	15	1.441	1.169e-1	7.452e-2	1.863	1.121e+0	9.955e-1	1.927	8.850e-1	8.026e-1	1.194	...[b]
1e+9	16	1.629	1.756e-1	1.198e-1	2.106	1.028e+0	9.049e-1	2.114	7.923e-1	7.120e-1	1.139	...[b]
1e+9	17	1.721	1.701e-1	1.204e-1	2.136	1.012e+0	8.951e-1	2.206	7.757e-1	7.021e-1	1.132	...[b]
1e+9	18	1.407	1.160e-1	7.173e-2	1.906	1.154e+0	1.022e+0	1.892	9.175e-1	8.295e-1	1.210	...[b]
1e+9	19	1.691	1.690e-1	1.157e-1	2.068	9.690e-1	8.524e-1	2.176	7.330e-1	6.594e-1	1.103	...[b]
1e+9	20	1.643	1.910e-1	1.341e-1	2.166	9.528e-1	8.358e-1	2.128	7.168e-1	6.428e-1	1.092	...[b]
1e+9	21	1.299	9.447e-2	5.357e-2	1.824	1.187e+0	1.052e+0	1.784	9.513e-1	8.589e-1	1.226	...[b]
1e+9	22	1.535	1.459e-1	9.739e-2	2.032	9.850e-1	8.697e-1	2.020	7.489e-1	6.767e-1	1.115	...[b]
1e+9	23	1.759	1.648e-1	1.131e-1	2.234	9.643e-1	8.498e-1	2.244	7.283e-1	6.568e-1	1.102	...[b]
1e+9	24	1.666	1.851e-1	1.265e-1	2.179	8.789e-1	7.662e-1	2.151	6.428e-1	5.732e-1	1.041	...[b]
1e+9	25	1.789	1.865e-1	1.315e-1	2.243	8.950e-1	7.846e-1	2.274	6.590e-1	5.916e-1	1.055	...[b]
1e+9	26	1.446	1.348e-1	9.107e-2	1.844	1.112e+0	9.889e-1	1.931	8.758e-1	7.959e-1	1.190	...[b]
1e+9	27	1.392	9.724e-2	6.110e-2	1.845	1.175e+0	1.046e+0	1.877	9.387e-1	8.530e-1	1.223	...[b]
1e+9	28	1.342	1.132e-1	7.015e-2	1.828	1.096e+0	9.702e-1	1.827	8.598e-1	7.772e-1	1.179	...[b]
1e+9	29	1.624	1.738e-1	1.169e-1	2.176	1.014e+0	8.911e-1	2.109	7.783e-1	6.981e-1	1.130	...[b]
1e+9	30	1.571	1.277e-1	8.167e-2	2.000	1.119e+0	9.920e-1	2.056	8.828e-1	7.990e-1	1.192	...[b]
2e+9	1	1.274	2.186e-1	1.056e-1	1.772	9.744e-1	7.991e-1	1.654	7.384e-1	5.879e-1	1.052	7.908e+7
2e+9	2	1.338	2.363e-1	1.183e-1	1.827	8.956e-1	7.246e-1	1.718	6.596e-1	5.133e-1	0.992	7.908e+7
2e+9	3	1.373	2.242e-1	1.122e-1	1.867	9.631e-1	7.917e-1	1.753	7.270e-1	5.804e-1	1.046	7.908e+7
2e+9	4	1.231	2.044e-1	9.844e-2	1.722	1.120e+0	9.398e-1	1.611	8.838e-1	7.285e-1	1.149	7.908e+7
2e+9	5	1.164	2.030e-1	9.237e-2	1.672	1.053e+0	8.705e-1	1.544	8.166e-1	6.592e-1	1.103	7.908e+7
2e+9	6	1.278	1.909e-1	8.627e-2	1.779	1.054e+0	8.780e-1	1.658	8.180e-1	6.668e-1	1.109	7.908e+7
2e+9	7	1.237	1.942e-1	8.247e-2	1.628	1.090e+0	9.049e-1	1.617	8.541e-1	6.936e-1	1.127	7.908e+7
2e+9	8	1.196	1.727e-1	6.563e-2	1.789	1.094e+0	9.092e-1	1.576	8.577e-1	6.979e-1	1.129	7.908e+7
2e+9	9	1.281	2.196e-1	1.018e-1	1.742	1.004e+0	8.231e-1	1.661	7.678e-1	6.118e-1	1.070	7.908e+7
2e+9	10	1.600	2.540e-1	1.408e-1	2.141	8.565e-1	6.948e-1	1.980	6.205e-1	4.835e-1	0.967	7.908e+7
2e+9	11	1.195	1.883e-1	8.399e-2	1.598	1.096e+0	9.183e-1	1.575	8.598e-1	7.070e-1	1.135	7.908e+7
2e+9	12	1.134	1.356e-1	4.169e-2	1.604	1.194e+0	1.007e+0	1.514	9.575e-1	7.957e-1	1.190	7.908e+7
2e+9	13	1.524	2.363e-1	1.168e-1	1.957	8.689e-1	6.994e-1	1.904	6.328e-1	4.882e-1	0.971	7.908e+7
2e+9	14	1.242	2.062e-1	1.029e-1	1.727	1.016e+0	8.468e-1	1.622	7.795e-1	6.356e-1	1.087	7.908e+7
2e+9	15	1.024	1.429e-1	5.202e-2	1.569	1.170e+0	9.880e-1	1.404	9.340e-1	7.768e-1	1.179	7.908e+7
2e+9	16	1.347	2.412e-1	1.257e-1	1.816	9.349e-1	7.629e-1	1.727	6.988e-1	5.516e-1	1.024	7.908e+7
2e+9	17	1.275	2.046e-1	9.945e-2	1.704	1.058e+0	8.838e-1	1.655	8.223e-1	6.726e-1	1.112	7.908e+7
2e+9	18	1.019	1.490e-1	5.379e-2	1.586	1.189e+0	1.003e+0	1.399	9.533e-1	7.921e-1	1.188	7.908e+7
2e+9	19	1.206	1.913e-1	8.005e-2	1.619	1.105e+0	9.195e-1	1.586	8.685e-1	7.083e-1	1.136	7.908e+7
2e+9	20	1.298	2.323e-1	1.153e-1	1.716	1.013e+0	8.333e-1	1.678	7.774e-1	6.220e-1	1.077	7.908e+7
2e+9	21	0.994	1.383e-1	4.546e-2	1.503	1.225e+0	1.034e+0	1.374	9.892e-1	8.231e-1	1.206	7.908e+7
2e+9	22	1.197	1.861e-1	8.048e-2	1.792	1.043e+0	8.660e-1	1.577	8.065e-1	6.548e-1	1.100	7.908e+7
2e+9	23	1.337	2.027e-1	9.030e-2	1.780	9.984e-1	8.230e-1	1.717	7.624e-1	6.117e-1	1.070	7.908e+7
2e+9	24	1.237	2.299e-1	1.069e-1	1.870	8.652e-1	6.905e-1	1.617	6.291e-1	4.792e-1	0.963	7.908e+7
2e+9	25	1.338	2.190e-1	1.059e-1	1.736	9.844e-1	8.099e-1	1.718	7.484e-1	5.986e-1	1.060	7.908e+7
2e+9	26	1.135	1.792e-1	7.881e-2	1.557	1.107e+0	9.315e-1	1.515	8.714e-1	7.202e-1	1.144	7.908e+7
2e+9	27	1.112	1.329e-1	4.918e-2	1.539	1.181e+0	1.008e+0	1.492	9.448e-1	7.970e-1	1.191	7.908e+7
2e+9	28	1.014	1.529e-1	5.527e-2	1.451	1.142e+0	9.583e-1	1.394	9.059e-1	7.471e-1	1.161	7.908e+7
2e+9	29	1.193	2.064e-1	8.958e-2	1.766	1.021e+0	8.368e-1	1.573	7.845e-1	6.255e-1	1.080	7.908e+7
2e+9	30	1.081	1.509e-1	5.572e-2	1.529	1.196e+0	1.008e+0	1.461	9.596e-1	7.971e-1	1.191	7.908e+7
3e+9	1	1.111	2.392e-1	8.266e-2	1.533	1.026e+0	7.969e-1	1.438	7.899e-1	5.726e-1	1.040	2.879e+8
3e+9	2	1.064	2.459e-1	8.436e-2	1.503	1.058e+0	8.240e-1	1.391	8.217e-1	5.997e-1	1.061	2.879e+8
3e+9	3	1.285	2.507e-1	8.898e-2	1.723	8.638e-1	6.488e-1	1.612	6.278e-1	4.244e-1	0.911	2.879e+8

Continued on Next Page...

TABLE C1 – Continued

$\rho_{c,0}$ (g cm^{-3})	r	$t_{\rm DDT}$ (s)	$M_{\rm IGE}(t_{\rm DDT})$ ($M_\odot$)	$M_{^{56}{\rm Ni}}(t_{\rm DDT})$ ($M_\odot$)	$t_{\rm IGE}$ (s)	$M_{\rm IGE}(t_{\rm IGE})$ ($M_\odot$)	$M_{^{56}{\rm Ni}}(t_{\rm IGE})$ ($M_\odot$)	$t^*_{\rm DDT}$ (s)	$M^*_{\rm IGE}(t^*_{\rm IGE})$ ($M_\odot$)	$M^*_{^{56}{\rm Ni}}(t^*_{\rm IGE})$ ($M_\odot$)	s	$\tau_{\rm cool}$ (yr)
3e+9	4	1.174	2.375e-1	8.843e-2	1.751	9.808e-1	7.627e-1	1.501	7.448e-1	5.383e-1	1.013	2.879e+8
3e+9	5	1.022	2.249e-1	7.251e-2	1.556	1.032e+0	8.054e-1	1.349	7.958e-1	5.810e-1	1.047	2.879e+8
3e+9	6	1.024	1.950e-1	4.817e-2	1.531	1.110e+0	8.787e-1	1.351	8.739e-1	6.544e-1	1.100	2.879e+8
3e+9	7	0.998	2.130e-1	5.642e-2	1.414	1.120e+0	8.818e-1	1.325	8.841e-1	6.575e-1	1.102	2.879e+8
3e+9	8	1.039	2.016e-1	5.049e-2	1.538	1.104e+0	8.693e-1	1.367	8.679e-1	6.449e-1	1.093	2.879e+8
3e+9	9	1.141	2.510e-1	8.595e-2	1.652	9.048e-1	6.815e-1	1.469	6.687e-1	4.571e-1	0.943	2.879e+8
3e+9	10	1.401	2.650e-1	1.099e-1	1.881	8.474e-1	6.409e-1	1.728	6.114e-1	4.165e-1	0.903	2.879e+8
3e+9	11	1.046	2.204e-1	6.880e-2	1.484	1.054e+0	8.297e-1	1.373	8.182e-1	6.054e-1	1.065	2.879e+8
3e+9	12	0.965	1.622e-1	3.069e-2	1.478	1.216e+0	9.813e-1	1.292	9.799e-1	7.569e-1	1.167	2.879e+8
3e+9	13	1.341	2.612e-1	9.459e-2	1.777	7.783e-1	5.657e-1	1.669	5.423e-1	3.414e-1	0.821	2.879e+8
3e+9	14	1.076	2.186e-1	7.401e-2	1.578	1.005e+0	7.881e-1	1.403	7.688e-1	5.637e-1	1.033	2.879e+8
3e+9	15	0.947	1.748e-1	4.569e-2	1.413	1.159e+0	9.341e-1	1.274	9.226e-1	7.097e-1	1.137	2.879e+8
3e+9	16	1.129	2.631e-1	9.851e-2	1.664	8.836e-1	6.622e-1	1.456	6.475e-1	4.378e-1	0.924	2.879e+8
3e+9	17	1.129	2.272e-1	7.756e-2	1.589	1.020e+0	8.019e-1	1.456	7.843e-1	5.775e-1	1.044	2.879e+8
3e+9	18	0.890	1.738e-1	4.342e-2	1.426	1.180e+0	9.478e-1	1.217	9.438e-1	7.235e-1	1.146	2.879e+8
3e+9	19	1.204	2.529e-1	8.665e-2	1.639	9.155e-1	6.899e-1	1.531	6.794e-1	4.655e-1	0.950	2.879e+8
3e+9	20	1.176	2.544e-1	9.120e-2	1.608	9.708e-1	7.453e-1	1.503	7.347e-1	5.210e-1	0.999	2.879e+8
3e+9	21	0.895	1.713e-1	4.005e-2	1.403	1.195e+0	9.655e-1	1.222	9.594e-1	7.411e-1	1.157	2.879e+8
3e+9	22	1.028	2.095e-1	6.057e-2	1.509	1.058e+0	8.335e-1	1.355	8.223e-1	6.092e-1	1.068	2.879e+8
3e+9	23	1.213	2.392e-1	7.568e-2	1.626	9.500e-1	7.260e-1	1.540	7.139e-1	5.017e-1	0.982	2.879e+8
3e+9	24	1.038	2.525e-1	8.053e-2	1.647	8.788e-1	6.479e-1	1.365	6.428e-1	4.236e-1	0.910	2.879e+8
3e+9	25	1.203	2.463e-1	9.050e-2	1.629	9.745e-1	7.522e-1	1.530	7.384e-1	5.278e-1	1.004	2.879e+8
3e+9	26	0.984	2.020e-1	5.757e-2	1.385	1.109e+0	8.828e-1	1.312	8.728e-1	6.584e-1	1.103	2.879e+8
3e+9	27	1.003	1.638e-1	3.844e-2	1.433	1.172e+0	9.547e-1	1.331	9.360e-1	7.304e-1	1.150	2.879e+8
3e+9	28	0.921	1.909e-1	5.010e-2	1.375	1.123e+0	8.973e-1	1.249	8.866e-1	6.729e-1	1.113	2.879e+8
3e+9	29	1.011	2.293e-1	6.818e-2	1.490	1.025e+0	7.908e-1	1.339	7.894e-1	5.665e-1	1.036	2.879e+8
3e+9	30	1.038	1.857e-1	4.406e-2	1.473	1.137e+0	9.113e-1	1.366	9.013e-1	6.869e-1	1.122	2.879e+8
4e+9	1	0.996	2.532e-1	6.652e-2	1.449	1.050e+0	7.802e-1	1.295	8.138e-1	5.443e-1	1.018	5.682e+8
4e+9	2	0.958	2.501e-1	5.462e-2	1.376	1.083e+0	8.002e-1	1.258	8.465e-1	5.642e-1	1.034	5.682e+8
4e+9	3	1.182	2.528e-1	5.884e-2	1.581	9.215e-1	6.633e-1	1.482	6.855e-1	4.274e-1	0.914	5.682e+8
4e+9	4	1.092	2.416e-1	6.524e-2	1.683	9.218e-1	6.719e-1	1.392	6.857e-1	4.359e-1	0.922	5.682e+8
4e+9	5	0.898	2.296e-1	4.362e-2	1.344	1.095e+0	8.208e-1	1.198	8.589e-1	5.848e-1	1.050	5.682e+8
4e+9	6	0.935	2.141e-1	3.618e-2	1.436	1.109e+0	8.331e-1	1.235	8.732e-1	5.972e-1	1.059	5.682e+8
4e+9	7	0.943	2.383e-1	4.479e-2	1.390	1.111e+0	8.314e-1	1.243	8.749e-1	5.954e-1	1.058	5.682e+8
4e+9	8	1.041	2.287e-1	3.968e-2	1.524	1.029e+0	7.590e-1	1.341	7.930e-1	5.231e-1	1.001	5.682e+8
4e+9	9	1.009	2.551e-1	5.758e-2	1.513	9.731e-1	7.033e-1	1.309	7.370e-1	4.673e-1	0.952	5.682e+8
4e+9	10	1.306	2.604e-1	6.975e-2	1.739	8.840e-1	6.309e-1	1.606	6.479e-1	3.950e-1	0.881	5.682e+8
4e+9	11	0.966	2.429e-1	5.893e-2	1.385	1.078e+0	8.134e-1	1.266	8.423e-1	5.775e-1	1.044	5.682e+8
4e+9	12	0.911	1.863e-1	2.445e-2	1.411	1.202e+0	9.346e-1	1.211	9.661e-1	6.986e-1	1.130	5.682e+8
4e+9	13	1.243	2.776e-1	7.328e-2	1.693	8.450e-1	5.828e-1	1.543	6.090e-1	3.468e-1	0.828	5.682e+8
4e+9	14	0.991	2.307e-1	5.550e-2	1.432	1.040e+0	7.836e-1	1.291	8.035e-1	5.477e-1	1.021	5.682e+8
4e+9	15	0.857	1.973e-1	3.404e-2	1.295	1.174e+0	9.107e-1	1.157	9.383e-1	6.747e-1	1.114	5.682e+8
4e+9	16	1.072	2.842e-1	8.135e-2	1.520	9.316e-1	6.651e-1	1.372	6.956e-1	4.291e-1	0.916	5.682e+8
4e+9	17	0.982	2.230e-1	5.106e-2	1.475	1.068e+0	8.094e-1	1.282	8.320e-1	5.735e-1	1.041	5.682e+8
4e+9	18	0.761	1.836e-1	3.043e-2	1.272	1.224e+0	9.556e-1	1.061	9.875e-1	7.196e-1	1.143	5.682e+8
4e+9	19	1.103	2.649e-1	6.228e-2	1.518	9.185e-1	6.502e-1	1.403	6.824e-1	4.142e-1	0.901	5.682e+8
4e+9	20	1.087	2.577e-1	6.216e-2	1.549	9.537e-1	6.863e-1	1.387	7.177e-1	4.504e-1	0.936	5.682e+8
4e+9	21	0.780	1.877e-1	2.909e-2	1.286	1.228e+0	9.640e-1	1.080	9.919e-1	7.281e-1	1.149	5.682e+8
4e+9	22	0.954	2.283e-1	4.964e-2	1.456	1.019e+0	7.587e-1	1.254	7.827e-1	5.227e-1	1.000	5.682e+8
4e+9	23	1.130	2.532e-1	5.409e-2	1.637	8.991e-1	6.326e-1	1.430	6.631e-1	3.966e-1	0.883	5.682e+8
4e+9	24	0.941	2.751e-1	5.869e-2	1.506	8.969e-1	6.151e-1	1.241	6.608e-1	3.791e-1	0.864	5.682e+8
4e+9	25	1.073	2.644e-1	6.909e-2	1.538	9.503e-1	6.829e-1	1.373	7.142e-1	4.470e-1	0.933	5.682e+8
4e+9	26	0.922	2.217e-1	4.436e-2	1.397	1.097e+0	8.284e-1	1.222	8.612e-1	5.924e-1	1.055	5.682e+8

Continued on Next Page...

TABLE C1 – Continued

$\rho_{c,0}$ (g cm^{-3})	r	$t_{\rm DDT}$ (s)	$M_{\rm IGE}(t_{\rm DDT})$ ($M_\odot$)	$M_{^{56}{\rm Ni}}(t_{\rm DDT})$ ($M_\odot$)	$t_{\rm IGE}$ (s)	$M_{\rm IGE}(t_{\rm IGE})$ ($M_\odot$)	$M_{^{56}{\rm Ni}}(t_{\rm IGE})$ ($M_\odot$)	$t^*_{\rm DDT}$ (s)	$M^*_{\rm IGE}(t^*_{\rm IGE})$ ($M_\odot$)	$M^*_{^{56}{\rm Ni}}(t^*_{\rm IGE})$ ($M_\odot$)	s	$\tau_{\rm cool}$ (yr)
4e+9	27	0.909	1.905e-1	3.106e-2	1.348	1.167e+0	9.091e-1	1.209	9.308e-1	6.731e-1	1.113	5.682e+8
4e+9	28	0.873	2.169e-1	4.070e-2	1.321	1.121e+0	8.550e-1	1.173	8.848e-1	6.191e-1	1.075	5.682e+8
4e+9	29	0.953	2.442e-1	4.582e-2	1.522	9.938e-1	7.150e-1	1.253	7.577e-1	4.790e-1	0.963	5.682e+8
4e+9	30	0.912	1.922e-1	2.870e-2	1.418	1.164e+0	8.932e-1	1.212	9.284e-1	6.573e-1	1.102	5.682e+8
5e+9	1	0.993	2.659e-1	5.307e-2	1.441	9.871e-1	6.823e-1	1.282	7.510e-1	4.344e-1	0.921	9.625e+8
5e+9	2	0.964	2.683e-1	4.278e-2	1.357	1.040e+0	7.268e-1	1.252	8.037e-1	4.789e-1	0.962	9.625e+8
5e+9	3	1.151	2.732e-1	4.979e-2	1.593	8.698e-1	5.775e-1	1.439	6.338e-1	3.296e-1	0.807	9.625e+8
5e+9	4	1.010	2.522e-1	4.409e-2	1.589	9.855e-1	6.843e-1	1.298	7.495e-1	4.364e-1	0.923	9.625e+8
5e+9	5	0.835	2.397e-1	3.034e-2	1.303	1.073e+0	7.673e-1	1.123	8.366e-1	5.195e-1	0.998	9.625e+8
5e+9	6	0.919	2.352e-1	3.124e-2	1.425	1.094e+0	7.911e-1	1.207	8.575e-1	5.432e-1	1.017	9.625e+8
5e+9	7	0.871	2.459e-1	3.091e-2	1.368	1.071e+0	7.635e-1	1.159	8.346e-1	5.157e-1	0.994	9.625e+8
5e+9	8	1.079	2.583e-1	4.057e-2	1.553	9.488e-1	6.520e-1	1.367	7.127e-1	4.042e-1	0.891	9.625e+8
5e+9	9	1.028	2.723e-1	3.992e-2	1.438	9.257e-1	6.253e-1	1.316	6.897e-1	3.775e-1	0.862	9.625e+8
5e+9	10	1.321	2.654e-1	3.999e-2	1.744	8.197e-1	5.304e-1	1.609	5.836e-1	2.825e-1	0.746	9.625e+8
5e+9	11	0.945	2.598e-1	4.614e-2	1.369	1.020e+0	7.213e-1	1.234	7.844e-1	4.735e-1	0.958	9.625e+8
5e+9	12	0.893	2.114e-1	2.626e-2	1.402	1.186e+0	8.934e-1	1.181	9.502e-1	6.455e-1	1.094	9.625e+8
5e+9	13	1.168	2.718e-1	4.903e-2	1.658	8.762e-1	5.797e-1	1.457	6.401e-1	3.318e-1	0.810	9.625e+8
5e+9	14	0.957	2.477e-1	4.220e-2	1.356	1.051e+0	7.527e-1	1.246	8.148e-1	5.048e-1	0.985	9.625e+8
5e+9	15	0.816	2.211e-1	3.014e-2	1.230	1.168e+0	8.686e-1	1.104	9.317e-1	6.207e-1	1.076	9.625e+8
5e+9	16	0.962	2.841e-1	5.486e-2	1.476	9.264e-1	6.173e-1	1.250	6.903e-1	3.694e-1	0.854	9.625e+8
5e+9	17	0.952	2.412e-1	3.602e-2	1.394	1.017e+0	7.242e-1	1.240	7.806e-1	4.764e-1	0.960	9.625e+8
5e+9	18	0.708	1.996e-1	2.283e-2	1.240	1.231e+0	9.288e-1	0.996	9.945e-1	6.809e-1	1.118	9.625e+8
5e+9	19	1.056	2.749e-1	4.684e-2	1.514	9.454e-1	6.377e-1	1.345	7.093e-1	3.898e-1	0.876	9.625e+8
5e+9	20	1.017	2.628e-1	3.967e-2	1.450	9.610e-1	6.549e-1	1.305	7.250e-1	4.070e-1	0.894	9.625e+8
5e+9	21	0.738	2.054e-1	2.201e-2	1.248	1.230e+0	9.259e-1	1.026	9.936e-1	6.781e-1	1.116	9.625e+8
5e+9	22	0.872	2.439e-1	4.205e-2	1.420	1.057e+0	7.587e-1	1.160	8.213e-1	5.108e-1	0.990	9.625e+8
5e+9	23	1.090	2.600e-1	3.872e-2	1.487	9.235e-1	6.318e-1	1.379	6.874e-1	3.839e-1	0.869	9.625e+8
5e+9	24	0.877	2.843e-1	4.293e-2	1.417	9.215e-1	6.055e-1	1.165	6.854e-1	3.577e-1	0.840	9.625e+8
5e+9	25	1.034	2.672e-1	4.927e-2	1.469	9.410e-1	6.431e-1	1.323	7.050e-1	3.952e-1	0.881	9.625e+8
5e+9	26	0.898	2.510e-1	4.255e-2	1.344	1.098e+0	7.913e-1	1.186	8.615e-1	5.435e-1	1.017	9.625e+8
5e+9	27	0.985	2.265e-1	3.279e-2	1.413	1.094e+0	8.063e-1	1.274	8.583e-1	5.584e-1	1.029	9.625e+8
5e+9	28	0.795	2.264e-1	2.744e-2	1.272	1.146e+0	8.445e-1	1.084	9.096e-1	5.966e-1	1.059	9.625e+8
5e+9	29	0.891	2.486e-1	3.129e-2	1.406	1.027e+0	7.174e-1	1.180	7.907e-1	4.695e-1	0.954	9.625e+8
5e+9	30	0.868	2.162e-1	2.560e-2	1.343	1.160e+0	8.600e-1	1.156	9.239e-1	6.122e-1	1.070	9.625e+8

[a] As discussed in Section 3.1.2, the results of $\rho_{c,0} = 1.0 \times 10^9$ g cm^{-3}, realization 8 were excluded from the analysis.
[b] As discussed in Section 5.2, the results of Lesaffre et al. (2006) do not allow us to generate cooling times for results with $\rho_{c,0} = 1.0 \times 10^9$ g cm^{-3}.

Chapter 5

Conclusions and Future Work

5.1 Summary and Conclusions

My research into SNeIa used a customized version of the `FLASH` code to perform a suite of two-dimensional simulations. Applying the statistical method of Townsley et al. (2009), I generated five different progenitor WDs, each with a different initial central density, and performed thirty different simulations of each progenitor with randomized initial flame surfaces. Based on analysis of these simulations, I provided a theoretical explanation of the observed trend that SNeIa from older stellar populations are systematically dimmer. I showed that, due to the strongly non-linear processes involved, a statistical study of many simulations is important to capturing the true trends in SNeIa. For the initial conditions that I used, $15-20$ different initial flame surfaces are necessary to capture statistically significant trends.

Additionally, I find that SNeIa from my simulations match the qualitiative requirements to fall along the observed WLR: the mass of ^{56}Ni varies, correlating approximately to moving along the WLR; the mass of IGEs is statistically constant, but has some small variation, which correlates approximately to the width of the WLR; the ^{56}Ni is well-mixed out to a high enclosed mass. Despite being well-mixed, the ^{56}Ni does show some clumpiness, which could potentially give rise to observable line-of-sight variations in observations of SNeIa.

Using the results of Lesaffre et al. (2006), I connected the central density of the progenitor immediately prior to the ignition of the deflagration to the age of the progenitor, allowing my research on the question of the central density to shed light on the question of variations of SNeIa with the age of the host stellar population, a question which observers have been studying in order to control for systematic biases in cosmological studies. I presented a potentially-observable trend that could determine the relative ages of the progenitors of two SNeIa with the same brightness. The mass of stable IGEs is tightly correlated with the central density, and therefore the age.

5.2 Future Work

The collaboration that I worked with on this research is currently investigating several aspects of this problem, and is seeking to improve our models. Turbulence is inherently different in three dimensions than it is in two dimensions, so a current goal of the collaboration

is to develop three-dimensional models. This includes modifying the method for randomizing the initial conditions, and also includes a model for the interactions between turbulence and the flame front. The collaboration is also pursuing post-processing of tracer particles to verify the energetics and nucleosynthesis of our simulations, and present greater detail of the nucleosynthetic yield.

The next step for my own research within this collaboration is a study of the influence of the carbon fraction in the core of the progenitor WD. At this stage, it will first require a literature search to understand previous work on this topic, as well as to determine believable initial conditions for progenitor WD models. This carbon fraction study will be performed analagously to the central density study presented in Krueger et al. (2010) and Krueger et al. (2012), using a suite of two-dimensional simulations.

Part II

Classical Novae

Chapter 6

Overview

Classical novae are scientifically interesting for numerous reasons:

- They are potentially very important to the theory of SNeIa, as they may be the mechanism by which the massive WDs that are needed as SNIa progenitors are made. However, this connection is still being debated.
- While CNe are not as bright as SNeIa, and are therefore not visible from such great distances, they can be calibrated through a relationship between their maximum magnitude and their rate of decline, and used as distance indicators (della Valle & Livio, 1995).
- Novae have a strong impact on the interstellar medium: though they eject less matter per event than supernovae, novae are more numerous and likely contribute a comparable amount of matter to the interstellar medium. Due to the difference in nucleosynthesis between novae and supernovae, novae likely produce more intermediate-mass elements, and may be the dominant sources of certain isotopes, possibly including ^{7}Li, ^{13}C, ^{15}N, ^{17}O, ^{22}Na, and ^{26}Al.
- Because nova nucleosynthesis proceeds at temperatures and densities obtainable in a laboratory, they may be valuable tests for laboratory astrophysics (José & Iliadis, 2011).
- Novae provide an opportunity to study circumstellar dust formation in real time.
- Most close binaries may go through a nova phase, so understanding novae may be significant for binary stellar evolution.
- Novae pose many open questions related to light curves and spectra, and provide an excellent opportunity to study non-steady-state radiation transport.

For recent compilations that review CNe observations and theory, see Hernanz & José (2002) and Bode & Evans (2008).

My study of CNe is still a work in progress. The next few chapters will detail the work I have done and my plans for future work to complete, and potentially extend, the project.

6.1 Historical Overview

Many phenomena can result from mass transfer onto a WD from a non-degenerate companion. Some are observed to brighten and dim (this can be periodic or aperiodic); such systems are referred to as cataclysmic variables (CVs). There are many CV subtypes, including classical novae, recurrent novae, dwarf novae, and a number of others that are typically named after a prototype system representative of that class (Downes et al., 2001).

Theories about novae date back at least as far as Newton's *Principia Mathematica* (Newton, 1687; see also José & Iliadis, 2011): "So fixed stars, that have been gradually wasted by the light and vapors emitted from them for a long time, may be recruited by comets that fall upon them; and from this fresh supply of new fuel those old stars, acquiring new splendor, may pass for new stars." The study of novae also includes one of the most concise research papers ever written (Hartmann, 1925), which reads in its entirety, "Nova problem solved. Star inflates, bursts." However, the modern theory of CVs could be argued to begin with Joy (1943), who first deduced the binary nature of a CV (specifically the AE Aquarii system). Walker (1954) showed that one of the two stars in the DQ Herculis system must be compact due to the short period, which implied very small separation of the two stars. Struve (1955) generalized these two findings and proposed that all CVs are close binary systems. Crawford & Kraft (1956) presented a model for AE Aquarii that serves as a prototype for all CV systems: one star overflowing its Roche lobe and transferring mass onto a compact companion; this model was shown to apply to ten nova systems by Kraft (1964).

Because of the high thermal conductivity of degenerate matter, it was initially believed that heat would be transported away from the energy-generation region too rapidly for the temperature to rise sufficiently to ignite a thermonuclear runaway. Giannone & Weigert (1967) show that the matter is not fully degenerate, therefore the thermal conductivity is low enough that the temperature is able to rise and ignite a thermonuclear runaway. Sparks (1969) performed simulations of shocks in the envelope of a star and showed that the resulting light curves resemble novae.

6.2 Enrichment

Starrfield et al. (1972) determined that the fraction of carbon, nitrogen, and oxygen in the WD's accreted envelope prior to the explosion must be greater than the fraction present in the sun in order to generate sufficent energy for a nova outburst; this is referred to as enrichment. Without enrichment, expansion quenches the burning before enough energy has been released for an outburst. Carbon, nitrogen, and oxygen catalyze hydrogen burning through the CNO cycle (see Section 9.1), so the burning proceeds fast enough to generate sufficient energy for an outburst before expansion can quench the burning. This theoretical prediction was supported by observations that showed the abundances of nova remnants could only result if the pre-outburst abundances were enriched (Gehrz et al., 1998).

The source of the enrichment is believed to be some sort of mixing between the accreted envelope (primarily hydrogen and helium) and the underlying core (in the case of CNe, believed to be primarily carbon and oxygen). The mechanism(s) of this mixing are unknown, with suggestions including

- diffusion across the boundary, which builds a mixed layer that heats and induces convection (Prialnik & Kovetz, 1984; Kovetz & Prialnik, 1985; Iben & MacDonald, 1985; Iben et al., 1991, 1992; Fujimoto & Iben, 1992);
- shear instabilities along the boundary, particularly as caused by differential rotation during the accretion phase (Durisen, 1977; Kippenhahn & Thomas, 1978; MacDonald, 1983; Livio & Truran, 1987; Kutter & Sparks, 1987; Sparks & Kutter, 1987; Kutter & Sparks, 1989; Fujimoto, 1988);
- convection-induced shear instabilities, particularly breaking gravity waves on the core-envelope boundary (Rosner et al., 2001; Alexakis et al., 2002; Calder et al., 2002a; Alexakis et al., 2004);
- convective undershoot, where convective motions induced in the envelope begin to penetrate into the core and dredge up core material (Woosley, 1986; Glasner & Livne, 1995; Glasner et al., 1997; Kercek et al., 1998, 1999; Glasner et al., 2011).

This question of enrichment and mixing is the focus of my research into CNe, with the goal being an understanding of how this mixing occurs, how fast it takes place, and how much material is mixed across the core-envelope boundary.

6.3 The State of Modern Simulations

The majority of simulation work on nova explosions has been one-dimensional, with convection described by mixing-length theory (see Starrfield, 2002, Glasner et al., 2011, and José & Iliadis, 2011 for reviews). However, most of the proposed mechanisms for enrichment are inherently multidimensional. Most multidimensional studies suggest that convective undershoot may play a significant role in enrichment (Glasner et al., 1997, 2007; Casanova et al., 2010). However, some have seen qualitatively different behavior (Kercek et al., 1998, 1999). Algorithmic differences and the dimensionality of the simulations may play a significant role in the results (Kercek et al., 1999; Glasner et al., 2005; Casanova et al., 2011b). The current uncertainty in the field strongly suggests that multidimensional (especially three-dimensional) simulations may be necessary.

6.4 The `MAESTRO` Code

For this research I used `MAESTRO`, a new hydrodynamics tool designed for low-Mach-number astrophysical flows (Nonaka et al., 2010). Grid based codes are subject to the Courant-Friedrichs-Lewy (CFL) condition, which limits the time step such that information cannot propagate more than a single cell in a single time step (Courant et al., 1928). For a traditional compressible code (e.g., `FLASH`), the speed at which information propagates is equal to the fluid speed plus the sound speed. `MAESTRO` filters out acoustic waves as described below, so that information propagates at the fluid speed. In the low-Mach regime in which `MAESTRO` is valid (Mach number much less than unity, $\mathcal{M} \ll 1$), this allows `MAESTRO` to take time steps longer than those of a traditional compressible code, typically by a factor

of approximately $1/\mathcal{M}$. Unlike other algorithms for low-Mach flow (e.g., incompressible or anelastic), MAESTRO captures important compressibility effects, including local heating (such as from nuclear reactions) and movement through a stratified background. MAESTRO has been tested extensively against compressible algorithms in order to demonstrate the validity of the MAESTRO approximation for flows with Mach number less than approximately 0.3 (Almgren et al., 2006a,b, 2008).

In order to achieve this low-Mach approximation, MAESTRO assumes a one-dimensional base state that is in hydrostatic equilibrium (HSE), and uses a variation of the Euler equations[1] to compute the multidimensional perturbations to this hydrostatic base state:

$$\nabla P_0 = -\rho_0 \mathbf{g} \tag{6.1a}$$

$$\frac{\partial (\rho X_k)}{\partial t} = -\nabla \cdot (\rho X_k \mathbf{u}) + \rho \dot{\omega}_k \tag{6.1b}$$

$$\frac{\partial (\mathbf{u})}{\partial t} = -\mathbf{u} \cdot (\nabla \otimes \mathbf{u}) - \frac{1}{\rho} \nabla \pi - \frac{\rho - \rho_0}{\rho} \mathbf{g} \tag{6.1c}$$

$$\frac{\partial (\rho h)}{\partial t} = -\nabla \cdot (\rho h \mathbf{u}) + \frac{DP_0}{Dt} + \rho \, \dot{h}_{\mathrm{nuc}} \tag{6.1d}$$

$$\nabla \cdot (\beta_0 \mathbf{u}) = \beta_0 \left(S - \frac{1}{\overline{\Gamma}_1 P_0} \frac{\partial P_0}{\partial t} - \frac{f_{\mathrm{vd}}}{\overline{\Gamma}_1 P_0} \frac{P_0 - P_{\mathrm{EoS}}}{\Delta t} \right), \tag{6.1e}$$

where quantities marked by a bar (e.g., $\overline{S}$) are averaged over a horizontal layer (i.e., an average over all cells with the same radial coordinate), quantities marked with a subscript "EoS" are the result of a call to the EoS with the full-state quantities (e.g., $P_{\mathrm{EoS}} = P_{\mathrm{EoS}}(\rho, T, X_k)$), and quantities marked with a subscript zero refer to the hydrostatic base state.

The first two equations are straightforward: Equation (6.1a) is the equation of hydrostatic equilibrium and defines the base state, while Equation (6.1b) is the same as Equation (2.4) from the usual Euler equations.

Equation (6.1c) corresponds to Equation (2.1b), with two changes. First, the equation for HSE has been added in to change the pressure gradient to a gradient of the pressure perturbation ($\pi = P - P_0$, also known as the dynamic pressure). Second, the density has been factored out of the $\partial (\rho \mathbf{u}) / \partial t$ term to cast this as an equation for velocity instead of momentum density.

Equation (6.1d) corresponds to Equation (2.1c) except for two changes. First, the equation has been reformulated to use specific enthalpy (h) instead of specific total energy (e) or specific internal energy (ε). This change (using some algebra, and substitution from Equation (6.1c)) allows the pressure term to be recast using a notation referred to as a Lagrangian (or "material") derivative:

$$\frac{DP_0}{Dt} \equiv \frac{\partial P_0}{\partial t} + \mathbf{u} \cdot \nabla P_0. \tag{6.2}$$

Accordingly, the energy source has been recast as an enthalpy source. Second, the pressure has been changed from the full-state pressure (P) to the base-state pressure (P_0). This is

[1] See Equation (2.1) for the typical Eulerian equations for compressible reactive hydrodynamics.

the only explicit reference to the full-state pressure (other equations in this set use either the base-state pressure or the pressure perturbation). This change decouples the pressure from the density, filtering out acoustic waves. However, because of this change, it is necessary that the pressure perturbation be small; formally, the requirement is that $|\pi| / P_0$ be of order $\mathcal{M}^2$, leading to the requirement that the Mach number be small.

Equation (6.1e) is an implicit constraint on the velocity field, and is an expression of the EoS. The quantity β_0 is a density-like variable derived in Almgren et al. (2006a), S is a generic source term, Γ_1 is the logarithmic derivative of pressure with respect to density at constant entropy ($\Gamma_1 = (d \log P / d \log \rho)_s$), Δt is the time step, and $f_{\rm vd}$ is known as the "volume discrepancy factor" (a dimensionless constant between zero and unity). Because this constraint equation is a linearization of a non-linear constraint, it is possible for the pressure to drift away from the pressure given by the EoS. The volume discrepancy term is included to counteract this drift and push the pressure into thermodynamic equilibrium (Pember et al., 1998).

Chapter 7

Initial Models

The initial models that I used in my CNe research were provided by Ami Glasner, and match some of the models used in Glasner et al. (2007). The models are a time sequence of one-dimensional CN models from a Lagrangian stellar evolution code, and are named by the peak temperature in the domain (in 10^7 K); the models supplied by Ami Glasner are T3, T3.5, T5, T7, and T9, with T3 being the earliest and T9 the latest as the base of the accreted envelope heats up. Due to differences between a one-dimensional, Lagrangian stellar evolution code and a multidimensional, Eulerian hydrodynamics code, these initial models needed to be modified through a series of steps to be appropriate for use in `MAESTRO`. More detail of these differences will be discusses in Section 7.1.1.

Figure 7.1 shows a sample profile based on Ami Glasner's T5 model. The model extends to a higher radius than is shown; beyond the radial limits of the plot the temperature and composition are constant, with the density determined as described in Section 7.1.2. The upper panel shows the density profile, which clearly shows the sharp density gradient around the core-envelope boundary. The central panel shows the temperature profile. The core is not fully isothermal, but approaches isothermal as the radius goes to zero. Immediately above the core-envelope boundary there is a nearly-isentropic region due to convection (additional discussion of this region is in Section 7.2), and above the convective region the envelope is isothermal. The lower panel shows the composition: the core is an even mixture by mass of ^{12}C and ^{16}O, while the envelope is approximately solar composition.

7.1 Outline of the Initial Model Builder

The goal of my simulations is to study mixing of carbon and oxygen from the core into the envelope. This mixing is expected to be related to convective velocities, which are caused by nuclear energy generation. The peak energy-generation region is where there is a large concentration of hydrogen (the fuel for the reactions) mixed with a significant quantity of carbon (the catalyst) at a high temperature (the reactions are extemely sensitive to temperature). All of these processes are focused on the base of the accreted layer, where the mixing is occurring and the temperature is highest. Therefore, it is necessary to identify the base of the accreted layer, $r_{\rm base}$, as that location will be significant throughout the initial model building process.

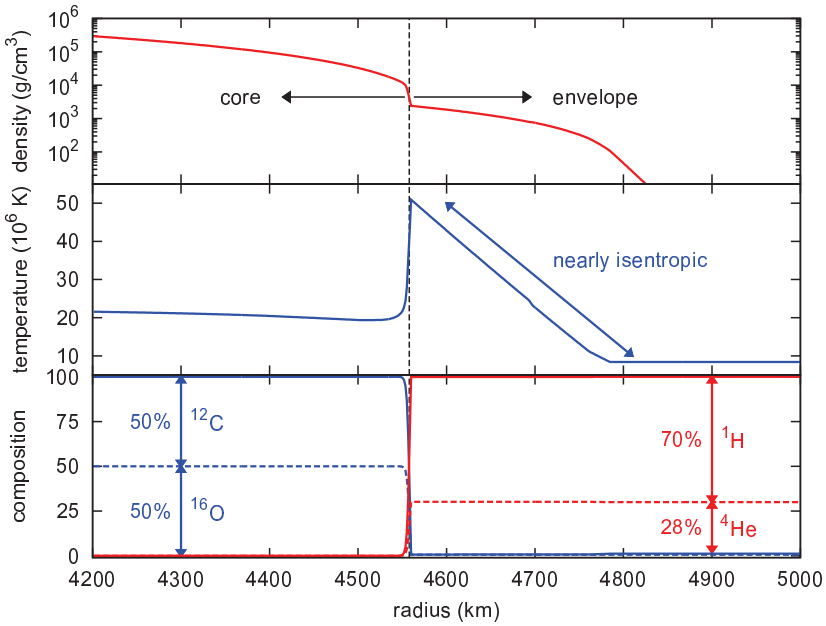

Figure 7.1: This figure shows a sample profile based on Ami Glasner's T5 model. The T5 model has been the basis of all preliminary simulations to date. The model extends to a higher radius than is shown here; the extension is at a constant composition and temperature.

7.1.1 Uniform Grid Interpolation

Hydrodynamics may be described in two frames of reference. The Lagrangian frame is bound to the material: a grid point tracks a parcel of material, and the grid points are allowed to move. The Eulerian frame is bound to space: the grid is stationary in space, and material is allowed to move between grid points. Thus the input models from Ami Glasner's Lagrangian stellar evolution code have arbitrary grid point locations, while `MAESTRO` requires fixed locations on a uniform grid[1]. Figure 7.2 shows a comparison between the Lagrangian input model and a uniform grid model by plotting the density of grid points. Therefore, the first step of converting the initial model is to change the grid structure from the Lagrangian input model by interpolating to a uniform grid. A simple linear interpolation is sufficient; the following steps will modify the profiles and ensure that the correct conditions are met, so it is not necessary to go beyond the simplest interpolation method.

Due to the temperature sensitivity of the nuclear reactions, it is important to capture the peak temperature correctly. Depending on how the cell centers of the uniform grid align with the grid points of the input model, the peak temperature may be "clipped" off: if the uniform grid cell center does not lie precisely at the peak, the interpolation scheme will

[1]Because `MAESTRO` uses adaptive mesh refinement, the grid points are not absolute, but may change in a prescribed way. However, `MAESTRO` initial models need to be defined on the finest grid, assuming that the entire domain will be at the finest resolution. `MAESTRO` will coarsen the initial model as appropriate based on the criteria controlling the adaptive mesh.

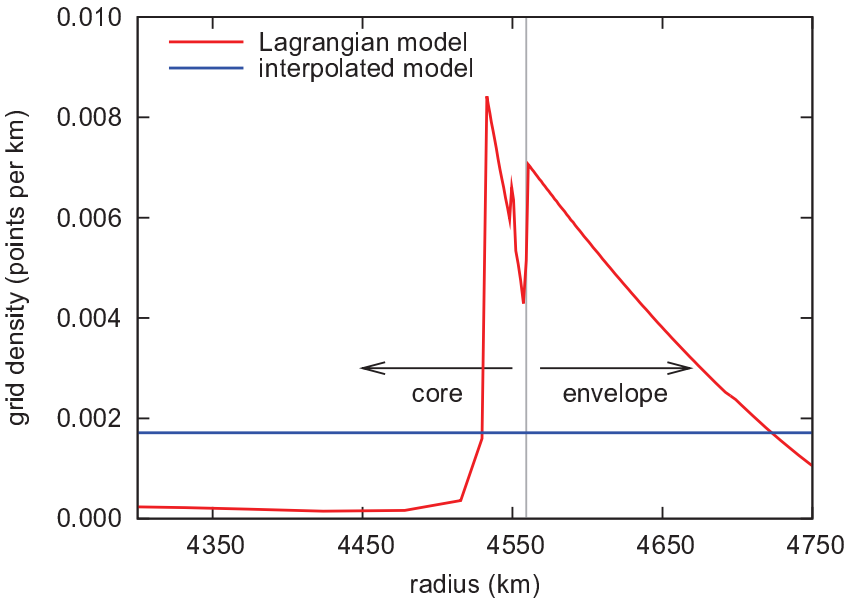

Figure 7.2: This plot shows the density of grid points for the T5 model from Ami Glasner, as well as the same model after interpolation to a uniform grid. By definition, the uniform grid will have a constant grid density, while the variable grid spacing of a Lagrangian code can be seen in the high grid density near the core-envelope interface.

average the peak with the next point down, lowering the peak value. Certain alignments may even cause the true peak to be lowered below the neighboring point, artificially moving the peak and creating a different profile in the vicinity of the new peak; this is shown in Figure 7.3. Therefore the initial model builder shifts the uniform grid slightly in order to place the peak temperature in the center of a cell.

7.1.2 Hydrostatic Equilibrium Integration — First Pass

Because MAESTRO uses a hydrostatic base state, it is important to ensure that the initial model is in HSE. Due to differences in numerical methods and the included physics, HSE can vary from one code to the next due to, e.g., gridding, the EoS, or gravity. Even if the input model was in HSE, we must recompute the structure by integrating the HSE equation:

$$\frac{\partial P}{\partial r} = -\rho g. \tag{7.1}$$

The acceleration of gravity, g, depends on assumptions made about the way that gravity is calculated; for example, common gravity methods include constant gravity, enclosed-mass gravity, and self-gravity. In the case of my simulations, I use a point-source inverse-squared gravity to match the gravity derived for MAESTRO in Section 8.1. The entire initial domain is assumed to be in HSE, so that $P = P_0$ and $\rho = \rho_0$ at $t = 0\,\mathrm{s}$.

In practice, the integration becomes a pair of coupled equations: HSE and the EoS. If we take the superscripts "c" and "p" to refer respectively to the current grid cell we are solving

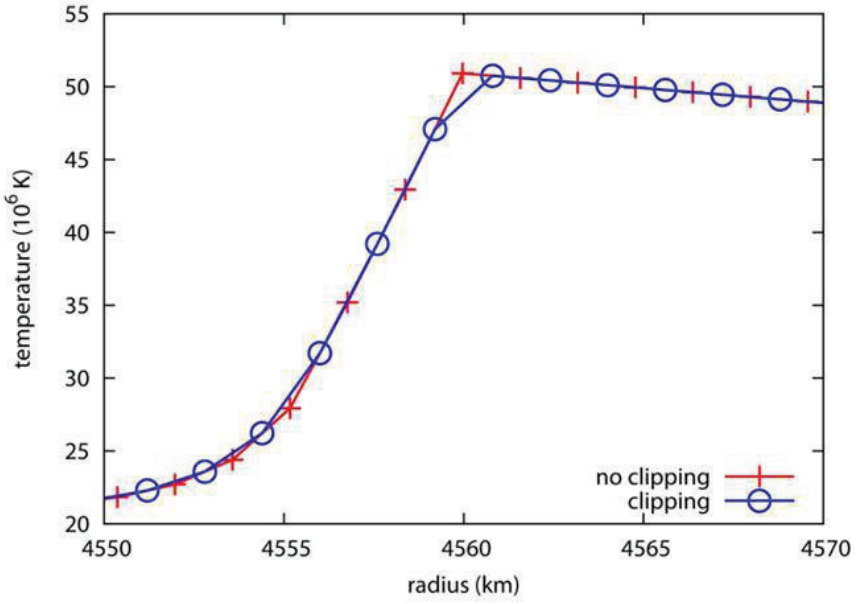

Figure 7.3: A comparison of the temperature peak of the interpolated T5 model. The only difference between the two profiles is that the temperature peak is aligned to the cell center (red profile) or cell edge (blue profile). Notice how the blue profile has "clipped" off the temperature peak, resulting in (a) a lower peak, (b) the peak moving to a higher radius, and (c) a shallower gradient immediately below the peak. The problem becomes more exaggerated as the resolution decreases.

for and the previous cell already solved for,

$$P^{\mathrm{c}} = P^{\mathrm{p}} - \Delta r \left(\frac{\rho^{\mathrm{c}} + \rho^{\mathrm{p}}}{2} \right) g \tag{7.2a}$$

$$P^{\mathrm{c}} = P_{\mathrm{EoS}}(\rho^{\mathrm{c}}, T^{\mathrm{c}}, X_k^{\mathrm{c}}), \tag{7.2b}$$

where g is evaluated between the current and previous grid cells. A Newton-Raphson loop solves this pair of equations by iterating on ρ^{c} in order to bring these two expressions for the pressure into agreement. The temperature and composition profiles given by the interpolation from the input model are unchanged, so T^{c} and X_k^{c} are known for all cells. This integration also requires a boundary condition: due to the importance of the base of the accreted layer, the density at r_{base} is taken as the boundary condition, with the pressure at r_{base} given by an EoS call. Integration proceeds in two sweeps: one integration sweep upwards from the base and one downward from the base. At the upper end of the domain, as the density falls off, a tunable parameter determines a cutoff density below which the star is said to be in the "fluff": a region of such low density as to be essentially irrelevant to the dynamics of the mixing. When the model falls into this region, the density is set to be equal to this cutoff density and the temperature is set to a constant value. The HSE integration core was adopted from previous initial model builders developed by the `MAESTRO` team.

7.1.3 Smoothing

Due to the conceptual differences between a Lagrangian fluid dynamics code and an Eulerian fluid dynamics code, the two methods have different capabilities. A Lagrangian code is capable of having boundaries as thin as the spacing between two grid points, while Eulerian codes often have difficulties with sharp discontinuities and will tend to smooth them out. The input models supplied by Ami Glasner contain such a thin discontinuity: one grid point is a hot, low-density mixture dominated by hydrogen and helium, while the adjacent grid point below it is a cool, high-density mixture of carbon and oxygen. This discontinuity is not expected to be so narrow in a real CN progenitor, so both for reasons of the physics of the situation and the ability of the numerics, it is necessary to smooth out this interface across a wider radial range. I implemented and tested a variety of smoothing methods.

Kernel Smoothing

Kernel smoothing takes all data points around the current grid point and performs a weighted average according to some smoothing kernel; essentially, this is a convolution of the original profile with the smoothing kernel function. The smoothing kernel function is typically symmetric and peaks in the center; for my implementation, I used a Gaussian. Unfortunately, the kernel smoothing method modifies the entire domain and does not preserve all of the important features of the initial model (e.g., the temperature peak), so it was rejected.

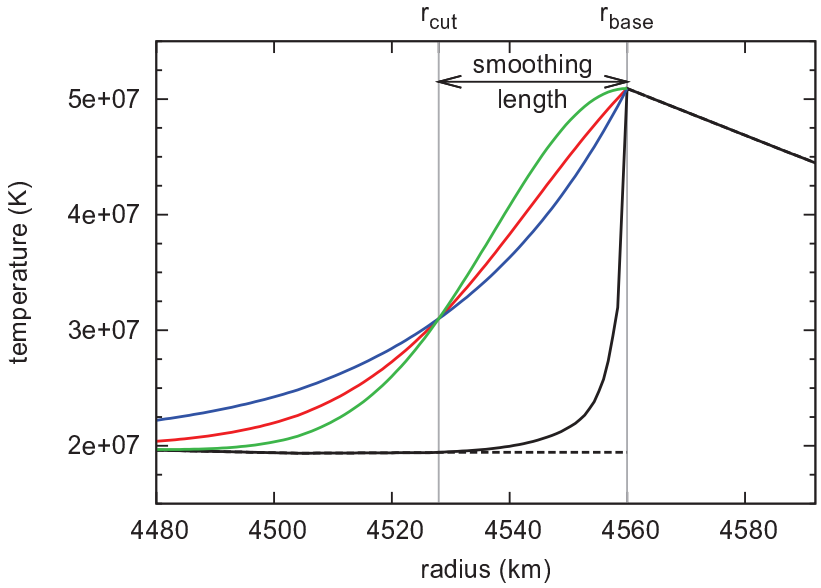

Figure 7.4: Demonstration of the transition smoothing method on the temperature profile. The solid black profile shows the unsmoothed profile, while the dotted line shows where the transition was cut out. The colored profiles show the new transition shape being added in: green is the Gaussian, blue is the exponential, and red is the hyperbolic tangent. The smoothing length has been exaggerated to clearly show the transition shapes.

Transition Smoothing

Transition smoothing erases the transition region immediately below the base of the accreted layer and replaces it with a specified transition shape. Centering the new transition shape on $r_{\rm base}$ leads to changes in the thermodynamics of the base of the accreted envelope, hence only the region below the base is modified. The temperature and the composition are typically the only two quantities smoothed by this method; the density and pressure will be updated in the next step. This smoothing method requires the specification of a transition shape and a smoothing length ($\ell_{\rm sm}$) which determines the width of the transition. The method of performing this smoothing is to mark the base of the accreted layer and the point one smoothing length below the base (call this the cut point; $r_{\rm cut} = r_{\rm base} - \ell_{\rm sm}$), then erase the the region between the cut point and the base and replace it with a straight line at the same level as the cut point; i.e., for a quantity q, $q(r_{\rm cut} < r < r_{\rm base}) = q(r_{\rm cut})$. Then the selected transition shape is added to the profile below the base, leaving the profile above the base unchanged during the entire smoothing step. This is demonstrated in Figure 7.4: the solid black profile shows the temperature profile prior to smoothing, then the dotted line shows where the transition was removed. The colored profiles show various new transition shapes added in to create a new transition. The three transition shapes intersect at both $r_{\rm cut}$ and $r_{\rm base}$, splitting the profile below the base into two regions: the upper core ($r_{\rm cut} < r < r_{\rm base}$) and the inner core ($r < r_{\rm cut}$).

Gaussian: The first transition shape is a half-Gaussian, centered at the base and extending to lower radii. The standard deviation of the Gaussian is set to $\ell_{\rm sm}$, and the height is scaled to connect at $r_{\rm base}$. This profile has the advantage of being smooth at $r_{\rm base}$ and rapidly falls to the original profile away from the base. However, it changes the input model immediately below the base (the upper core) more than is desired.

Exponential: The second transition shape is an exponential decay of the form $\exp(r/\ell_{\rm sm})$, scaled to connect at $r_{\rm base}$. This transition shape changes the upper core less than the Gaussian profile, but still has a relatively sharp edge between the base of the accreted layer and the top of the core. This shape also has more significant impact than the Gaussian in the inner core.

Hyperbolic tangent: The third transition shape is a hyperbolic tangent centered half a smoothing length below $r_{\rm base}$ and scaled to connect at $r_{\rm base}$. This transition shape has a smoother connection at $r_{\rm base}$ than the exponential and falls away rapidly as the distance increases from $r_{\rm base}$. This transition shape appears to balance the need for a smooth connection at $r_{\rm base}$ (to avoid too sharp of a change between $r_{\rm base}$ and the next grid cell below) and not changing the input model too much in the upper core. The hyperbolic tangent transition shape is the smoothing technique that I am currently using, with some testing remaining to determine if this is acceptible or if a better smoothing method is necessary.

Lowering the Composition Boundary

My research included brief testing of a new variation on the transition smoothing method that separates the composition transition and the hottest zone. One-dimensional stellar evolution codes cannot simulate convection, so convection must be approximated (often through mixing-length theory). Depending on the choice and implementation of the boundary conditions for convection, the boundaries of the convective zone may or may not migrate. It is possible that the convection has not migrated downward to abut the composition gradient. In addition, since Lagrangian codes are able to maintain arbitrarily thin discontinuities, it is possible that a wider and smoother composition transition may result in a temperature peak farther from the center of the transition. Therefore, the relative locations of the temperature peak, the composition transition, and the lower edge of the convective zone may not be captured correctly. In particular, the temperature peak and lower edge of the convective zone might be separated from the composition transition. If the composition transition were wider and farther-separated from the temperature peak, the catalysis of the nuclear reactions could be different, which would change the heating, and therefore the convection, which would in turn feed back on the mixing across the composition transition. Based on these arguments, there may be a physical motivation to force a separation between the temperature peak and the composition boundary. The simplest way to mock up this separation is to simply lower the composition boundary, which is what this new smoothing method was implemented to do. This method is only in preliminary testing stages, and requires some research on initial conditions in order to determine a more physically realistic implementation.

7.1.4 Hydrostatic Equilibrium Integration — Second Pass

The smoothing step changes the temperature and composition profiles, and both of these feed into the EoS and therefore impact the HSE through Equation (7.2b). This necessitates a second pass of the HSE integrator in order to correct the density and pressure profiles. Running a single sweep of the integrator after both the interpolation and smoothing have been performed may lead to unexpected interactions between the interpolation and smoothing processes, so it is important to have two passes of HSE integration, one immediately after the interpolation and one immediately after the smoothing.

7.1.5 Hydrostatic Equilibrium Verification

The final step is to verify the HSE conditions by comparing dP/dr to $-\rho g$ and computing the maximum error. This checks that the Newton-Raphson loop in the HSE integration routine converges and no unexpected errors have arisen. This also mimics the HSE check that `MAESTRO` itself will perform on importing the model, which tells you if `MAESTRO` will have issues with the model.

7.2 Correction of Entropy Discontinuity

Early simulations with these initial models generated velocities in a region where there is no physical reason for such velocities to appear. I traced the problem back to a discontinuity in the initial model. A portion of the accreted envelope is nearly isentropic due to convection, except for a small discontinuity (in both entropy and temperature) in the middle of this region. See Figure 7.5: the upper panel shows the entropy profile, where the discontinuity is more pronounced, but the lower panel shows the temperature profile, which also exhibits this discontinuity. The discontinuity occurs when the temperature is approximately 2.5×10^7 K, which is the temperature when the pp II and pp III branches of the proton-proton reaction chain are equally important (see Figure 7.6). Above this temperature pp III is the dominant energy source, and below it pp II dominates (with another critical temperature around 1.7×10^7 K, below which the pp I branch takes over). While it is possible for some feature to appear here due to the change in reaction chains at this temperature, both the pp II and pp III reaction rates are continuous and smooth so a discontinuity is not expected. While the discontinuity is somewhat small, it is still sufficient to cause two problems. The first is that this convective region, which should mix thoroughly as a single region, is artificially split into two disjoint convective zones that mix independently of each other. The second is the appearance of the unphysical velocities which were problematic in early simulations.

In order to fix the problem, I had to correct for the discontinuity in entropy and temperature. The convection causes the region to be nearly, but not fully, isentropic. Changing it to a truly isentropic profile could change the dynamics by pushing part of the domain across the boundary to being convective when it should not be or vice-versa. I found that a cubic polynomial fit the profile very well when an arbitrary shift was permitted on one side of the discontinuity. Using this cubic polynomial as a guide, I corrected the temperature profile between the discontinuity and the top of the convective region. Above the convective

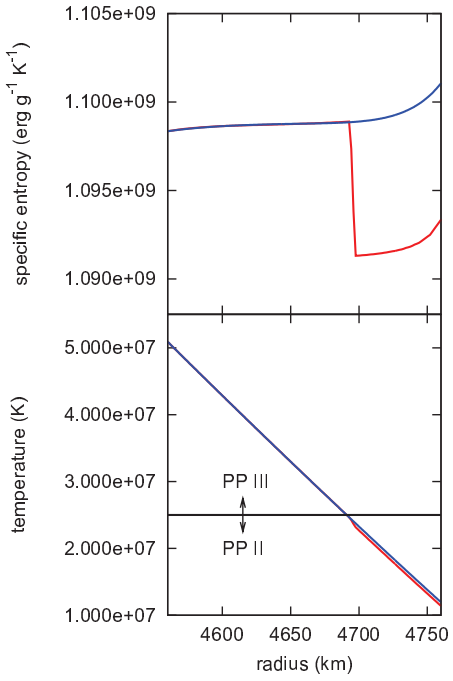

Figure 7.5: Illustration of the discontinuity in the initial model. The top panel shows the specific entropy profile, while the lower panel shows the temperature profile. The red curve is the profile with the discontinuity, which can be seen clearly in the entropy (upper panel) around 4700 km. The blue curve is the corrected version without the discontinuity. The shape of the entropy is unchanged, except for the vertical shift for radii greater than 4700 km.

region the temperature profile is isothermal, which made it simple to connect the corrected profile to the profile above the convective region. This correction was applied just prior to the interpolation to a uniform grid.

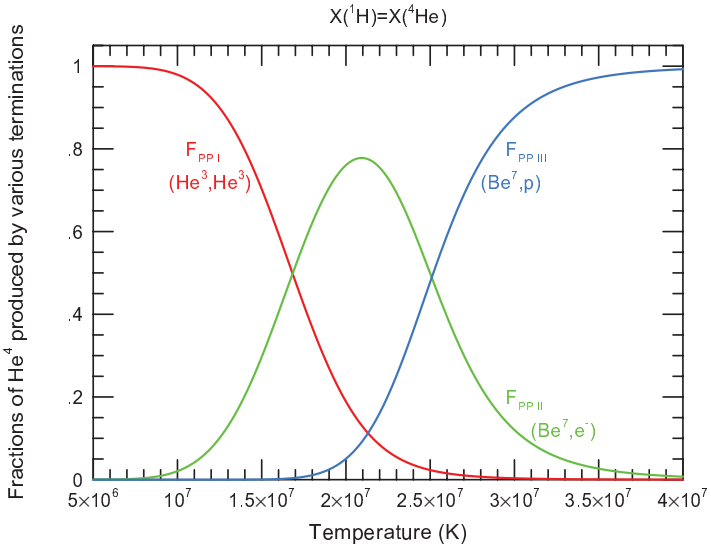

Figure 7.6: Relative contributions of the three branches of the proton-proton chain of nuclear reactions. The critical temperature where the pp II branch gives way to the pp III branch can be see to be around 2.5×10^7 K. This image is reprinted from `http://cococubed.asu.edu/code_pages/burn_hydrogen.shtml` by permission of Frank X. Timmes.

Chapter 8

Modifications to the MAESTRO Code

MAESTRO has been used to simulate multiple astrophysical phenomena (e.g., Malone et al., 2011; Zingale et al., 2011; Nonaka et al., 2012a), but my work is the first time that it has been applied to CNe. Therefore, it was necessary for me to implement a few new routines to include the physics that is needed for CNe but was not needed for previous simulations performed with MAESTRO. In particular, the plane-parallel geometry that I used for my simulations needed a point-source inverse-squared gravity routine, and I needed a new reaction network designed to capture the nucleosynthesis and nuclear energetics involved in CNe.

8.1 Gravity

As CNe occur in a thin accreted layer on the surface of a WD and the core of the WD plays no part in the dynamics of the outburst, it is natural to perform simulations in a plane-parallel mode in order to eliminate the core of the WD from the simulation. In this domain the gravity is dominated by the mass of the WD, with the contributions of the mass in the accreted layer being negligible, so that a full self-gravity or an enclosed-mass gravity is not necessary. However, a constant gravity is not sufficient: the radial extent is large enough that the difference in gravity between the top and bottom of the domain is non-negligible. Thus it was necessary to implement an inverse-squared gravity mode in MAESTRO, which modifies the constraint equation from Equation (6.1e). Instead of using Equation (6.1e) directly, I will use an alternate form that constrains the base-state expansion velocity ($w_0 = \overline{(\mathbf{u} \cdot \mathbf{e}_r)}$), which is derived in the MAESTRO Users' Guide (Lawrence Berkeley National Laboratory & Stony Brook University, 2012):

$$\nabla \cdot (w_0 \mathbf{e}_r) = \overline{S} - \frac{1}{\overline{\Gamma}_1 P_0} \frac{DP_0}{Dt} - \frac{f}{\overline{\Gamma}_1 P_0} \frac{P_0 - \overline{P_{\mathrm{EoS}}}}{\Delta t}. \tag{8.1}$$

In the plane-parallel geometry, $\nabla \cdot (w_0 \mathbf{e}_r) = \partial w_0 / \partial r$. This equation can be simplified by splitting w_0 into $\overline{w_0}$ and δw_0 such that

$$\frac{\partial \overline{w_0}}{\partial r} = \overline{S} - \frac{f}{\overline{\Gamma}_1 P_0} \frac{P_0 - \overline{P_{\mathrm{EoS}}}}{\Delta t}; \tag{8.2}$$

this leaves behind

$$\frac{\partial\,\delta w_0}{\partial r} = -\frac{1}{\overline{\Gamma}_1 P_0}\left(\frac{\partial P_0}{\partial t} + w_0\,\frac{\partial P_0}{\partial r}\right). \tag{8.3}$$

The next step is to multiply through by $\overline{\Gamma}_1 P_0$, differentiate by r, and swap the order of a mixed partial derivative:

$$\frac{\partial}{\partial r}\left[\overline{\Gamma}_1 P_0\,\frac{\partial \delta w_0}{\partial r}\right] = -\frac{\partial}{\partial t}\,\frac{\partial P_0}{\partial r} - \frac{\partial}{\partial r}\left[w_0\,\frac{\partial P_0}{\partial r}\right]. \tag{8.4}$$

Almgren et al. (2008) (Equation (30)) defines

$$\eta_\rho(r) = \overline{((\rho-\rho_0)\,\tilde{w})}, \tag{8.5}$$

where $\tilde{w} = (\mathbf{u} - w_0\mathbf{e}_r)\cdot\mathbf{e}_r$, and shows that (Equation (29))

$$\frac{\partial \rho_0}{\partial t} = -\nabla\cdot(\rho_0 w_0 \mathbf{e}_r) - \nabla\cdot(\eta_\rho \mathbf{e}_r). \tag{8.6}$$

Substitute the HSE equation for the base state (Equation (6.1a)) and Equation (8.6) into Equation (8.4):

$$\begin{aligned}
\frac{\partial}{\partial r}\left[\overline{\Gamma}_1 P_0\,\frac{\partial \delta w_0}{\partial r}\right] &= -\frac{\partial}{\partial t}\,\frac{\partial P_0}{\partial r} - \frac{\partial}{\partial r}\left[w_0\,\frac{\partial P_0}{\partial r}\right] \\
&= \frac{\partial}{\partial t}(\rho_0 g) + \frac{\partial}{\partial r}(w_0\rho_0 g) \\
&= \rho_0\left(\frac{\partial g}{\partial t} + w_0\,\frac{\partial g}{\partial r}\right) + g\left(\frac{\partial}{\partial t}(\rho_0) + \frac{\partial}{\partial r}(w_0\rho_0)\right) \\
&= \rho_0\frac{Dg}{Dt} - g\frac{\partial \eta_\rho}{\partial r}.
\end{aligned} \tag{8.7}$$

Recall that the gravitational acceleration for a point source is $g = Gmr^{-2}$, and m is constant as we are neglecting the gravitational contributions of mass within the domain. Therefore,

$$\begin{aligned}
\frac{Dg}{Dt} &= \frac{D}{Dt}\left(\frac{Gm}{r^2}\right) \\
&= Gm\left(\frac{\partial}{\partial t}\left(\frac{1}{r^2}\right) + w_0\,\frac{\partial}{\partial r}\left(\frac{1}{r^2}\right)\right) \\
&= 0 - \frac{2Gmw_0}{r^3} \\
&= -\frac{2w_0 g}{r}.
\end{aligned} \tag{8.8}$$

Combining Equations (8.7) and (8.8), then splitting w_0 into $\overline{w_0}$ and δw_0, yields the final expression for the constraint equation for point-source gravity in plane-parallel geometry:

$$\frac{\partial}{\partial r}\left[\overline{\Gamma}_1 P_0 \frac{\partial(\delta w_0)}{\partial r}\right] + \frac{2\rho_0 g\, \delta w_0}{r} = -\frac{2\rho_0 g\, \overline{w_0}}{r} - g\frac{\partial \eta_\rho}{\partial r}. \tag{8.9}$$

Although I derived this equation, the discretization and implementation of it was handled by the designers of `MAESTRO`, especially Michael Zingale. Details of the discretization (for both uniform and adaptive grids) are given in Chapter 26 of the `MAESTRO` Users' Guide.

To complete this constraint, it is necessary to specify a boundary condition. The expansion, which is constrained by the equation derived here, is driven by heating, which occurs at the base of the accreted envelope. As the heat is predominantly carried to higher radii, the expansion should be contained in the region above the heating layer; therefore, there should be no expansion velocity at the base of the accreted layer. This gives the boundary condition $w_0(r_{\rm base}) = 0$.

8.2 Initial Convective Field

A one-dimensional stellar evolution code, such as the one Ami Glasner used to generate the input models that I used, can estimate the results of convection through mixing length theory. While mixing length theory can generate a mean radial velocity, it is unable to generate a multidimensional convective velocity field that captures the turnover of convective eddies. Therefore, when I start my simulations in `MAESTRO` I have no initial velocities. This turns out to be a significant issue: without convective velocities, there is no way for energy generated at the base of the accreted layer (the region of maximum energy generation) to be transported away as it would be in a real CN. This leads to isolated zones going into thermonuclear runaway, causing spikes in the temperature and energy generation. These small runaways are completely unphysical. The convective velocity field would have long since been established before temperatures reached the point where such runaways could happen, and would diffuse the energy generated by temperature spikes into the surrounding material. Thus it is necessary to mock up an initial convective velocity field.

The method developed by Michael Zingale was to start by inhibiting (but not forbidding) the runaway. This inhibition is done by passing the mean temperature of a layer ($\overline{T}$) to the EoS instead of the local temperature so that an entire layer must heat up in order to run away, which slows the runaways. Thus there is still energy generation at the base of the convective layer to drive the convective velocities, but the small regions do not run away as rapidly. Running with this modification allows a convective velocity field to develop that is consistent with the initial model. Once the convective velocity field has stabilized, the thermodynamics and composition details are thrown out and the initial model is mapped back in, but now with a multidimensional velocity field. Then the simulation is restarted.

Chapter 9

Nuclear Reactions

Fundamentally important to the CN problem is the energy release from nuclear reactions. These reactions generate heat at the base of the envelope, creating a convective layer that is believed to cause mixing across the core-envelope boundary. This mixing in turn catalyzes the reactions, increasing the rate of heating and leading to a feedback loop that will culminate in a CN outburst. Over the course of this project, I have applied several methods to estimate the heating from nuclear reactions. Each of these tools focuses on reactions that convert hydrogen to helium.

9.1 Hydrogen Burning Chains

The important reaction processes are split into the pp chains, so named because they begin by fusing a pair of protons, and the CNO cycles, so named because they rely on looping through various isotopes of carbon, nitrogen, and oxygen. For a review of these processes, see the introduction to Wiescher et al. (2010) and references therein. Additionally, it is possible for the reactions to escape the CNO cycle and begin forming heavier elements; this is known as rp breakout, as it is based on the rapid proton process.

9.1.1 The pp Chains

The pp reaction chains begin by fusing a pair of protons, with a weak reaction converting one into a neutron, leaving behind a deuterium nucleus. A third proton is added to this, yielding ^{3}He. From this point, there are three branches. The pp I branch fuses two ^{3}He nuclei to form a ^{4}He nucleus and 2 protons, while the pp II and pp III branches merge a ^{3}He and a ^{4}He, and eventually add an additional proton to create a pair of ^{4}He nuclei. The pp chains are illustrated in Figure 9.1.

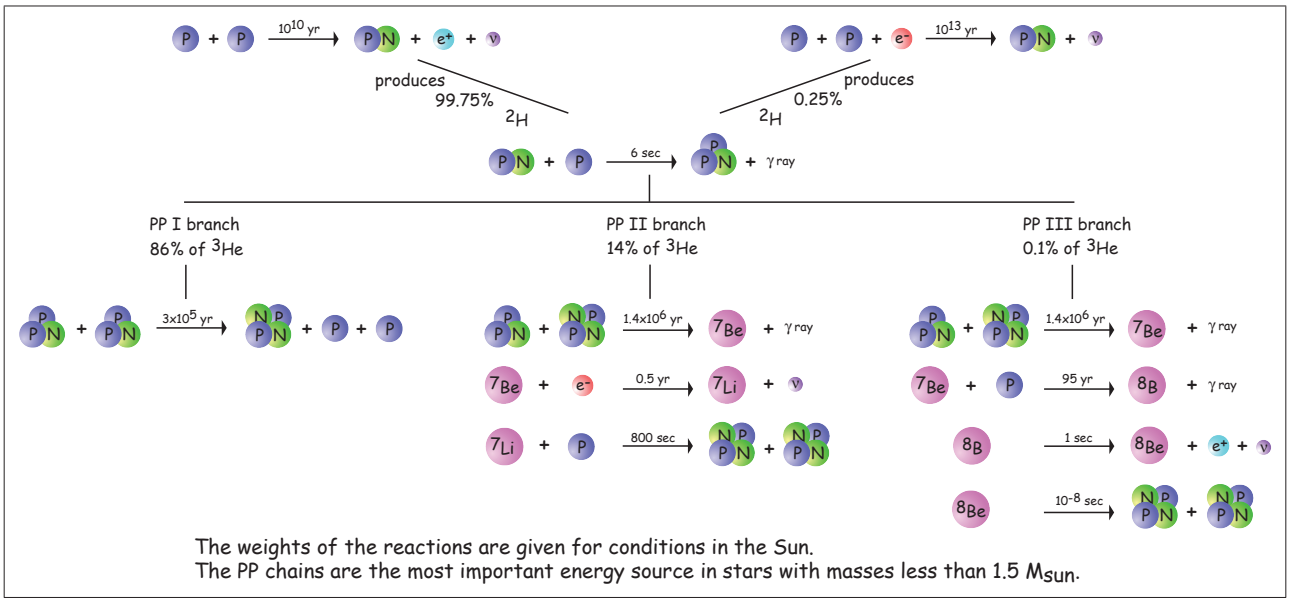

Figure 9.1: The three branches of the pp chain, which fuse protons to form nuclei of ^{4}He. This image is reprinted from `http://cococubed.asu.edu/code_pages/burn_hydrogen.shtml` by permission of Frank X. Timmes.

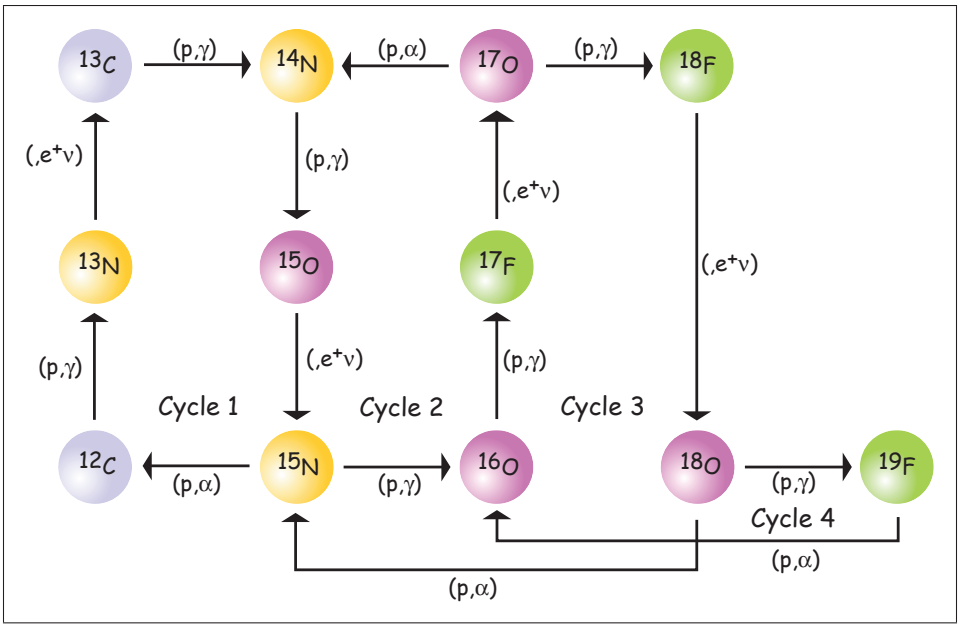

Figure 9.2: The four branches of the cold CNO cycle, which use carbon, oxygen, and nitrogen as catalysts for conversion of four protons to a ^{4}He nucleus. This image is reprinted from `http://cococubed.asu.edu/code_pages/burn_hydrogen.shtml` by permission of Frank X. Timmes.

9.1.2 The CNO Cycles

The CNO reaction cycles require the presence of carbon, nitrogen, and/or oxygen, which serve as catalysts for the conversion of hydrogen to helium by enabling new reaction pathways that are faster than those of the pp chains. There are a number of branches of the CNO cycle, but the common feature is adding four protons to a heavier nucleus (e.g., a ^{12}C nucleus), interleaved with weak reactions that convert two of the protons to neutrons. The cycle is closed by the emission of a ^{4}He nucleus, returning to the original catalyst nucleus. The four branches of the cold CNO cycle are illustrated in Figure 9.2. Figure 9.3 adds several branches of the hot CNO cycle.

9.1.3 Rapid Proton Breakout

In the rapid proton (rp) process, a seed nucleus captures protons in quick succession, building to a large, proton-rich nucleus. A high temperatures is necessary for protons to overcome the Coulomb barrier of the seed nucleus, and a high concentration of protons is necessary to capture multiple protons before weak processes begin to convert the excess protons into neutrons and return the nucleus to stability. This process escapes the CNO cycle and forms heavier elements (Wallace & Woosley, 1981). Figure 9.3 shows some channels of rp breakout from the CNO cycle.

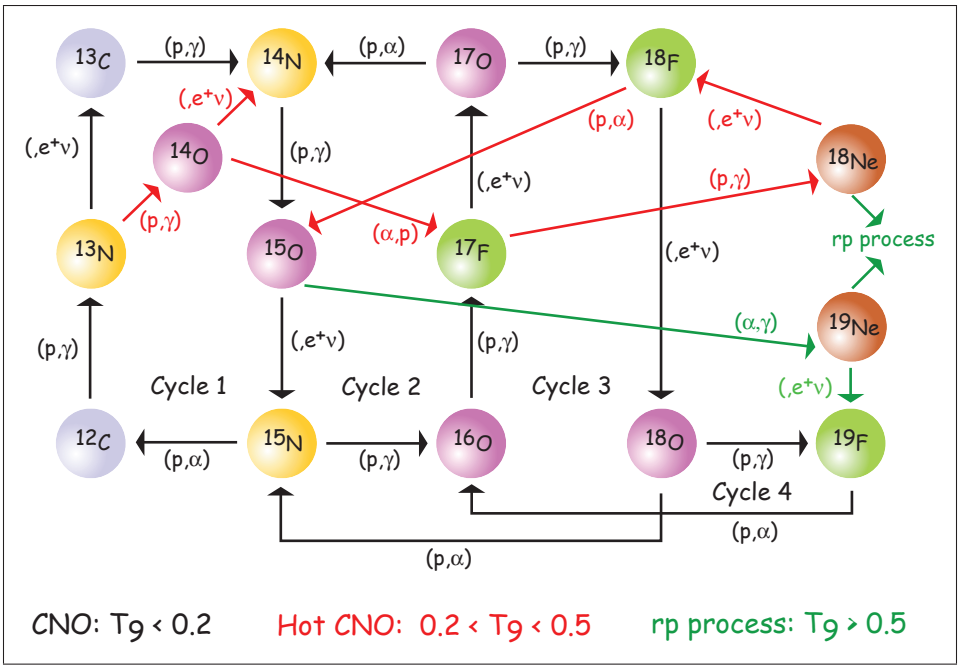

Figure 9.3: In addition to the four branches of the cold CNO cycle (shown in Figure 9.2), this figure adds branches of the hot CNO cycle, which are important at higher temperature, and rp breakout, which leaves the CNO cycle. This image is reprinted from `http://cococubed.asu.edu/code_pages/burn_hydrogen.shtml` by permission of Frank X. Timmes.

9.2 Decoupling of Reactions and Hydrodynamics

For a hydrodynamics code, fully coupling the reactions would involve adding the equations for reactions to the hydrodynamics equation set (given by Equation (6.1) for `MAESTRO`). However, reactions have a very different natural timescale from hydrodynamics; coupling these equations would require much smaller time steps than the hydrodynamics allow, which would severely limit the types of phenomena that could be simulated with such a code. In order to avoid this problem, the hydrodynamics and reactions are decoupled. Such a decoupling allows the hydrodynamics to proceed with a much longer time step than the reactions, which cycle through numerous smaller time steps to build up to a single hydrodynamics time step. In `MAESTRO`, this is done by holding the hydrodynamics constant and reacting for half of a hydrodynamics time step, then holding the reactions constant while performing a full time step for the hydrodynamics, then finally reacting for the second half of the hydrodynamics time step. Splitting the reactions into two half steps enables the method to be second-order accurate in time.

One issue that arises from this decoupling is the question of how the thermodynamic variables (especially the density and temperature) evolve during the reaction step. There exist a number of approximations for how the thermodynamic variables should evolve during reactions. All of these methods are only approximations, and do not exactly match the evolution that would result from a fully couple set of hydrodynamics and reaction equations. Decoupling is common, as the differences between a decoupled method and a coupled method

are considered to be negligible, especially for small hydrodynamics time steps. Recent research has explored ways to decouple the equations, but eliminate the resulting changes (see Section 9.5.5). I detail a few of these approximations for the evolution of the thermodynamic variables.

Isochoric: For a grid-based code, a common approximation to the thermodynamic evolution is to assume that the reaction step is an isochoric (constant density) process. This assumption is made in order to conserve mass: because the hydrodynamics are not acting during a reaction step, no matter is flowing in or out of a cell, so the mass in a cell cannot change; combining this with the constant volume of the cell gives a constant density. One caveat is that mass is not truly conserved; the nuclear reactions convert some fraction of the mass into energy, so density should actually change. However, even in an extreme case such as pure hydrogen converting to pure nickel, the change in mass is less than 1%. Therefore, this mass loss is typically neglected.

Isobaric: For `MAESTRO`, it is important to carefully monitor the pressure due to the restriction that the ratio of the pressure perturbation to the base-state pressure ($|\pi| / P_0$) be small. This suggests that `MAESTRO` should assume that reactions are an isobaric (constant pressure) process. Having an isobaric reaction network forces a choice between three different inconsistencies in the density. In the first case, the density would be evolved in a way that is thermodynamically consistent with the energy release. Doing so means that the density of a given cell changes without any flow across the boundary, breaking conservation of mass. The second case similarly evolves the density, but then neglects the density evolution from the reaction network in order to conserve mass, resulting in the hydrodynamics and the reactions having two different densities. The third choice is to hold the density constant, which brings the density out of thermodynamic consistency with the energy release.

Hydrostatic: A simple method is to assume that the thermodynamic variables do not evolve. This approximation has a variety of names, including "hydrostatic" and "pure network". This does not account for the feedback of temperature-sensitive reaction rates, effectively slowing the reactions from the speed at which they should proceed. However, this is the simplest form of the network to implement.

I make use of the isobaric and hydrostatic approximations in the reaction network described in Section 9.5. Details of my implementations of these approximations are presented below.

9.3 Analytic CNO

The first attempt at capturing the energy release from nuclear reactions, primarily existing as a preliminary testing tool, was an analytic expression to approximate the energy

release of the CNO cycle (Kippenhahn & Weigert, 1996):

$$\begin{aligned}\varepsilon = & 8.67\times10^{27}\left(1+2.7\times10^{-3}\,T_6^{1/3}-7.78\times10^{-3}\,T_6^{2/3}-1.49\times10^{-4}\,T_6\right)\\ & \times\rho\,X_{\rm CNO}\,X_{^1{\rm H}}\,T_6^{-2/3}\,\exp\left(-1.5228\times10^{2}\,T_6^{-1/3}\right),\end{aligned} \tag{9.1}$$

where T_6 is the temperature divided by $10^6\,\mathrm{K}$, and ρ and ε are assumed to be in cgs units. The symbol $X_{\rm CNO}$ represents the combined mass fraction of all carbon, oxygen, and nitrogen isotopes. This only accounts for energy release without evolving the composition, density, or temperature, and acts as a source term to Equation (6.1d). When a full network was subsequently implemented, this approximation was found to be a poor representation of CNO energy generation for the conditions in a CN.

9.4 Frank X. Timmes's `pphotcno` Network

The next step was to implement a nuclear reaction network. We chose to port Frank Timmes's `pphotcno` network[1] into `MAESTRO`. This network is designed to capture all of the nuclear processes described in Section 9.1. The core code of `pphotcno` was included essentially as it was provided by Frank Timmes (with minor modifications to integrate with the `MAESTRO` EoS), and I wrote new interface routines to connect `MAESTRO` and `pphotcno`.

The primary design decision for this process was which approximation to use. As discussed in Section 9.2, `MAESTRO` typically uses isobaric reaction networks. However, when porting `pphotcno` into `MAESTRO`, the isobaric mode presented some unexpected issues. As a temporary solution, I instead chose to run `pphotcno` in a hydrostatic mode. This was sufficient for preliminary simulations, but needed to be corrected for publishable results.

9.5 Rebuilt Network

The next implementation of nuclear reactions for my simulations involved rebuilding `pphotcno`. I did this for several reasons:

1. better integration with `MAESTRO`,
2. improved performance,
3. implementation of the isobaric assumption,
4. a code update to `MAESTRO` that implemented a technique known as spectral deferred corrections (SDC; Nonaka et al., 2012b), which works to resolve the issues that arise from decoupling the reactions from the hydrodynamics.

[1] Available at `http://cococubed.asu.edu/code_pages/burn_hydrogen.shtml`.

The original pphotcno network included subroutines to compute the reaction rates and neutrino losses. I stripped these subroutines out of the code and reused them with minimal changes (primarily for style consistency, tighter integration with MAESTRO, and elimination of redundant code such as the EoS that was already included in MAESTRO). The rest of the code was rebuilt, including the removal of the integration method built around the MA28 linear system solver and replacing it with the VODE integrator.

9.5.1 Notes on Composition

Reaction networks in MAESTRO store the following information for each species: A_k, the number of nucleons in a nucleus of species k; Z_k, the number of protons in a nucleus of species k; and B_k, the binding energy of a nucleus of species k (given as a positive value). From these, the mass of a particle of species k is given by

$$m_k = Z_k\, m_p + (A_k - Z_k)\, m_n - B_k/c^2,$$

where m_p and m_n are the masses of protons and neutrons respectively. We can also compute the mass of a mole of particles of species k:

$$W_k = N_A\, m_k,$$

where N_A is Avogadro's number. An important caution: pphotcno makes a common approximation: $W_k = A_k$. This assumes that mass is being measured in grams, and makes two further simplifying assumptions: (1) the mass of the proton and the mass of the neutron are both approximately $(1/N_A)$ g, and (2) the binding energy is negligible. These assumptions are not always appropriate, so at times it is necessary to use $N_A\, m_k$ in place of W_k. I also define $N_{\rm sp}$ to be the number of species in the reaction network.

Nuclear reaction networks often work in terms of the molar abundance (Y_k), which is the ratio of the number of moles of species k to the total mass, and therefore has units of one over mass. This is given as follows:

$$Y_k = \frac{(\text{number of moles})_k}{(\text{mass})_{\rm tot}} = \frac{(\text{molar density})_k}{(\text{mass density})_{\rm tot}} = \frac{n_k/N_A}{\rho} = \frac{1}{m_k\, N_A}\frac{\rho_k}{\rho} = \frac{X_k}{W_k},$$

where n_k is the number density of nuclei of species k. The last form will be used frequently to convert betweeen molar abundance and mass fraction, which is the form used in the hydrodynamics and the EoS.

9.5.2 Equation Outline

Reaction networks are often framed as a set of coupled ordinary differential equations of the form

$$\dot{u}_i = f_i\left(u_1, \ldots, u_{N_{\rm eq}}\right), \qquad i = 1..N_{\rm eq},$$

where $N_{\rm eq}$ is the number of equations. The first $N_{\rm sp}$ equations are the composition variables, and one or more thermodynamic quantities are also evolved. The f_i function set is often

referred to as the "right-hand side" function. The choice of how many and which thermodynamic variables are evolved depends on the assumptions and design decisions that go into the reaction network. I will demonstrate three different choices: a simple isobaric network, an isobaric network that attempts to gain an improvement in run time, and MAESTRO's SDC method.

9.5.3 A Simple Isobaric Network

The simplest method for an isobaric network is to evolve the composition and the energy, then use a call to the EoS to update the other quantities as necessary. The evolution of the thermodynamics is driven by energy release from nuclear reactions, so the energy is the most obvious choice of which thermodynamic quantity to evolve. Coupling the energy with the quantity that does not evolve (in this case pressure) uniquely defines the thermodynamic state through the EoS.

Evolution of the Composition

The fundamental job of the reaction network is to evolve the composition; networks that use the hydrostatic approximation merely evolve composition without allowing any feedback to the thermodynamics, and non-hydrostatic reaction networks evolve the thermodynamics based on energy released by the changing composition. Evolution of the composition is done by defining a set of reactions between the species present and constructing the rates of these reactions. In the pphotcno network, the reaction rates are functions of the density and temperature, and in some cases also the electron-to-baryon ratio (Y_e, derivable from the composition). Using these reaction rates, we can compute the rate of change of the composition:

$$\dot{Y}_i = \sum_j \left(\pm Y_{j,1} \; [Y_{j,2} \; [Y_{j,3}]] \; R_j(\rho, T, Y_{1..N_{\rm sp}}) \right), \tag{9.2}$$

where the summation over j includes the reactions that consume (negative sign) or form (positive sign) species i, R_j is the rate for reaction j, and $Y_{j,\ell}$ are the reactant species for reaction j. There may be 1, 2, or 3 reactants (hence why $Y_{j,2}$ and $Y_{j,3}$ are in brackets: they may or may not be present for all reactions), and they may be the same species or different species. For example, the triple-α reaction has three reactants (all of which are ^{4}He), proton capture has two reactants (^{1}H and the capturing nucleus), and electron capture only has one reactant (the nucleus that captures the electron).

Evolution of the Energy

The root of the changing thermodynamics lies in the release of energy from the nuclear reactions. The rate of change of energy is simply a summation of the nuclear energy release with an additional term for neutrino cooling. The easiest form of energy to construct is the

specific internal energy:

$$\begin{aligned}
\dot{\varepsilon} &= -\sum_k \left(\frac{\dot{E}_{\mathrm{nuc},k}}{M_{\mathrm{tot}}} \right) - \dot{\varepsilon}_\nu(\rho, T, Y_{1..N_{\mathrm{sp}}}) \\
&= -\sum_k \left(\frac{\dot{M}_k\, c^2}{M_{\mathrm{tot}}} \right) - \dot{\varepsilon}_\nu(\rho, T, Y_{1..N_{\mathrm{sp}}}) \\
&= -\sum_k \left(\frac{\dot{X}_k\, M_{\mathrm{tot}}\, c^2}{M_{\mathrm{tot}}} \right) - \dot{\varepsilon}_\nu(\rho, T, Y_{1..N_{\mathrm{sp}}}) \\
&= -\sum_k \left(\dot{Y}_k\, W_k\, c^2 \right) - \dot{\varepsilon}_\nu(\rho, T, Y_{1..N_{\mathrm{sp}}}) \\
&= -N_A\, c^2 \sum_k \left(\dot{Y}_k\, m_k \right) - \dot{\varepsilon}_\nu(\rho, T, Y_{1..N_{\mathrm{sp}}}),
\end{aligned} \tag{9.3}$$

where $\dot{E}_{\mathrm{nuc},k}$ is the nuclear energy release from species k, M_{tot} is the total mass of all species, and $\dot{\varepsilon}_\nu$ encapsulates the energy losses due to the generation of neutrinos (this term is computed by subroutines included in Frank Timmes's network). In the final step it is necessary to use $W_k = N_A m_k$: the source of the energy release is the nuclear binding energy, and the typical approximation ($W_k = A_k$) neglects this binding energy, so using $N_A m_k$ in place of W_k ensures that this expression is correct, regardless of whether or not W_k is approximated. Both terms in this expression have negative signs. The nuclear binding energy summation is actually the sum of the mass lost from nuclei, which is the opposite of the energy gained from this mass loss. The neutrino term is actually the energy lost to neutrinos, so it is subtracted out of the energy source.

9.5.4 A Faster Isobaric Network

The previous method, although simple in concept and execution, requires a call to the EoS inside of each call to the right-hand side routine. For a simple EoS, such as the ideal gas law, this may be acceptable. For a complex EoS, such as a realistic electron-ion plasma, this can result in a significant amount of time being spent in the EoS. Avoiding an EoS call could result in a faster execution time for the reaction network.

This section attempts to derive the equations for an isobaric network in such a way as to avoid a call to the EoS. However, the derivation below is incomplete, in that it neglects the evolution of thermodynamic derivatives such as c_P or $\partial h/\partial Y_k$. It may be acceptable to consider some of these as constant over the course of the integration, but which may be held constant would require testing. Preliminary testing has shown that assuming a constant value for c_P gives noticeably incorrect results over long durations, but it is necessary to evaluate this approximation on the time scale of a hydrodynamic time step, which is the duration that a reaction network would run while coupled to `MAESTRO`. In order to make use of these equations, it would be necessary to evaluate which of the thermodynamic derivatives must be evolved and then to augment the equation set to evolve the important quantities.

Coupled Evolution of Enthalpy, Temperature, and Density

Since the reaction rates are functions of the density and temperature, it makes the most sense to evolve these two quantities. For faster execution, it is best to minimize the number of variables to be evolved. Also derived in this section is the evolution equation for the specific enthalpy; as will be discussed later, this may be an important quantity and its evolution is coupled with that of the temperature and density.

The first expression comes from the relationship between specific enthalpy and specific internal energy: $h = \varepsilon + P/\rho$. Taking the time derivative of this expression and rearranging slightly gives

$$\dot{h} + \frac{P}{\rho^2}\dot{\rho} = \dot{\varepsilon}. \tag{9.4}$$

This equation couples the evolution of density and specific enthalpy together, with the evolution of the energy (given by Equation (9.3) above) as a source term.

The second expression comes from the total differential of the specific enthalpy. In `MAESTRO` the EoS supplies the partial derivatives of specific enthalpy with respect to the mass fraction, assuming that pressure and temperature are held constant. However, since the reaction rates available from Frank Timmes's network are in terms of molar abundances, we will simply convert the derivatives according to

$$\left.\frac{\partial h}{\partial Y_k}\right|_{P,T} = \left.\frac{\partial h}{\partial X_k}\right|_{P,T} W_k.$$

Now we can say that specific enthalpy should be a function of pressure, temperature, and composition and take the total differential:

$$dh = \left.\frac{\partial h}{\partial P}\right|_{T,Y_{1..N_{\rm sp}}} dP + \left.\frac{\partial h}{\partial T}\right|_{P,Y_{1..N_{\rm sp}}} dT + \sum_k \left(\left.\frac{\partial h}{\partial Y_k}\right|_{P,T} dY_k \right).$$

Since we are in the isobaric assumption, dP is zero. We can also identify the derivative with respect to temperature as the isobaric specific heat capacity. If we divide this expression by dt and rearrange slightly, we get our second equation:

$$\dot{h} - c_P \dot{T} = \sum_k \left(\frac{\partial h}{\partial Y_k} \dot{Y}_k \right). \tag{9.5}$$

This equation couples the evolution of the temperature and the specific enthalpy together, with the summation over the composition evolution expressions (given by Equation (9.2) above) as a source term.

The third expression comes from the total differential of the pressure. In `MAESTRO` the EoS supplies the partial derivatives of pressure with respect to mass fraction, assuming that density and temperature are held constant. As with the previous expression, we convert derivatives with respect to mass fraction to derivatives with respect to molar abundances by

multiplying by W_i. The total differential of pressure therefore is

$$dP = \left.\frac{\partial P}{\partial \rho}\right|_{T,Y_{1..N_{\text{sp}}}} d\rho + \left.\frac{\partial P}{\partial T}\right|_{\rho,Y_{1..N_{\text{sp}}}} dT + \sum_k \left(\left.\frac{\partial P}{\partial Y_k}\right|_{\rho,T} dY_k \right).$$

Since we are in the isobaric assumption, dP is zero. Dividing by dt and rearranging slightly gives us our third equation:

$$\frac{\partial P}{\partial \rho}\,\dot{\rho} + \frac{\partial P}{\partial T}\,\dot{T} = -\sum_k \left(\frac{\partial P}{\partial Y_k}\,\dot{Y}_k \right). \tag{9.6}$$

This equation couples the evolution of the density and the temperature together, with the summation over the composition evolution expressions (given by Equation (9.2) above) as a source term.

The final expressions are simply the result of solving these coupled equations. In order to simplify these expressions, let us define some shorthands:

$$\Lambda_h \equiv \sum_k \left(\frac{\partial h}{\partial X_k}\,W_k\,\dot{Y}_k \right), \tag{9.7a}$$

$$\Lambda_P \equiv \sum_k \left(\frac{\partial P}{\partial X_k}\,W_k\,\dot{Y}_k \right), \tag{9.7b}$$

and

$$\Delta \equiv \left(c_P\,\frac{\partial P}{\partial \rho} - \frac{P}{\rho^2}\,\frac{\partial P}{\partial T} \right)^{-1}. \tag{9.8}$$

With these we can summarize the equation set as

$$\begin{bmatrix} 1 & \frac{P}{\rho^2} & 0 \\ 1 & 0 & -c_P \\ 0 & \partial P/\partial \rho & \partial P/\partial T \end{bmatrix} \begin{bmatrix} \dot{h} \\ \dot{\rho} \\ \dot{T} \end{bmatrix} = \begin{bmatrix} \dot{\varepsilon} \\ \Lambda_h \\ -\Lambda_P \end{bmatrix}.$$

Solving this system of equations yields our final, decoupled equations:

$$\dot{h} = \Delta \left(c_P\,\frac{P}{\rho^2}\,\Lambda_P + c_P\,\frac{\partial P}{\partial \rho}\dot{\varepsilon} - \frac{P}{\rho^2}\frac{\partial P}{\partial T}\,\Lambda_h \right) \tag{9.9a}$$

$$\dot{\rho} = \Delta \left(\frac{\partial P}{\partial T}\,\Lambda_h - c_P\,\Lambda_P - \frac{\partial P}{\partial T}\,\dot{\varepsilon} \right) \tag{9.9b}$$

$$\dot{T} = \Delta \left(\frac{P}{rho^2}\,\Lambda_P + \frac{\partial P}{\partial \rho}\,\dot{\varepsilon} + \frac{\partial P}{\partial \rho}\,\Lambda_h \right) \tag{9.9c}$$

Quasi-Isochoric Approximation

In some cases it may be useful to assume that the change in density is negligible, which I refer to as the quasi-isochoric approximation. As discussed in Section 9.2, the isobaric

assumption forces a choice between different inconsistencies. Given a choice between mass non-conservation, two different densities, or thermodynamic inconsistency, it may be that thermodynamic inconsistency is the "least-bad" option.

In this case, we can simplify the expressions derived in the previous section. Firstly, Equation (9.6) can be replaced by a statement of the quasi-isochoric approximation: $\dot{\rho} = 0$. Equation (9.4) simplifies to the equivalence $\dot{h} = \dot{\varepsilon}$, eliminating the need to consider the evolution of enthalpy separately from the evolution of energy. Using this equivalence, we can simplify Equation (9.5) and solve for the temperature evolution[2]:

$$\dot{T} = \frac{1}{c_P} \left(\dot{\varepsilon} - \sum_k \left(\frac{\partial h}{\partial X_k} W_k \dot{Y}_k \right) \right). \tag{9.10}$$

Using this approximation we eliminate the need to evolve density or enthalpy and arrive at a simpler expression for the evolution of the temperature.

Energy Release

One of the important outputs from a reaction network is the energy release, although in `MAESTRO` the enthalpy release is the desired quantity. There are several possible methods for computing the final energy release.

The simplest is to call the EoS using the initial and final states of the integration. This only adds two EoS calls to the reaction network (one at the beginning of the integration and one at the end of the integration), instead of an EoS call to each iteration of the reaction network's sub-cycling (as the method outlined in Section (9.5.3) does).

The second method is to evolve the energy (or the enthalpy) directly. If the desired quantity is not already being evolved to track the thermodynamic evolution, this adds an extra variable to the reaction network, which increases the execution time of each iteration of the network's sub-cycling. Whether this is faster or slower than adding starting and ending EoS calls would have to be the subject of testing, and may depend on the duration over which the network needs to be evolved.

A third method is to use an integrated form of one of the evolution equations (Equations (9.4) – (9.6) or Equations (9.9a) – (9.9c)) to deconvolve the total change in energy or enthalpy from the total change in the density, temperature, and composition. However, this method suffers from the problem discussed above regarding the assumption that c_P and other thermodynamic derivatives are constant, and therefore it would have to be modified consistently with any other modifications implemented to address this issue.

[2]The `MAESTRO` Users' Guide (Lawrence Berkeley National Laboratory & Stony Brook University, 2012) gives an alternate derivation that achieves this same result. See Chapter 19, "Notes on Prediction Types", particularly Section 3, "Energy Evolution".

9.5.5 The SDC Method

In the SDC version of the reaction network, there is no need to approximate the thermodynamic evolution (e.g., the isobaric approximation); the SDC method is intended to evolve the reaction network consistently with the hydrodynamics by reducing the error that arises from decoupling. The SDC method is an iterative process that applies a set of corrections to reduce the decoupling error, which maintains the efficiency of a decoupled method while providing the accuracy of a fully coupled method. For complete details of the SDC method, see Nonaka et al. (2012b). I did not implement the SDC method, but only implemented a variation of the reaction network that is consistent with the requirements of the SDC method. Here I detail how the equations for the reaction network are modified to integrate with the SDC method. Borrowing from the SDC documentation in the `MAESTRO` User's Guide, the two key equations are

$$\frac{d(\rho X_k)}{dt} = \rho\,\dot{\omega}_k + A_{\rho X_k} \tag{9.11a}$$

$$\frac{d(\rho h)}{dt} = \rho\,\dot{h}_{\rm nuc} + A_{\rho h}, \tag{9.11b}$$

where $A_{\rho X_k}$ and $A_{\rho h}$ come from the hydrodynamics. They are defined as

$$A_{\rho X_k} = -\vec{\nabla}\cdot(\rho X_k \vec{u}) \tag{9.12a}$$

$$A_{\rho h} = -\vec{\nabla}\cdot(\rho h \vec{u}) + \frac{DP_0}{Dt}. \tag{9.12b}$$

While the form of these equations comes from the Euler equations, we can make a loose correspondence with product rules for derivatives to give ourselves a mental aid in understanding the relationships involved in these equations. For Equation (9.11a), the $\rho\,\dot{\omega}_k$ term is akin to $\rho\,\dot{X}_k$, and the $A_{\rho X_k}$ term is akin to $\dot{\rho}\,X_k$. For Equation (9.11b), we need to recall the relationship between enthalpy density and internal energy density ($\rho\,h = \rho\,\varepsilon + P$), and we can see that the $\rho\,\dot{h}_{\rm nuc}$ term is akin to $\rho\,\dot{\varepsilon}$, and the $A_{\rho h}$ term is akin to $\dot{\rho}\,\varepsilon + \dot{P}$. This also helps identify the fact that $\dot{h}_{\rm nuc}$ is equivalent to $\dot{\varepsilon}$. The true derivation of these equations comes from the Euler equations, so these product rules are merely a guide and not a true equivalence. It should be noted, however, that the $\dot{h}_{\rm nuc}$ term appears in both the energy and the enthalpy equations, so that it can be identified with $\dot{\varepsilon}$ formally.

The equations for $\dot{X}_k$ (except for a factor of W_k) and $\dot{\varepsilon}$ are given in Section (9.5.3). The SDC method evolves the partial densities instead of the mass fractions or molar abundances (which accounts for mass non-conservation as discussed previously when explaining the isochoric approximation for reaction networks) and the enthalpy density instead of the specific enthalpy. The density comes from a summation of the partial densities. All other thermodynamics come from a call to the EoS in ρ-h mode.

Chapter 10

Conclusions and Future Work

10.1 Preliminary Results

This project is still a work in progress. Here I present results to date, which demonstrate the current status and suggest possible conclusions that may result from this study.

Figure 10.1 shows the evolution of the peak Mach number (the largest value of $\mathcal{M}$ in the domain) over the course of a simulation of convection in the hydrogen-rich envelope of a classical nova progenitor. For the first roughly 800 s, the value of the peak Mach number varies, but on average remains approximately constant around 0.04. After the 800 s mark, the scatter around the mean trend increases in frequency, and the mean trend begins to rise. While I have not yet determined the reason(s) for these changes, this plot suggests that around 800 s the nuclear burning changes from some sort of steady-state burning to a runaway, leading towards a nova outburst.

Figure 10.2 shows a snapshot of another simulation just over 270 s after the start. The region shown is only a part of the simulation domain, focusing on the core-envelope interface (at approximately 4550 km as shown by the radial coordinate along the left side of the image) and the convective region immediately above the interface. The central panel shows a region immediately above the interface (up to approximately $4600 - 4700$ km) that is enhanced in ^{12}C, as evidenced by the greener color in this region in contrast to the more cyan color at a higher radius. By comparison with the right panel, this ^{12}C-enhanced region approximately correlates with the region of nuclear energy release. The ripples on the core-envelope interface, while not fully understood as of yet, are reminiscent of breaking waves such as those discussed in Alexakis et al. (2004), although there is concern that these ripples may be an artifact due to boundary condition effects. While more analysis, and possibly further simulations (perhaps at higher resolution), will be necessary for confirmation, these results suggest that breaking waves may play a significant role in the metallicity enrichment of the envelope.

10.2 Summary and Conclusions

While I have done extensive background work to develop the tools necessary for simulations of CNe, this is an ongoing project. My work has primarily divided into two categories.

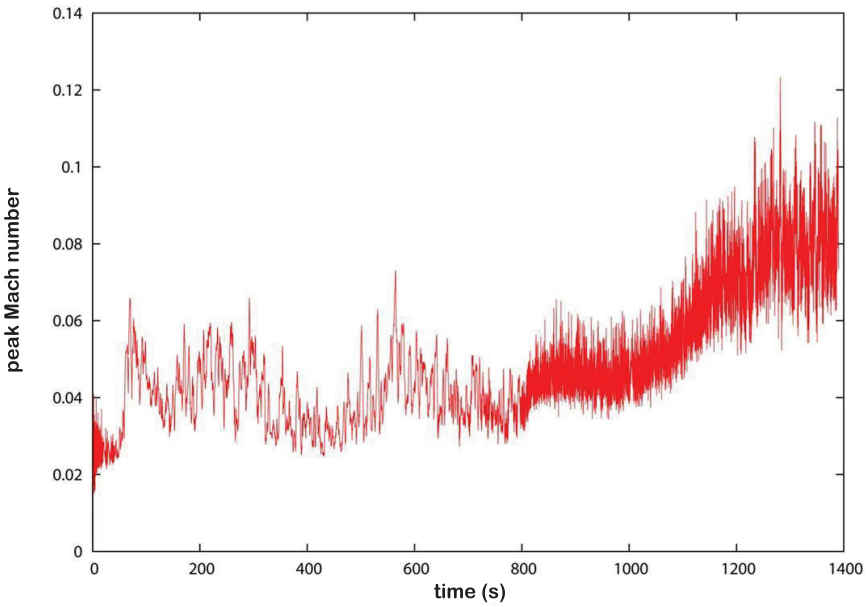

Figure 10.1: The evolution of the peak Mach number in a preliminary simulation of a classical novae in `MAESTRO`. Note the change in behavior around 800 s.

The first category is developing appropriate initial conditions for a multidimensional Eulerian code based on a one-dimensional Lagrangian code. As shown by Zingale et al. (2002), transferring between two such codes is not as trivial as copying the output of the Lagrangian code into the Eulerian code. Many issues, both physical and numerical, must be addressed in transferring a model between two such codes: e.g., the sharpness of discontinuities, hydrostatic equilibrium, the grid underlying the simulation, and convective velocities. Each much be carefully considered, not only independently, but in conjunction with the other issues; for example, interpolation to a new grid and smoothing of discontinuities may interact in unexpected ways if care is not taken to ensure hydrostatic equilibrium after each such transformation of a model.

The second category is implementing an appropriate method for capturing the nucleosynthesis and nuclear energetics of CNe. Prior research has shown that the appropriate reactions include the proton-proton chains and the carbon-nitrogen-oxygen cycles, along with rapid-proton breakout. I found that an analytic approximation to the CNO cycle is a poor representation of the energy release; in addition, it gives no information about the nucleosynthesis that occurs during a CNe. Due to time step considerations, reactions are often decoupled from hydrodynamics, which introduces errors from the approximations that are needed to close the decoupled sets of equations. However, new methods are being developed to address these errors, including spectral-deferred corrections.

The study of CNe has proven more challenging than I initially expected. This is an ongoing project, but promises to have the potential to explore new aspects of CNe and improve our understanding of these complex astrophysical phenomena.

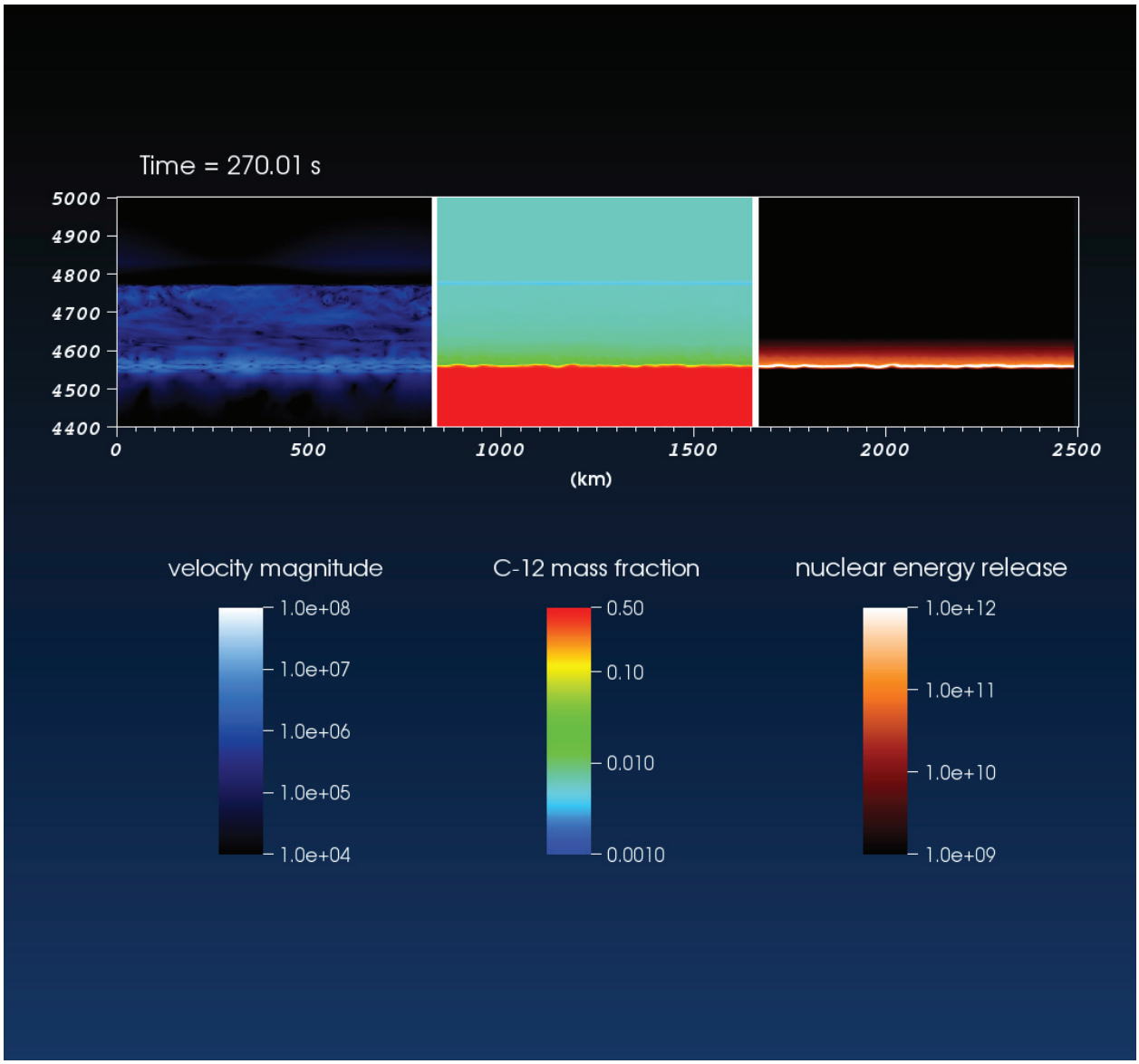

Figure 10.2: A snapshot of the core-envelope interface and convective region during a preliminary simulation of a classical nova in MAESTRO. Evidence of envelope enrichment by breaking waves is suggested by this simulation, but further analysis will be necessary to confirm such a tentative result.

10.3 Future Work

The current work on the CNe project is continued code development. This includes verification and validation (V&V) of both the initial model builder and the rebuilt nuclear reaction network. Preliminary V&V has been done, but is not yet extensive enough to ensure that these codes are ready for use in publishable work.

I am preparing a suite of two-dimensional simulations designed to test the code components and begin clarifying the computational needs of the CN problem. The most physically-realistic simulations must be performed in three dimensions in order to accurately model convection, but three-dimensional simulations are very computationally expensive. Hence a suite of two-dimensional problems will help to map out the optimal use of computational resources for three-dimensional simulations. I intend to investigate questions of:

- spatial resolution necessary to capture the processes in a CN outburst,
- boundary conditions (e.g., see Glasner et al. 2005),
- simulation domain size and its interaction with side boundary conditions,
- the possibility of a smaller reaction network that minimizes pp chain processes.

Once the code components under development have undergone rigorous V&V and the planned two-dimensional preliminary suite has been performed, I can begin to move forward with explorations of the physics of CNe. The intended goal of this project has been to study the mixing processes across the core-envelope boundary in a CN outburst. With my computational tools, I can match the published literature on the subject for comparison and validation, then begin to expand on the current understanding of these mixing processes.

Classical novae present a challenging computational problem, particularly if results are to be connected to observations. Although convection in the accreted envelope is not directly observable, the result of simulating convection-induced mixing in the burning region at the base of the accreted envelope could potentially link to observations in several ways. First, any inhomogeneities following from the structure of the turbulent convective flow could seed inhomogeneities in the ejecta (see, e.g., Casanova et al., 2011b). Next, following the evolution of a CN through the outburst would allow me to determine ejecta velocities. Simulating the outburst is a significant computational challenge because the envelope will expand through orders of magnitude in radius and a complete simulation would require interactions of the expanding envelope with the accretion disk and possibly even the binary companion.

The nuclear burning and mixing processes that occur during my simulations will also provide information about the quantity and distribution of certain nucleosynthesis products. The models and simulations presented in this dissertation assume simplified reactions for the thermonuclear burning because of the expense (in computating power and memory) of including variables for all participating nuclei. Greater fidelity and detail of the nucleosynthesis products would be achievable through post-processing of advected tracer particles based on their thermodynamic histories during a simulation. This information about nucleosynthesis could be compared to studies of the ejecta (see, e.g., Gehrz et al., 1998). The use of radiation transport would allow even more observationally-oriented information, such

as calculating light curves and spectra from the simulations. For all of these issues, the most informative results would only be achievable by the difficult process of continuing my simulations beyond the mixing phase to the outburst phase, and perhaps even beyond to following the evolution of ejecta. These different phases will require different computational tools, which may require significant development.

With the computational tools I have been developing for my CN simulations, I will be able to pursue a variety of questions in addition to mixing across the core-envelope boundary. This includes:

- Studying the complete evolution of a CN outburst, including mixing and explosion. This could allow me to develop observable signatures for comparison with my simulations. This could also potentially allow an exploration of how much mass is ejected in an outburst, which is an important question in evaluating whether or not CNe could be a phase in the evolution of a SNIa progenitor.

- Studying the effect of the mass of the underlying WD, which sets the gravity and therefore will be a significant factor in the pressure and density of the burning layer as well as the energy necessary to eject matter during an outburst. Through both of these effects, the mass of the WD may be important in determining whether or not a CNe accretes more matter between outbursts than it ejects during an outburst. This study would require the use of a stellar evolution code, such as the new open-source code `MESA`, to generate realistic initial models with different WD masses.

- Studying the effect of the composition of the accreted material, which will impact the nucleosynthesis pathways favored during an outburst, which will in turn change the rate of energy release and the total energy release before expansion quenches the burning.

- Performing a comparison of one-dimensional and multidimensional evolution. Due to the time scales involved, it is not currently possible for a multidimensional hydrodynamics code to follow the evolution of a nova from the onset of accretion through the first outburst or between outbursts. Many studies of novae must therefore rely on one-dimensional, Lagrangian, stellar evolution codes. I could perform an important check on some aspects of such codes by running an early-time model from the time-sequence provided by Ami Glasner until it matches a late-time model and comparing the evolution between a one-dimensional stellar evolution code and a multidimensional reactive hydrodynamics code.

- Studying differences in novae on carbon-oxygen WDs and oxygen-neon WDs, exploring how the resulting outbursts compare to classical vs. recurrent novae and searching for potentially-observable signatures. The common assumption in nova theory is that recurrent novae occur on oxygen-neon WDs, while classical novae occur on carbon-oxygen novae, but this has not been conclusively confirmed. This could additionally shed light on the question of whether these two different classes of novae gain or lose mass over long time scales.

- Evaluating the impact of varying uncertain reaction rates. This could shed light on potential constraints on reaction rates that are currently not well known by comparing the results of my simulations with observations.

Several of these points will require new computational tools, and some of them may not be possible with current technology. However, as long-term goals, they serve to focus my effort towards exploring the important open questions in the field of CNe.

Bibliography

Albrecht, A. et al. 2006, arXiv Astrophysics e-prints

Alexakis, A. et al. 2004, ApJ, 602, 931

Alexakis, A., Young, Y., & Rosner, R. 2002, Phys. Rev. E, 65, 059904

Almgren, A. S., Bell, J. B., Nonaka, A., & Zingale, M. 2008, ApJ, 684, 449

Almgren, A. S., Bell, J. B., Rendleman, C. A., & Zingale, M. 2006a, ApJ, 637, 922

—. 2006b, ApJ, 649, 927

Arnett, W. D. 1982, ApJ, 253, 785

Aspden, A. J., Bell, J. B., Day, M. S., Woosley, S. E., & Zingale, M. 2008, ApJ, 689, 1173

Aspden, A. J., Bell, J. B., & Woosley, S. E. 2010, ApJ, 710, 1654

Baade, W., & Zwicky, F. 1934, Physical Review, 46, 76

Bertola, F. 1964, Annales d'Astrophysique, 27, 319

Blinnikov, S. I., & Khokhlov, A. M. 1986, Soviet Astronomy Letters, 12, 131

Bloom, J. S. et al. 2012, ApJ, 744, L17

Bode, F., & Evans, A. 2008, Classical Novae, Cambridge Astrophysics Series (Cambridge University Press)

Brachwitz, F. et al. 2000, ApJ, 536, 934

Brahe, T. 1573, Copenhagen

Branch, D., Livio, M., Yungelson, L. R., Boffi, F. R., & Baron, E. 1995, PASP, 107, 1019

Brandt, T. D., Tojeiro, R., Aubourg, É., Heavens, A., Jimenez, R., & Strauss, M. A. 2010, AJ, 140, 804

Bravo, E., & García-Senz, D. 2008, A&A, 478, 843

Bravo, E., Isern, J., Canal, R., & Labay, J. 1990, Ap&SS, 169, 19

Calder, A. C. et al. 2002a, in American Institute of Physics Conference Series, Vol. 637, Classical Nova Explosions, ed. M. Hernanz & J. José, 134–138

Calder, A. C. et al. 2002b, ApJS, 143, 201

—. 2007, ApJ, 656, 313

Casanova, J., José, J., García-Berro, E., Calder, A., & Shore, S. N. 2010, A&A, 513, L5

—. 2011a, A&A, 527, A5

Casanova, J., José, J., García-Berro, E., Shore, S. N., & Calder, A. C. 2011b, Nature, 478, 490

Chaisson, E., & McMillan, S. 2001, Astronomy Today, 4th edn. (Prentice Hall)

Chamulak, D. A., Brown, E. F., Timmes, F. X., & Dupczak, K. 2008, ApJ, 677, 160

Chandrasekhar, S. 1931a, MNRAS, 91, 456

—. 1931b, ApJ, 74, 81

—. 1935, MNRAS, 95, 207

Colgate, S. A., & McKee, C. 1969, ApJ, 157, 623

Conley, A. et al. 2011, ApJS, 192, 1

Courant, R., Friedrichs, K., & Lewy, H. 1928, Mathematische Annalen, 100, 32

Crawford, J. A., & Kraft, R. P. 1956, ApJ, 123, 44

da Silva, L. A. L. 1993, Ap&SS, 202, 215

Davidson, P. A. 2004, Turbulence (Oxford: Oxford University Press)

della Valle, M., & Livio, M. 1995, ApJ, 452, 704

Domínguez, I., Höflich, P., & Straniero, O. 2001, ApJ, 557, 279

Downes, R. A., Webbink, R. F., Shara, M. M., Ritter, H., Kolb, U., & Duerbeck, H. W. 2001, PASP, 113, 764

Durisen, R. H. 1977, ApJ, 213, 145

Euler, L. 1757a, Mémoires de l'académie des sciences de Berlin, 11, 217, Euler Archive E225

—. 1757b, Mémoires de l'académie des sciences de Berlin, 11, 274, Euler Archive E226

—. 1757c, Mémoires de l'académie des sciences de Berlin, 11, 316, Euler Archive E227

—. 1761, Novi Commentarii academiae scientiarum Petropolitanae, 6, 271, Euler Archive E258

Fan Ye. 5th century, official Chinese historical text

Filippenko, A. V. 1997, ARA&A, 35, 309

Filippenko, A. V. 2009, in Stellar Death and Supernovae Conf. (Santa Barbara: UCSB), http://online.kitp.ucsb.edu/online/sdeath_c09/filippenko/

Fisher, R., Falta, D., Jordan, G., & Lamb, D. 2010, in Gravitation and Astrophysics, ed. J. Luo, Z.-B. Zhou, H.-C. Yeh, & J.-P. Hsu, 335–344

Fowler, R. H. 1926, MNRAS, 87, 114

Fryxell, B. et al. 2000, ApJS, 131, 273

Fujimoto, M., & Iben, Jr., I. 1992, ApJ, 399, 646

Fujimoto, M. Y. 1988, A&A, 198, 163

Fuller, G. M., Fowler, W. A., & Newman, M. J. 1985, ApJ, 293, 1

Gallagher, J. S., Garnavich, P. M., Caldwell, N., Kirshner, R. P., Jha, S. W., Li, W., Ganeshalingam, M., & Filippenko, A. V. 2008, ApJ, 685, 752

Gehrz, R. D., Truran, J. W., Williams, R. E., & Starrfield, S. 1998, PASP, 110, 3

Giannone, P., & Weigert, A. 1967, ZAp, 67, 41

Glasner, A. S., Livne, E., & Truran, J. W. 2011, ArXiv e-prints

Glasner, S. A., & Livne, E. 1995, ApJ, 445, L149

Glasner, S. A., Livne, E., & Truran, J. W. 1997, ApJ, 475, 754

—. 2005, ApJ, 625, 347

—. 2007, ApJ, 665, 1321

Goldhaber, G. et al. 2001, ApJ, 558, 359

Golombek, I., & Niemeyer, J. C. 2005, A&A, 438, 611

Hansen, C. J., Kawaler, S. D., & Trimble, V. 2004, Stellar interiors : physical principles, structure, and evolution, 2nd edn. (Springer-Verlag)

Hartmann, J. 1925, Astronomische Nachrichten, 226, 63

Hernanz, M., & José, J. 2002, Classical nova explosions: International Conference on Classical Nova Explosions : Sitges, Spain 20-24 May 2002, Review of progress in quantitative nondestructive evaluation (American Institute of Physics)

Hillebrandt, W., & Niemeyer, J. C. 2000, ARA&A, 38, 191

Höflich, P., & Khokhlov, A. 1996, ApJ, 457, 500

Höflich, P., Khokhlov, A. M., & Wheeler, J. C. 1995, ApJ, 444, 831

Höflich, P. et al. 2010, ApJ, 710, 444

Höflich, P., Wheeler, J. C., & Thielemann, F. K. 1998, ApJ, 495, 617

Howell, D. A. et al. 2009, ApJ, 691, 661

Hoyle, F., & Fowler, W. A. 1960, ApJ, 132, 565

Hubble, E. 1929, Proceedings of the National Academy of Science, 15, 168

Iben, Jr., I., Fujimoto, M. Y., & MacDonald, J. 1991, ApJ, 375, L27

—. 1992, ApJ, 388, 521

Iben, Jr., I., & MacDonald, J. 1985, ApJ, 296, 540

Iben, Jr., I., & Tutukov, A. V. 1984, ApJS, 54, 335

Iwamoto, K., Brachwitz, F., Nomoto, K., Kishimoto, N., Umeda, H., Hix, W. R., & Thielemann, F.-K. 1999, ApJS, 125, 439

JabRef Development Team. 2010, JabRef, JabRef Development Team

Jackson, A. P., Calder, A. C., Townsley, D. M., Chamulak, D. A., Brown, E. F., & Timmes, F. X. 2010, ApJ, 720, 99

Jacoby, G. H. et al. 1992, PASP, 104, 599

Jha, S., Riess, A. G., & Kirshner, R. P. 2007, ApJ, 659, 122

José, J., & Hernanz, M. 2007, Journal of Physics G Nuclear Physics, 34, 431

José, J., & Iliadis, C. 2011, Reports on Progress in Physics, 74, 096901

Joy, A. H. 1943, PASP, 55, 283

Kelly, P. L., Hicken, M., Burke, D. L., Mandel, K. S., & Kirshner, R. P. 2010, ApJ, 715, 743

Kercek, A., Hillebrandt, W., & Truran, J. W. 1998, A&A, 337, 379

—. 1999, A&A, 345, 831

Khokhlov, A. M. 1989, MNRAS, 239, 785

—. 1991a, A&A, 245, 114

—. 1991b, A&A, 245, L25

—. 1995, ApJ, 449, 695

—. 2000, ArXiv Astrophysics e-prints

Khokhlov, A. M., Oran, E. S., & Wheeler, J. C. 1997, ApJ, 478, 678

Kippenhahn, R., & Thomas, H.-C. 1978, A&A, 63, 265

Kippenhahn, R., & Weigert, A. 1996, Stellar Structure and Evolution (Springer)

Kirshner, R. P. 2010, in Dark Energy: Observational and Theoretical Approaches, 1st edn., ed. P. Ruiz-Lapuente (Cambridge University Press), 151

Kovetz, A., & Prialnik, D. 1985, ApJ, 291, 812

Kraft, R. P. 1964, ApJ, 139, 457

Krueger, B. K., Jackson, A. P., Calder, A. C., Townsley, D. M., Brown, E. F., & Timmes, F. X. 2012, accepted by the Astrophysical Journal

Krueger, B. K., Jackson, A. P., Townsley, D. M., Calder, A. C., Brown, E. F., & Timmes, F. X. 2010, ApJ, 719, L5

Kuhlen, M., Woosley, S. E., & Glatzmaier, G. A. 2006, ApJ, 640, 407

Kutter, G. S., & Sparks, W. M. 1987, ApJ, 321, 386

—. 1989, ApJ, 340, 985

Langanke, K., & Martínez-Pinedo, G. 2001, Atomic Data and Nuclear Data Tables, 79, 1

Lawrence Berkeley National Laboratory, C., & Stony Brook University. 2012, MAESTRO User's Guide, distributed with the MAESTRO source code

Lemaître, G. 1927, Annales de la Societe Scietifique de Bruxelles, 47, 49

Lesaffre, P., Han, Z., Tout, C. A., Podsiadlowski, P., & Martin, R. G. 2006, MNRAS, 368, 187

Li, W. et al. 2011, Nature, 480, 348

Lisewski, A. M., Hillebrandt, W., & Woosley, S. E. 2000, ApJ, 538, 831

Livio, M. 2000, in Type Ia Supernovae, Theory and Cosmology, ed. J. C. Niemeyer & J. W. Truran, 33

Livio, M., & Truran, J. W. 1987, ApJ, 318, 316

MacDonald, J. 1983, ApJ, 273, 289

Maeda, K., Röpke, F. K., Fink, M., Hillebrandt, W., Travaglio, C., & Thielemann, F.-K. 2010, ApJ, 712, 624

Malone, C. M., Nonaka, A., Almgren, A. S., Bell, J. B., & Zingale, M. 2011, ApJ, 728, 118

Mannucci, F., Della Valle, M., & Panagia, N. 2006, MNRAS, 370, 773

Mazzali, P. A., & Podsiadlowski, P. 2006, MNRAS, 369, L19

Meakin, C. A., Seitenzahl, I., Townsley, D., Jordan, G. C., Truran, J., & Lamb, D. 2009, ApJ, 693, 1188

Minkowski, R. 1941, PASP, 53, 224

Neill, J. D. et al. 2009, ApJ, 707, 1449

Newton, I. 1687, Philosophi Naturalis Principia Mathematica (Jussu Societatis Regiae ac Typis Josephi Streater. Prostat apud plures bibliopolas)

Niemeyer, J. C. 1999, ApJ, 523, L57

Niemeyer, J. C., & Hillebrandt, W. 1995, ApJ, 452, 769

Niemeyer, J. C., & Woosley, S. E. 1997, ApJ, 475, 740

Nobelprize.org. 2011, The 2011 Nobel Prize in Physics - Press Release

Nomoto, K. 1984, ApJ, 277, 791

Nomoto, K., Saio, H., Kato, M., & Hachisu, I. 2007, ApJ, 663, 1269

Nomoto, K., Sugimoto, D., & Neo, S. 1976, Ap&SS, 39, L37

Nomoto, K., Thielemann, F.-K., & Yokoi, K. 1984, ApJ, 286, 644

Nonaka, A., Almgren, A. S., Bell, J. B., Lijewski, M. J., Malone, C. M., & Zingale, M. 2010, ApJS, 188, 358

Nonaka, A., Aspden, A. J., Zingale, M., Almgren, A. S., Bell, J. B., & Woosley, S. E. 2012a, ApJ, 745, 73

Nonaka, A., Bell, J. B., Day, M. S., Gilet, C., Almgren, A. S., & Minion, M. L. 2012b, Combustion Theory and Modelling, accepted

Nugent, P. E. et al. 2011, Nature, 480, 344

Oda, T., Hino, M., Muto, K., Takahara, M., & Sato, K. 1994, Atomic Data and Nuclear Data Tables, 56, 231

Osterbrock, D. E. 2001, in Bulletin of the American Astronomical Society, Vol. 33, American Astronomical Society Meeting Abstracts, 1330

Pember, R. P., Howell, L. H., Bell, J. B., Colella, P., Crutchfield, W. Y., Fiveland, W. A., & Jessee, J. P. 1998, Combustion Science and Technology, 140, 123

Perlmutter, S. et al. 1999, ApJ, 517, 565

Phillips, M. M. 1993, ApJ, 413, L105

Phillips, M. M., Lira, P., Suntzeff, N. B., Schommer, R. A., Hamuy, M., & Maza, J. 1999, AJ, 118, 1766

Pinto, P. A., & Eastman, R. G. 2000, ApJ, 530, 744

Piro, A. L., & Bildsten, L. 2008, ApJ, 673, 1009

Piro, A. L., & Chang, P. 2008, ApJ, 678, 1158

Plewa, T., Calder, A. C., & Lamb, D. Q. 2004, ApJ, 612, L37

Poludnenko, A. Y., Gardiner, T. A., & Oran, E. S. 2011, Physical Review Letters, 107, 054501

Poludnenko, A. Y., & Oran, E. S. 2011a, Combustion and Flame, 157, 995

—. 2011b, Combustion and Flame, 158, 301

Pope, S. B. 1987, Annual Review of Fluid Mechanics, 19, 237

Porter, A. C., & Filippenko, A. V. 1987, AJ, 93, 1372

Prialnik, D., & Kovetz, A. 1984, ApJ, 281, 367

Raskin, C., Scannapieco, E., Rhoads, J., & Della Valle, M. 2009, ApJ, 707, 74

Riess, A. G. et al. 1998, AJ, 116, 1009

—. 2011, ApJ, 730, 119

Röpke, F. K. 2006, in Reviews in Modern Astronomy, Vol. 19, Reviews in Modern Astronomy, ed. S. Roeser, 127

Röpke, F. K. 2007, ApJ, 668, 1103

Röpke, F. K., Gieseler, M., Reinecke, M., Travaglio, C., & Hillebrandt, W. 2006, A&A, 453, 203

Röpke, F. K., & Hillebrandt, W. 2005, A&A, 429, L29

Röpke, F. K., & Niemeyer, J. C. 2007, A&A, 464, 683

Röpke, F. K. et al. 2011, Progress in Particle and Nuclear Physics, 66, 309

Rosner, R., Alexakis, A., Young, Y.-N., Truran, J. W., & Hillebrandt, W. 2001, ApJ, 562, L177

Scalzo, R. A. et al. 2010, ApJ, 713, 1073

Scannapieco, E., & Bildsten, L. 2005, ApJ, 629, L85

Schmidt, W., Ciaraldi-Schoolmann, F., Niemeyer, J. C., Röpke, F. K., & Hillebrandt, W. 2010, ApJ, 710, 1683

Schmidt, W., Niemeyer, J. C., & Hillebrandt, W. 2006a, A&A, 450, 265

Schmidt, W., Niemeyer, J. C., Hillebrandt, W., & Röpke, F. K. 2006b, A&A, 450, 283

Seitenzahl, I. R., Ciaraldi-Schoolmann, F., & Röpke, F. K. 2011, MNRAS, 414, 2709

Seitenzahl, I. R., Meakin, C. A., Townsley, D. M., Lamb, D. Q., & Truran, J. W. 2009a, ApJ, 696, 515

Seitenzahl, I. R., Röpke, F. K., Fink, M., & Pakmor, R. 2010, MNRAS, 407, 2297

Seitenzahl, I. R., Townsley, D. M., Peng, F., & Truran, J. W. 2009b, Atomic Data and Nuclear Data Tables, 95, 96

Sparks, W. M. 1969, ApJ, 156, 569

Sparks, W. M., & Kutter, G. S. 1987, ApJ, 321, 394

Starrfield, S. 2002, in American Institute of Physics Conference Series, Vol. 637, Classical Nova Explosions, ed. M. Hernanz & J. José, 89–98

Starrfield, S., Truran, J. W., Sparks, W. M., & Kutter, G. S. 1972, ApJ, 176, 169

Stothers, R. 1977, Isis. Journal of the History of Science Society, 68, 443

Straniero, O., Domínguez, I., Imbriani, G., & Piersanti, L. 2003, ApJ, 583, 878

Stritzinger, M., Mazzali, P. A., Sollerman, J., & Benetti, S. 2006, A&A, 460, 793

Struve, O. 1955, S&T, 14, 275

Sullivan, M. et al. 2011, ApJ, 737, 102

Timmes, F. X., Brown, E. F., & Truran, J. W. 2003, ApJ, 590, L83

Timmes, F. X., & Swesty, F. D. 2000, ApJS, 126, 501

Townsley, D. M., Calder, A. C., Asida, S. M., Seitenzahl, I. R., Peng, F., Vladimirova, N., Lamb, D. Q., & Truran, J. W. 2007, ApJ, 668, 1118

Townsley, D. M., Jackson, A. P., Calder, A. C., Chamulak, D. A., Brown, E. F., & Timmes, F. X. 2009, ApJ, 701, 1582

Travaglio, C., Hillebrandt, W., Reinecke, M., & Thielemann, F.-K. 2004, A&A, 425, 1029

Truran, J. W., Arnett, W. D., & Cameron, A. G. W. 1967, Canadian Journal of Physics, 45, 2315

Vladimirova, N., Weirs, G., & Ryzhik, L. 2006, Combust. Theory Modelling, 10, 727

Walker, M. F. 1954, PASP, 66, 230

Wallace, R. K., & Woosley, S. E. 1981, ApJS, 45, 389

Webbink, R. F. 1984, ApJ, 277, 355

Whelan, J., & Iben, Jr., I. 1973, ApJ, 186, 1007

Wiescher, M., Görres, J., Uberseder, E., Imbriani, G., & Pignatari, M. 2010, Annual Review of Nuclear and Particle Science, 60, 381

Woosley, S. E. 1986, in Saas-Fee Advanced Course 16: Nucleosynthesis and Chemical Evolution, ed. J. Audouze, C. Chiosi, & S. E. Woosley, 1

Woosley, S. E. 1990, in Supernovae, ed. A. G. Petschek, 182–212

Woosley, S. E. 2007, ApJ, 668, 1109

Woosley, S. E., Kasen, D., Blinnikov, S., & Sorokina, E. 2007, ApJ, 662, 487

Woosley, S. E., Kerstein, A. R., Sankaran, V., Aspden, A. J., & Röpke, F. K. 2009, ApJ, 704, 255

Woosley, S. E., & Weaver, T. A. 1986, ARA&A, 24, 205

Yuan, F. et al. 2010, ApJ, 715, 1338

Zingale, M. et al. 2002, ApJS, 143, 539

Zingale, M., Nonaka, A., Almgren, A. S., Bell, J. B., Malone, C. M., & Woosley, S. E. 2011, ApJ, 740, 8